This is to certify that the
thesis entitled

Validation of Computational Fluid Dynamics Simulations of Turbulent Heat Transfer Associated with the Hot Soaking Phenomenon

presented by

Takesha Sattiewhite

has been accepted towards fulfillment
of the requirements for the

M.S. degree in Mechanical Engineering

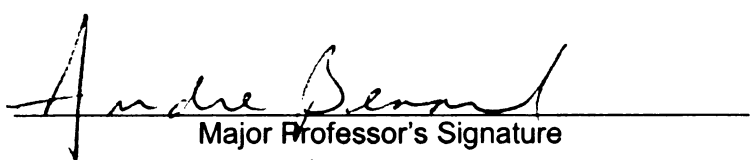

Major Professor's Signature

5/10/2007

Date

Validation of Computational Fluid Dynamics Simulations of Turbulent Heat Transfer Associated with the Hot Soaking Phenomenon

By

Takesha Sattiewhite

A THESIS

Submitted to
Michigan State University
In partial fulfillment of the requirements
For the degree of

MASTER'S OF SCIENCE

MECHANICAL ENGINEERING

2007

ABSTRACT

Validation of Computational Fluid Dynamics Simulations of Turbulent Heat Transfer Associated with the Hot Soaking Phenomenon

By

Takesha Sattiewhite

Hot soaking is a process that is used during the testing of a vehicle to study the effects of exposure to heat on vehicle components. The occurrence of a rapid increase of temperature during this process is important since it can affect the durability and performance of vehicle components.

In the present work, computational fluid dynamics (CFD) simulations were performed to study the performance of various turbulence models, needed in computations associated with convective heat transfer with the help of invariant or realizability diagrams. Three cases exhibiting phenomena associated with hot soaking were evaluated to understand the performance of turbulence models and CFD for simulating turbulent heat transfer: single phase turbulent flow through a pipe with a 90 degree bend, natural convection in a 2D square enclosure, and a two dimensional simulation of a cylinder above a heated plate. These cases aided in the development of a numerical simulation of the hot soaking process. Numerical results of the simulation illustrate the high temperature regions developed on the cylinder surface and the production of realizable turbulent heat transfer from the heated plate.

ACKNOWLEDGEMENTS

I would like to thank my advisor, Dr. Andre Benard, for his mentoring and support throughout my enrollment in the graduate program. His guidance was essential to the development of this thesis and has expanded my knowledge of turbulent heat transfer.

I would also like to thank Dr. Tom Shih for his guidance and support during my first year of the graduate program. My thanks also go to the members of my thesis committee, Dr. Charles A. Petty and Dr. Farhad Jaberi, for providing valuable insights during my thesis defense which was used to improve this thesis.

Last, but not least, I would like to thank my family and close friends for their encouragement and support throughout my graduate studies.

TABLE OF CONTENTS

LIST OF TABLES

LIST OF FIGURES

"<u>Images in this thesis are presented in color</u>".

NOMENCLATURE

a	absorption coefficient
$\vec{A}$	Area (m^2)
b_{ij}	Anisotropy tensor
C	Constant
c_p	Heat capacity at constant pressure (J/Kg-K)
C_p	Coefficient of Pressure
E	Total energy (J)
$\vec{F}$	Force vector (N)
g	Gravity (kg/m^2)
G_b	Generation of turbulence kinetic energy due to buoyancy
G_k	Generation of turbulence kinetic energy due to mean velocity gradients
G_ω	Generation of specific dissipation rate
h_f	Fluid-side local heat transfer coefficient (W/m^2-K)
$I_\lambda(\vec{r},\vec{s})$	Spectral intensity
k	Kinetic energy per unit mass (J/kg)
$\dot{m}$	Mass Flow rate (kg/s)
n	Wavelength interval
Nu	Nusselt number
P	Pressure (Pascal)
Pr	Prandtl number

q''	Total Heat Flux (W/m^2)
q''_{rad}	Radiation Heat Flux (W/m^2)
R,r	Radius (m)
S	Modulus of mean rate-of-strain tensor
T	Non-dimensional temperature in Chapter 4 (K)
T'	Fluctuating component of temperature (K)
T_f	Local fluid temperature (K)
T_i	Initial temperature (K)
T_m	Mean temperature (K)
T_w	Wall surface temperature (K)
T_∞	Fluid temperature (K)
u_j	Velocity magnitude in the j-th direction (m/s)
$\vec{u}$	Velocity magnitude in x – direction (m/s)
$\bar{u}$	Average axial velocity (m/s)
$\overline{u_i'u_j'}$	Reynolds Stress (also $u'u'$, $u'v'$, $u'w'$, etc.)
$\overline{u'T}$	Turbulent heat flux (W/m^2)
U	Centerline velocity (m/s)
$\vec{v}$	Overall velocity vector (m/s)
Y_k	Dissipation of k due to turbulence
Y_ω	Dissipation of ω due to turbulence
II, III	Second and third invariants (respectively)

Greek

β	Coefficient of thermal expansion (1/K)
δ	Delta function
δ_{ij}	Kronecker delta function
ε	Turbulent dissipation rate (m^2/s^2)
ρ	Density (kg/m^3)
σ_k	Turbulent Prandtl number for kinetic energy
σ_ε	Turbulent Prandtl number for turbulent dissipation rate
σ_s	Stefan-Boltzmann constant ($5.672 \times 10^{-8} W/m^2\text{-}K^4$)
τ	Shear Stress (Pascal)
$\bar{\bar{\tau}}_{eff}$	Effective stress tensor (Pascals)
$(\tau_{ij})_{eff}$	Deviatoric Stress Tensor
μ	Dynamic viscosity (Pascal-seconds)
μ_t	Turbulent Dynamic viscosity (Pascal-seconds)
ν	Kinematic viscosity (m^2/s)
ω	Specific dissipation rate
Γ	Effective diffusivity
Φ	Azimuthal angle
θ	Time of the averaging process

I. INTRODUCTION

I.a. Hot Soaking

Hot soaking is a phenomenon often referred to as temperature soaking or heat soaking. It is a process during which a vehicle's engine is shut-off suddenly after being ran through numerous test cycles. All sources of forced convection such as the condenser, radiator, and fans are disabled. The vehicle is parked in a chamber or near a wall, thus eliminating any source of airflow. As a result, the temperatures of the components of the vehicle located near sources of heat (exhaust system, engine, etc.) experience a rapid increase of temperature and eventually decrease to ambient conditions over a period of time. "Soaking a vehicle can also mean letting it sit (ignition off) and reach equilibrium with the environment, whether it is hot or cold. So, hot soaking in this sense would mean leaving the vehicle outside or in a hot chamber until the whole vehicle reached the ambient temperature." (Karlson 2003)

The occurrence of the rapid increase of temperature during the hot soaking process is very important, since it can diminish the durability and performance of vehicle components. The material of a component may degrade or melt, thus exposing a flammable fluid that can lead to a thermal incident. The hot soaking phenomenon is used during the testing of a vehicle in order to study the effects of heat transfer and the thermal characteristics of its components. Some applications of this phenomenon to vehicle testing include the study of the

exhaust system and nearby components of a vehicle, the study of catalytic converter cool down process, the study of brake fluid temperature rise during braking, and the study of evaporative emission testing.

One application of hot soaking is used to study the high temperatures generated on components surrounding the exhaust system of a vehicle. During vehicle testing, a temperature rise is generated on the exhaust system which affects the components near the exhaust. According to David Turner, Thermal Integration Engineer at GM, "The temperature effect of the soak is that the temperatures of components near the exhaust system tend to have a spike in the temperatures during the first few minutes of the soak. Then, the temperatures eventually decrease back to ambient" (Turner 2003). He goes on to say, "Immediately preceding the soak, the component temperatures are a result of the energy balance on the component. Usually most components are being heated from radiation from the exhaust and being cooled by conduction and convection. Immediately, after soaking starts, the radiation input is similar to the pre-soak level radiation, but convection is measurably decreased. So, a spike in the component temperature occurs. Eventually, natural convection currents become established and tend to cause air to rise up in the engine compartment and the underbody of vehicles. This air is heated as it flows over the exhaust, and the temperature of components directly over the exhaust system is bathed in this heat, adding to the temperature increase in the components". (Turner 2003)

The catalytic converter is one of the hottest components of the exhaust system. Catalytic converters are typically located near the engine exhaust manifold. Chung et al. (2003) performed a study of the use a numerical method to model the temperature soaking phenomenon that occurs during the cool down process of a 3D catalytic converter model. In this problem of temperature soaking, a temperature rise is generated on the converter skin after the engine is shut-off reaching a maximum. "The maximum temperature, which the converter assembly will see, is crucial in determining shell materials, types of mounting mats (for ceramic substrate), and mat thickness in order to avoid converter durability issues. This maximum temperature also needs to be considered in the identification of converter configurations" (Chung et al. 2003). This study by Chung et al. was used to develop a numerical simulation to predict the temperature effects of the catalytic converter.

Lee (1999) studied a typical brake system model in order to predict the maximum brake fluid temperature during the heat soaking period of a vehicle that is parked after repetitive braking. Lee states "Long repetitive braking, such as one which occurs during mountain descent, will result in a brake fluid temperature rise and may cause brake fluid vaporization. This may be concern particularly for passenger cars equipped with aluminum calipers and with a limited airflow to the wheel brake systems". If the performance is diminished then the functionality of the brake system and safety of the driver becomes an issue. The brake system components will become worn and fail, which can lead to an automobile

accident. Lee used the findings from the study of brake fluid temperature rise to develop a numerical simulation to predict the temperature effect during the heat soaking period. The numerical simulation was created to aid in the design of more efficient brake systems.

Hsu et al. (2003) studied the speciation of organic gas hot soak emissions of California light duty vehicles. Hot soaking emission test are used to estimate the chemical composition of emissions from organic gas. According to Hsu, "Hot soak emissions are comprised of fuel vapors emitted from a vehicle after the engine is turned off. The elevated engine temperature causes fuel vaporization from different sources such as fuel delivery lines, purge line to the canister, and gas cap". Hsu also states that "Speciation profiles are used in emission inventories, health risk assessments and photochemical modeling. The Benzene mass fraction (3.43% of TOG) in the current gasoline vehicular hot soak profile may over estimate benzene emissions from motor vehicles. In response to Benzene over estimation concerns, recent hot soak speciation data were requested from MSOD to update the hot soak profile." As a result of inaccurate estimations of the chemical composition of emissions, enhanced hot soaking profiles have to be developed in order to correct this inaccuracy. The accuracy of the hot soaking emissions is essential to appropriately assess emission inventory, health risk, and ozone photochemical modeling.

Hot soaking allows the study and determination of the high temperatures that are generated on the vehicle components to aid in the design of theses components

and to prevent the degradation of the components. Determining these high temperatures is important because it will allow the prediction of thermal issues concerning heat management.

The literature review on the applications of the hot soaking process to the automotive industry demonstrated the usefulness of the hot soaking process in studying temperature rises generated by sources of heat. Due to time constraints and the constant demand for fast problem resolution, many auto manufacturers use Computational Fluid Dynamics (CFD) programs that can produce a numerical prediction of performance of a component in a short amount of time. They cannot afford the time to develop an in depth study of the use of CFD to accurately predict the Hot Soaking phenomenon with transient analysis.

Most of the applications of the hot soaking process to study vehicle components mentioned previously consisted of the study of the hot soaking process to create a numerical simulation, except one: The study of the exhaust system mentioned by Turner was an application of the hot soaking process that was based on he thermal test procedure and not an numerical simulation. This study will be used in the development of a numerical simulation of the Hot Soaking process through an in depth evaluation of turbulence modeling and the heat transfer process.

I.b. Focus of Thesis

The focus of this thesis is to investigate the hot soaking phenomenon by quantifying the effect of the temperature generated on a hollow cylindrical component above a heated hollow horizontal plate. The investigation will begin with Case I consisting of a simple study of a single phase fluid flow through a pipe with a 90 degree angled bend. The simply study will be used to gain an understanding of how to effectively use CFD software to predict turbulence and heat transfer. The results will be computed using different turbulence models, evaluated at different Reynolds number values, and using the anisotropic invariant Map as a tool. The knowledge obtained from this study will then be used to conduct Case III which is the numerical simulation of the Hot Soaking process.

The Case II study will be conducted using a two-dimensional model of natural convection within a four-sided enclosure. This study will be used to gain an understanding of how to effectively use CFD software to predict natural convection with turbulence modeling and heat transfer. This study will be evaluated using the K-Epsilon turbulence models. The knowledge obtained from this study will then be used in addition to Case I to aid in the numerical simulation of the Hot Soaking process (Case III).

The Case III study will be conducted using a two-dimensional simplified model of a hollow cylindrical component above a heated hollow horizontal plate contained

within a four-sided enclosure. As stated previously, convection is measurably decreased immediately after soaking starts and thus a spike in component temperature occurs. This temperature spike is a result of conduction and radiation heat transfer. Conjugate heat transfer will be used to determine the conduction through the wall of the exhaust system as well as the radiation from the surface of the exhaust system. Since the hot soaking process does not contain forced convection, natural convection will be of interest. Earlier it was mentioned that during the duration of hot soaking the temperatures eventually decrease to ambient. Natural convection will become established thus creating currents of air that will be heated as it flows over the heated component. The hollow cylinder located above the heated plate will be soaked in the hot air thus contributing to the temperature increase of the hollow cylinder. The magnitude of the modes of heat transfer generated is needed to ascertain its contribution to the high temperatures that will develop on the hollow cylinder.

This investigation will be used to create a simple numerical simulation of the hot soaking process to aid in further study of the thermal characteristics of the exhaust system and components contained within the underhood and underbody of a vehicle. The numerical simulations will be performed using Computational Fluid Dynamics (CFD). CFD is an analytical tool that can be used to simulate thermal phenomenon of vehicle underhood and underbody components to "identify and resolve vehicle thermal issues early in the design phase. It also is an efficient tool for generating parametric studies with the potential of

significantly reducing the amount of experimentation required to optimize performance of a design". (Damodaran 2000)

I.c. Objective

The following thesis describes the study of two simple models created to understand how to use CFD to simulate turbulent flow and heat transfer, then describes the creation of a more progressive model that was used to study the hot soaking phenomenon. The body of this thesis is developed through Chapters II through V. Chapter II describes the numerical simulation of a Single Phase Fluid Flow through a Pipe with a 90 Degree Bend. Chapter III describes the numerical simulation of Natural Convection in a Two Dimensional Square Enclosure. Chapter IV describes the numerical simulation of Two Dimensional Model of a Cylinder above a Heated Plate. Chapter V summarizes the Conclusions and Recommendations of the thesis.

II. SINGLE PHASE FLOW THROUGH A PIPE WITH 90 DEGREE BEND

This chapter focuses on a three dimensional model of a single phase flow through a pipe with a 90 degree angled bend. The three-dimensional model was computed with Fluent (CFD Software) to predict turbulence and heat transfer throughout the pipe. The 3D computations were performed with the Realizable K-Epsilon and Reynolds Stress turbulence models. Computations were also done at three different values of the Reynolds number.

II.a. Problem Description

A three dimensional model of a pipe with a 90 degree angled bend was created in order to learn how CFD could be used to numerically simulate turbulence and heat transfer generated during single phase flow through a pipe. This understanding of the use of CFD will be used in addition to the knowledge gained from the next chapter to aid in the numerical simulation of the hot soaking phenomenon.

The pipe flow model is three-dimensional consisting of a pipe bent at a 90 degree angle which contains an inlet and an outlet. Figure 2-1 illustrates the geometry and triangular mesh used to create the 3D pipe of the model. Figure 2-2 illustrates a closer view of the triangular mesh used to create the 3D pipe of the model.

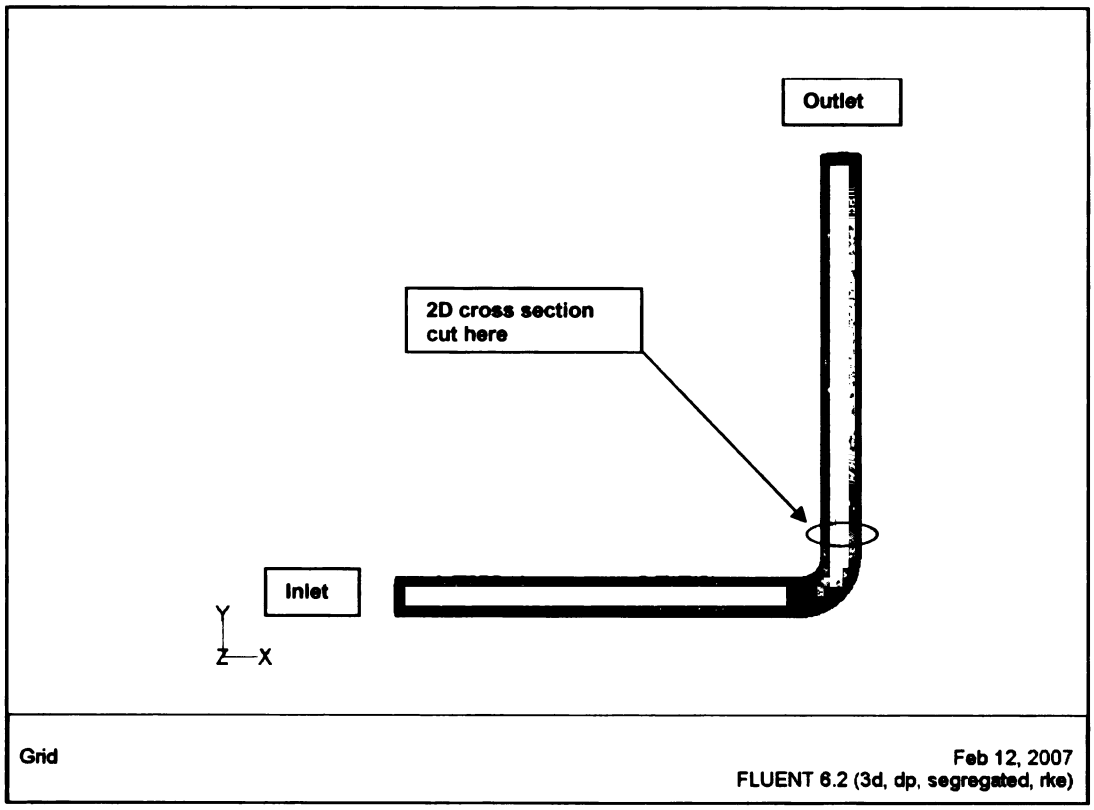

Figure 2.1: Plot of the triangular grid mesh used for the 3D Pipe Model for Single Phase Flow.

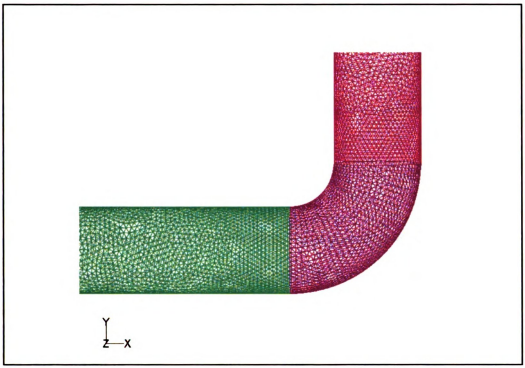

Figure 2.2: Plot of a closer view of the triangular grid mesh used for the 3D Pipe Model for Single Phase Flow.

The 3D pipe model with a 90 degree bend has a height and width of 2.0 meters. The diameter of the pipe is 0.3 meters. The fluid flowing through the pipe was modeled as air. The pipe wall was modeled with an aluminum material. The properties of the air and aluminum materials used in this model are listed in Table 2-1.

Table 2.1: List of the material properties for Air and Aluminum.

Material Properties	Air	Aluminum
Density (kg/m^3)	1.225	2719
Specific Heat (J/kg-K)	1006.43	871
Thermal Conductivity (W/m-K)	0.0242	202.4
Viscosity (kg/m-s)	1.79E-05	N/A

II.b. Problem Formulation

The initial conditions and boundary conditions used for CFD computations of the 3D pipe flow model are provided below. The model was analyzed using a steady state calculation.

Operating Conditions

The operating conditions used in this model were specified for the flow field. The temperature of the flow field was specified as 300 degrees Kelvin. The operating pressure was specified as 101,325 Pascals for the entire flow field.

Boundary Conditions

The model for this study contains surfaces also known as zones that were used for the application of boundary conditions on the surfaces of the model. Four different boundary types were used to define the boundary conditions for the different zones in the model. These boundary types are fluid, fixed temperature wall, velocity inlet, and pressure outlet.

The fluid zone was used to define the boundary condition of the fluid that is used to represent air. A fluid zone represents a group of cells that is used to calculate the governing equations of fluid flow and heat transfer. The fluid zone also participates in radiation.

Wall zones were used to define the thermal boundary conditions of the pipe wall. The pipe wall represents the source of heat in this study. A fixed temperature

wall boundary condition was applied to simulate the temperature of the hot exhaust gas inside the pipe. The temperature of the pipe wall was specified as 373.15 degrees Kelvin. The fixed temperature wall boundary condition can be referred to as the Dirichlet condition or a boundary condition of the first kind. The fixed temperature was used to calculate the heat flux generated to the wall from a fluid cell. The heat flux from a fluid cell is defined as (Fluent 2005):

$$q = h_f (T_w - T_f) + q_{rad} \tag{2.1}$$

When using the FLUENT program, the heat transfer coefficient of a fluid is computed based on the local flow-field conditions (e.g., turbulence level, temperature, and velocity profiles).

The pipe entrance was defined as a velocity inlet boundary. A velocity inlet boundary is used to define the characteristics and properties of the velocity flow at the inlet of the boundary. The flow direction of the velocity was specified normal to the boundary. A turbulence intensity of 1% and a hydraulic diameter of 0.3 meters were defined for the turbulence specification method. These inputs were then used to calculate the mass flow rate, momentum fluxes, and energy fluxes at the inlet. The equation used to calculate the mass flow rate at the entrance of the pipe is as follows (Fluent 2005):

$$\dot{m} = \int \rho \vec{v} \cdot d\vec{A} \tag{2.2}$$

As mentioned previously, the 3D model was used to compute predictions at four Reynolds numbers, therefore different velocity values were specified for each of the iterations. A velocity of 4.63 m/s was specified for the Reynolds number value of 95000, a velocity of 0.46 m/s was specified for the Reynolds number value of 9500, and a velocity of 0.049 m/s was specified for the Reynolds number value of 1000. Under normal flow conditions, the transition from laminar flow to turbulent flow occurs at Reynolds numbers of 2000 to 3000. A Reynolds number below 2000 represents a flow that is completely stable and that will always be laminar (Sabersky et al. 1999). This range of Reynolds numbers will allow the evaluation of the prediction of turbulent flow through a 3D pipe.

The pipe exit was defined as a pressure outlet boundary. A pressure outlet boundary is used to define and calculate the characteristics of the flow at the exit of the boundary. A gauge pressure was specified as 0 Pascals for the exit pressure. The gauge pressure is used as a static pressure along with other conditions which are extrapolated from the interior of the pipe to calculate the flow conditions at the exit. The backflow direction of the flow was specified normal to the exit boundary. A turbulence intensity of 1% and a hydraulic diameter of 0.3 meters were defined for the turbulence specification method.

The Realizable K-Epsilon and Reynolds Stress turbulence models were used in the evaluation of the predictions of turbulent flow for a single phase fluid using

the Fluent CFD Software. The no-slip shear boundary condition was used for wall of the pipe in this model. Since the no-slip condition has to be satisfied at the wall, the mean velocity is affected thus in turn affecting the turbulent flow. The Enhanced Wall Treatment method in Fluent was used to model the turbulent flow in the near-wall region of each pipe wall zone for the k-epsilon and Reynolds Stress Model turbulence models.

II.c. Governing Equations

The fluid flow is solved by the calculation of the following conservation of mass and momentum equations (Fluent 2005):

$$\frac{\partial \rho}{\partial t} + \nabla \cdot (\rho \vec{v}) = S_m \tag{2.3}$$

$$\frac{\partial}{\partial t}(\rho \vec{v}) + \nabla \cdot (\rho \vec{v} \vec{v}) = -\nabla p + \nabla \cdot (\bar{\bar{\tau}}) + \rho g + \vec{F} \tag{2.4}$$

Turbulence Modeling

The Realizable K-Epsilon model was selected first. The following are transport equations that FLUENT uses to calculate turbulence with the realizable k-epsilon model (Fluent 2005):

$$\frac{\partial}{\partial t}(\rho k) + \frac{\partial}{\partial x_j}(\rho k u_j) = \frac{\partial}{\partial x_j}\left[\left(\mu + \frac{\mu_t}{\sigma_k}\right)\frac{\partial k}{\partial x_j}\right] + G_k + G_b - \rho\varepsilon \tag{2.5}$$

$$\frac{\partial}{\partial t}(\rho\varepsilon)+\frac{\partial}{\partial x_j}(\rho\varepsilon u_j)=\frac{\partial}{\partial x_j}\left[\left(\mu+\frac{\mu_t}{\sigma_\varepsilon}\right)\frac{\partial\varepsilon}{\partial x_j}\right]+\rho C_1 S\varepsilon-\rho C_2\frac{\varepsilon^2}{k+\sqrt{\nu\varepsilon}}+C_{1\varepsilon}\frac{\varepsilon}{k}C_{3\varepsilon}G_b \qquad (2.6)$$

The Reynolds Stress Model was also used to evaluate the predictions of turbulent flow in this study. The following are transport equations that FLUENT uses to calculate turbulence with the Reynolds stress model (Fluent 2005):

$$\frac{\partial}{\partial t}(\rho\overline{u_i'u_j'})+\frac{\partial}{\partial x_k}(\rho u_k\overline{u_i'u_j'})=-\frac{\partial}{\partial x_k}\left[\overline{\rho u_i'u_j'u_k'}+\overline{p(\delta_{kj}u_i'+\delta_{ik}u_j')}\right]$$

$$+\frac{\partial}{\partial x_k}\left[\mu\frac{\partial}{\partial x_k}(\overline{u_i'u_j'})\right]-\rho\left(\overline{u_i'u_k'}\frac{\partial u_j}{\partial x_k}+\overline{u_j'u_k'}\frac{\partial u_i}{\partial x_k}\right)-\rho\beta(g_i\overline{u_j'\theta}+g_j\overline{u_i'\theta}) \qquad (2.7)$$

Heat Transfer

The energy equation was used for the calculation of heat transfer. All modes of heat transfer were calculated for this study. The modes of heat transfer are conduction, convection, and radiation. The following form of the energy equation was specified for the calculation of conduction and convection heat transfer (Fluent 2005):

$$\frac{\partial}{\partial t}(\rho E)+\frac{\partial}{\partial x_i}(u_i(\rho E+p))=\frac{\partial}{\partial x_j}\left(k_{eff}\frac{\partial T}{\partial x_j}+u_i(\tau_{ij})_{eff}\right) \qquad (2.8)$$

Velocity Profile Computation

The following analytical formula was calculated to determine the velocity profile for turbulent flow through a smooth pipe:

$$\frac{\bar{u}}{U} = \left(1 - \frac{r}{R}\right)^{1/n}, \text{ (Fox and McDonald, 1998)} \qquad (2.9)$$

where

$$n = -1.7 + 1.8 \log Re_v \qquad (2.10)$$

II.d. Anisotropic Invariant Map

In order to properly evaluate the numerical predictions of turbulence, a method must be used to validate these predictions. One such method has been developed by Lumley (1978, 2001). This method states that the state of turbulent flow can be analyzed and distinguished by its anisotropy. The anisotropy of the turbulent flow can be determined from the Reynolds stresses

$$\tau_{ij} = -\rho \overline{u'v'} \qquad (2.11)$$

$\overline{u'u'}$ - X component Reynolds stress
$\overline{v'v'}$ - Y component Reynolds stress
$\overline{w'w'}$ - Z component Reynolds stress
$\overline{u'v'}$ - X and Y component Reynolds stress

The anisotropy is determined by subtracting the isotropic part of the Reynolds stress from itself and normalizing by $\overline{u'u'}$. This mathematical manipulation forms the Reynolds anisotropy tensor (Lumley 1978):

$$b_{ij} = \frac{\overline{u_i u_j}}{\overline{u_i u_i}} - \frac{\delta_{ij}}{3} \tag{2.12}$$

$$\overline{u_i u_i} = 2k \tag{2.13}$$

Where k represents the turbulent kinetic energy and δ_{ij} represents the Kronecker delta function. The second (II) and third (III) invariants of the tensor b_{ij} can be calculated and

$$-II = b_{33}^2 - b_{11}b_{22} + b_{12}^2 \tag{2.14}$$

$$III = b_{33}(b_{11}b_{22} - b_{12}^2) \tag{2.15}$$

then plotted to create what is known as the Anisotropic Invariant Map (Lumley 1978). Figure 2.3 illustrates an Anisotropic Invariant Map created by Krogstag and Simonsen (2005).

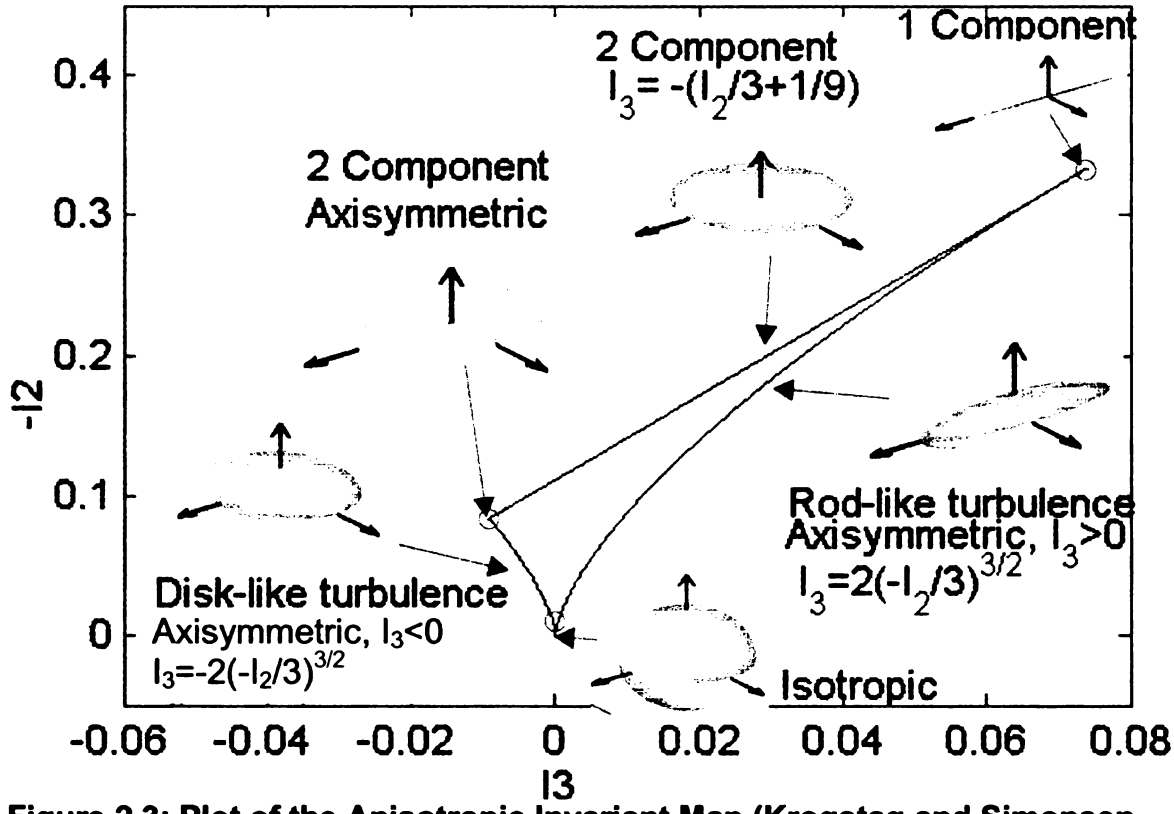

Figure 2.3: Plot of the Anisotropic Invariant Map (Krogstag and Simonsen 2005).

The Anisotropic Invariant Map is used to characterize the turbulent flow in terms on the Reynolds anisotropy tensor. If the anisotropy calculated is plotted and lies within the triangle domain of the anisotropic invariant map the turbulent flow is considered physically realizable. If the plotted anisotropy lies outside of the triangle then the turbulence is considered to be invalid. In the graph above "–I2" and "I3" represent the second (II) and third (III) invariants of the tensor b_{ij} defined previously.

In this study, the Reynolds stress tensors will be determined for the Realizable K-Epsilon and Reynolds Stress turbulence models. In the Fluent CFD program,

once the Reynolds Stress turbulence model is specified, the Reynolds stresses are obtain feasibly through post processing. The values can be either plotted or reported numerically. However, the Reynolds stresses have to be derived for the Realizable K-Epsilon turbulence model.

In order to derive the Reynolds stress from the Realizable K-Epsilon turbulence model, the Boussinesq hypothesis has to be used (Fluent 2005).

$$-\overline{\rho u_i' u_j'} = \mu_t \left(\frac{\partial u_i}{\partial x_j} + \frac{\partial u_j}{\partial x_i} \right) - \frac{2}{3} \left(\rho k + \mu_t \frac{\partial u_i}{\partial x_i} \right) \delta_{ij} \tag{2.16}$$

$$\overline{u'u'} = -\frac{\mu_t}{\rho} \left(2 \frac{\partial u}{\partial x} \right) + \frac{2}{3} \left(k + \frac{\mu_t}{\rho} \frac{\partial u}{\partial x} \right) \tag{2.17}$$

$$\overline{v'v'} = -\frac{\mu_t}{\rho} \left(2 \frac{\partial v}{\partial y} \right) + \frac{2}{3} \left(k + \frac{\mu_t}{\rho} \frac{\partial v}{\partial y} \right) \tag{2.18}$$

$$\overline{w'w'} = -\frac{\mu_t}{\rho} \left(2 \frac{\partial w}{\partial z} \right) + \frac{2}{3} \left(k + \frac{\mu_t}{\rho} \frac{\partial w}{\partial z} \right) \tag{2.19}$$

$$\overline{u'v'} = -\frac{\mu_t}{\rho} \left(\frac{\partial u}{\partial y} + \frac{\partial v}{\partial x} \right) \tag{2.20}$$

The Reynolds stresses obtained from the two turbulence models can be used to calculate the anisotropic components of the Reynolds stress tensor. The values of the anisotropy generated from the Realizable K-Epsilon and Reynolds Stress turbulence models will be plotted on an anisotropic invariant map to determine the validity of the turbulence model predictions. The results and plots of the evaluation of the turbulent flow can be found in the numerical results section

below.

II.e. Numerical Method of Solution

Computational Fluid Dynamics (CFD) was used to simulate the hot soaking process with a computer by computing the solutions to differential equations. The differential equations computed are the governing equations of fluid flow and heat transfer. CFD works best when used in conjunction with grid generation and post-processing analysis. Typically, the CFD process is executed as follows:

I) Pre-processors are used to create 2D and 3D geometric models and meshes

II) Pre-processors are then used to generate volume meshes from the geometric models

III) Solvers are used to numerically simulate fluid flow and heat transfer by computing solutions to the differential equations

IV) Post-processing analysis is used to evaluate the numerical solutions computed

HyperMesh, TGrid, and FLUENT CFD programs were used in this study to numerically simulate the single phase flow through the pipe containing a 90 degree angled bend as mentioned above. To begin, a 3D model of a 90 degree angled was constructed with triangular elements using HyperMesh. The 3D model was then imported into the TGrid program to generate the volume

elements. The volume elements were created from the triangular elements forming a tetrahedral mesh. The volume in this model was used to simulate the air flowing through the pipe. After the volume was generated, the model was imported into the FLUENT CFD program to numerically simulate the single phase flow.

Since the focus of this study is to predict the turbulence and heat transfer generated by single phase flow through a pipe, two cases created. The first case was used to examine turbulence modeling. The second case was used to simulate different values of the Reynolds number by creating a range of models.

II.f. Numerical Results

As mentioned previously, two different cases were examined to evaluate the use of the CFD software to predict the turbulence and heat transfer of the single phase fluid flow through a pipe with a 90 degree angled bend. These two cases were used to study the single phase flow through turbulence modeling and the use of different values of Reynolds numbers. To examine turbulence modeling, the Realizable K-Epsilon and Reynolds Stress turbulence models were specified so that the turbulent flow could be generated and analyzed. Finally, the 3D model was modified by creating three different models calculated with different velocities to simulate different values of the Reynolds number.

A 2D cross section was cut from the pipe as shown in Figure 2.1 and 2.4. The cross section was used as a plane to display the plot of the vorticity vectors and the static temperature contour plots. Figures 2.5 through 2.10 illustrate the vector plot of the vorticity magnitude generated in a cross section of the pipe for the two different turbulence models and the Reynolds numbers values of 1000, 9500, and 95000. This figure shows that the vorticity magnitude increase as the Reynolds number increases. This trend is expected because as the Reynolds number increases, the velocity increases (See Table 2.2). It also displays a symmetrical vortex circulation pattern as a result of using the realizable K-Epsilon turbulence model. The vortex patterns generated for the Reynolds Stress turbulence models are symmetric except for at the Reynolds number value of 9500. At the Reynolds number value of 9500, the use of the Reynolds Stress turbulence model produces a large vortex circulation zone near the bottom wall of the pipe cross-section.

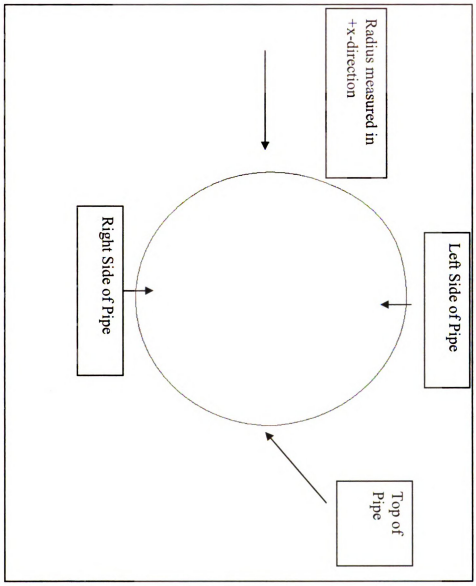

Figure 2.4: Plot of the 2D cross section cut from the pipe.

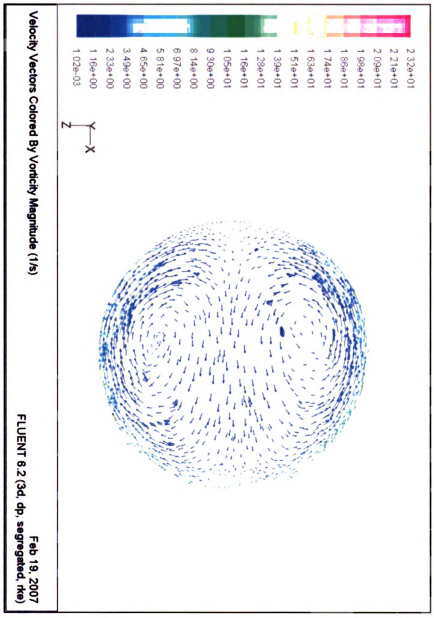

Figure 2.5: Plot of the vector plot of the vorticity magnitude generated in a cross section of the pipe for the K-Epsilon Turbulence Model with Re No. = 1000.

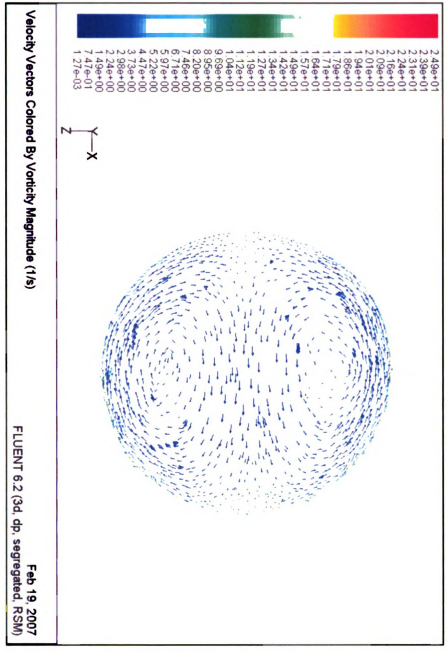

Figure 2.6: Plot of the vector plot of the vorticity magnitude generated in a cross section of the pipe for the RSM Turbulence Model with Re No. = 1000.

Figure 2.7: Plot of the vector plot of the vorticity magnitude generated in a cross section of the pipe for the K-Epsilon Turbulence Model with Re No. = 9500.

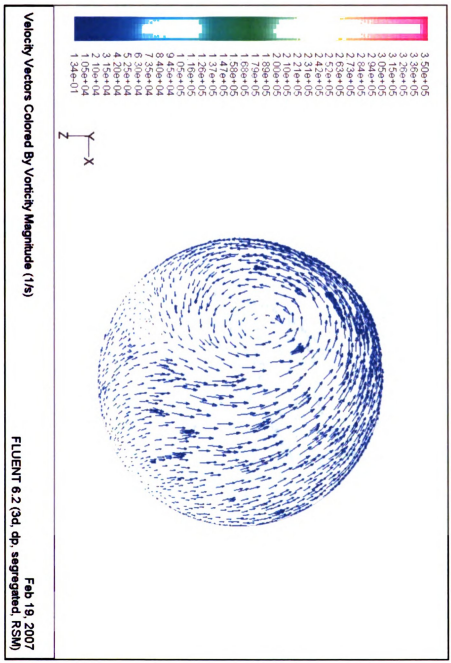

Figure 2.8: Plot of the vector plot of the vorticity magnitude generated in a cross section of the pipe for the RSM Turbulence Model with Re No. = 9500.

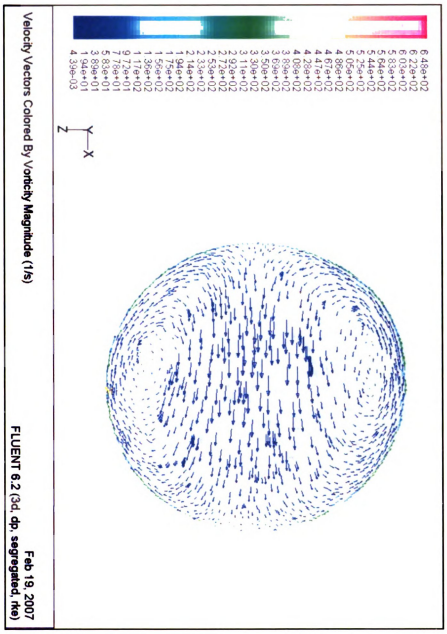

Figure 2.9: Plot of the vector plot of the vorticity magnitude generated in a cross section of the pipe for the K-Epsilon Turbulence Model with Re No. = 95000.

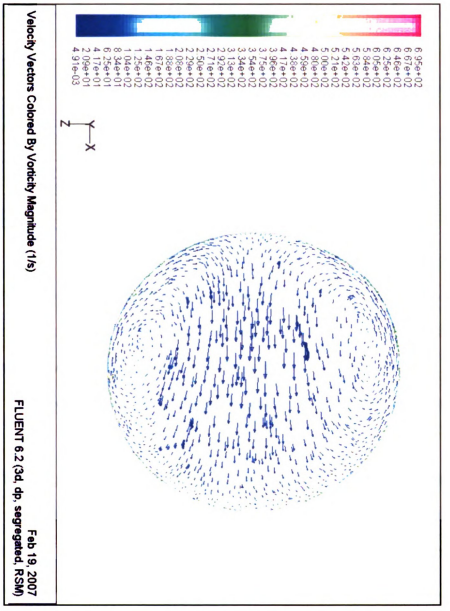

Figure 2.10: Plot of the vector plot of the vorticity magnitude generated in a cross section of the pipe for the RSM Turbulence Model with Re No. = 95000.

Table 2.2: List of the vorticity magnitude generated in a cross section of the pipe for the different turbulence models and Reynolds number values.

Turbulence Model	Reynolds Number	Velocity (m/s)	Vorticity Magnitude (od 2D cross-section)
Realizable K-Epsilon	1000	0.049	18.16
Realizable K-Epsilon	9500	0.46	97.8
Realizable K-Epsilon	95000	4.63	469.4
Reynolds Stress Model	1000	0.049	20.44
Reynolds Stress Model	9500	0.46	167.83
Reynolds Stress Model	95000	4.63	473

Table 2.2 lists the vorticity magnitude generated in cross sections of the pipe for the different turbulence models and Reynolds number values. This table also illustrates that the vorticity magnitude increases as the Reynolds number increases. The Reynolds stress model generates a higher vorticity magnitude.

Figures 2.11 through 2.16 illustrate the static temperature contours generated in a cross section of the pipe for the following Reynolds numbers values of 1000, 9500, and 95000. These figures show that the temperature distribution changes as the Reynolds number increases. At the lower Reynolds number value, the higher temperature value is dominant. The higher temperature value tends to be distributed more towards the bottom wall of the pipe. As the Reynolds number increases, the higher temperature value becomes more evenly distributed around the walls of the pipe. This trend is expected because as the Reynolds number increases, the velocity increases thus creating more airflow. The increased

airflow decreases the hot spot that is generated and creates a more even distribution of the temperature.

Also, it is shown that the Reynolds Stress Model produces a higher temperature distribution than the K-Epsilon model. As mentioned previously, the Reynolds Stress model produces a higher vorticity magnitude. The rotation and swirling motion of the hot air in the pipe can increase the thermal energy thus increasing the temperature of the air. It can be concluded that the higher vorticity magnitude creates higher temperature zones.

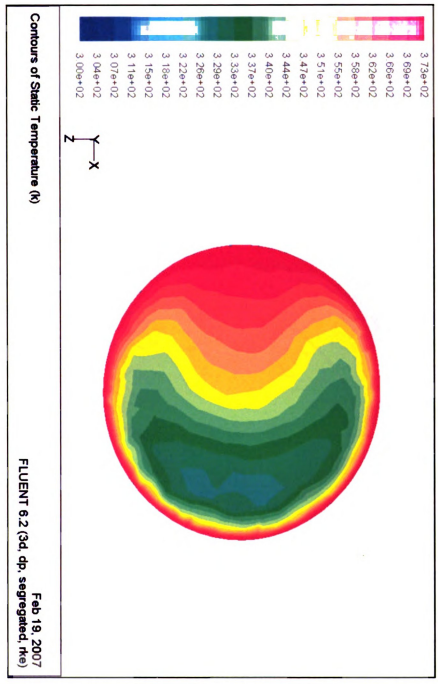

Figure 2.11: Plot of the static temperature contours generated in a cross section of the pipe for the K-Epsilon Turbulence Model with Re No. = 1000.

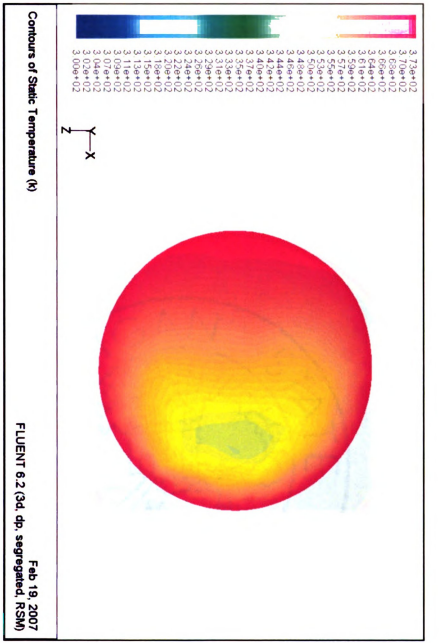

Figure 2.12: Plot of the static temperature contours generated in a cross section of the pipe for the RSM Turbulence Model with Re No. = 1000.

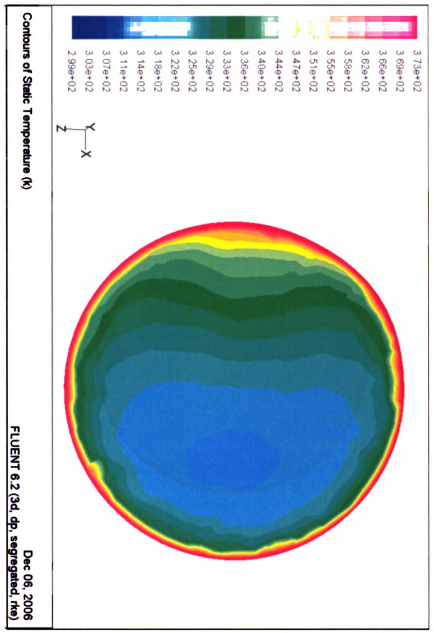

Figure 2.13: Plot of the static temperature contours generated in a cross section of the pipe for the following models: K-Epsilon Turbulence Model with Re No. = 9500.

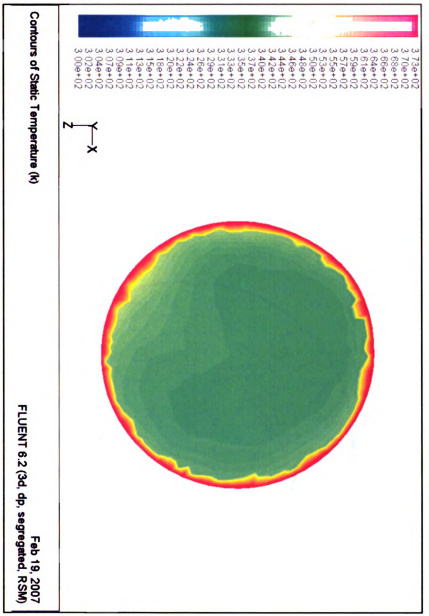

Figure 2.14: Plot of the static temperature contours generated in a cross section of the pipe for the following models: RSM Turbulence Model with Re No. = 9500.

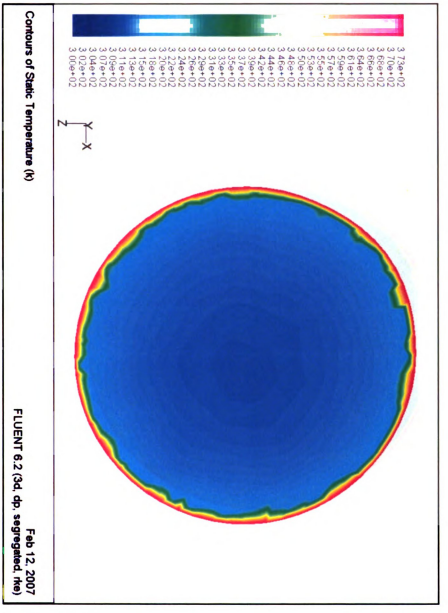

Figure 2.15: Plot of the static temperature contours generated in a cross section of the pipe for the following models: K-Epsilon Turbulence Model with Re No. = 95,000.

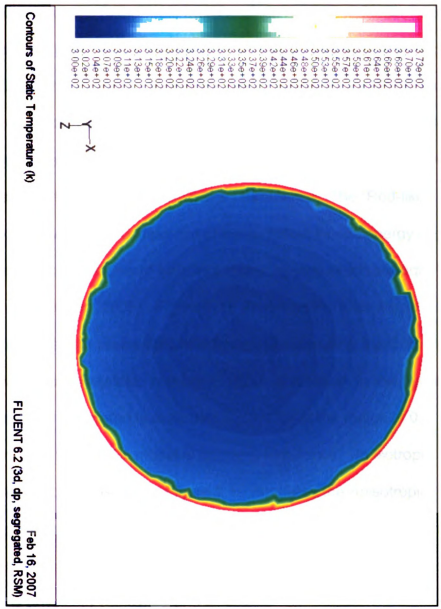

Figure 2.16: Plot of the static temperature contours generated in a cross section of the pipe for the following models: RSM Turbulence Model with Re No. = 95,000.

Figure 2.17 illustrates the Anisotropic Invariant Map generated for single phase fluid flow through a pipe using the K-Epsilon Turbulence Model at a Reynolds number of 1000. The anisotropy was calculated from the Reynolds stress values of the 2D cross-section cut from the pipe. The turbulence flow in this model is physically realizable. The turbulence generated is isotropic and slightly tends toward axis-symmetric expansion ("Rod-like") turbulence. The "Rod-like" turbulence occurs when one component of the turbulent kinetic energy is greater than the other two components of turbulent kinetic energy which are equal (Krogstag and Simonsen, 2005). Figure 2.18 illustrates the Anisotropic Invariant Map generated for single phase fluid flow through a pipe using the K-Epsilon Turbulence Model at a Reynolds number of 9500. It is shown in this figure that all of the anisotropy generated is realizable except for at the radius of 0.6. The realizable turbulent flow in this model is isotropic turbulence. In isotropic turbulence the anisotropy is zero. Figure 2.19 illustrates the Anisotropic Invariant Map generated for single phase fluid flow through a pipe using the K-Epsilon Turbulence Model at a Reynolds number of 95,000. The turbulence flow in this model is physically realizable and isotropic.

Figure 2.20 illustrates the Anisotropic Invariant Map generated for single phase fluid flow through a pipe using the Reynolds Stress Turbulence Model at a Reynolds number of 1000. The turbulent flow in this model is physically realizable except for at the center of the pipe (r = 0). However, the realizable turbulence ranges from axis-symmetric expansion to two-component turbulence.

Two-component turbulence can be found in the viscous sub layers at the wall. At this location the wall-normal component of velocity fluctuations tends to zero, leaving only wall-parallel components (Jovicic, 2006). Figure 2.21 illustrates the Anisotropic Invariant Map generated for single phase fluid flow through a pipe using the Reynolds Stress Turbulence Model at Reynolds number of 9500. The turbulent flow in this model is physically realizable and ranges from isotropic turbulence to axis-symmetric expansion. Figure 2.22 illustrates the Anisotropic Invariant Map generated for single phase fluid flow through a pipe using the Reynolds Stress Turbulence Model at Reynolds number of 95,000. The turbulent flow in this model is physically realizable except for at the center of the pipe and at the radius equal to 0.86. However, the realizable turbulence produced in this model tends toward axis-symmetric expansion.

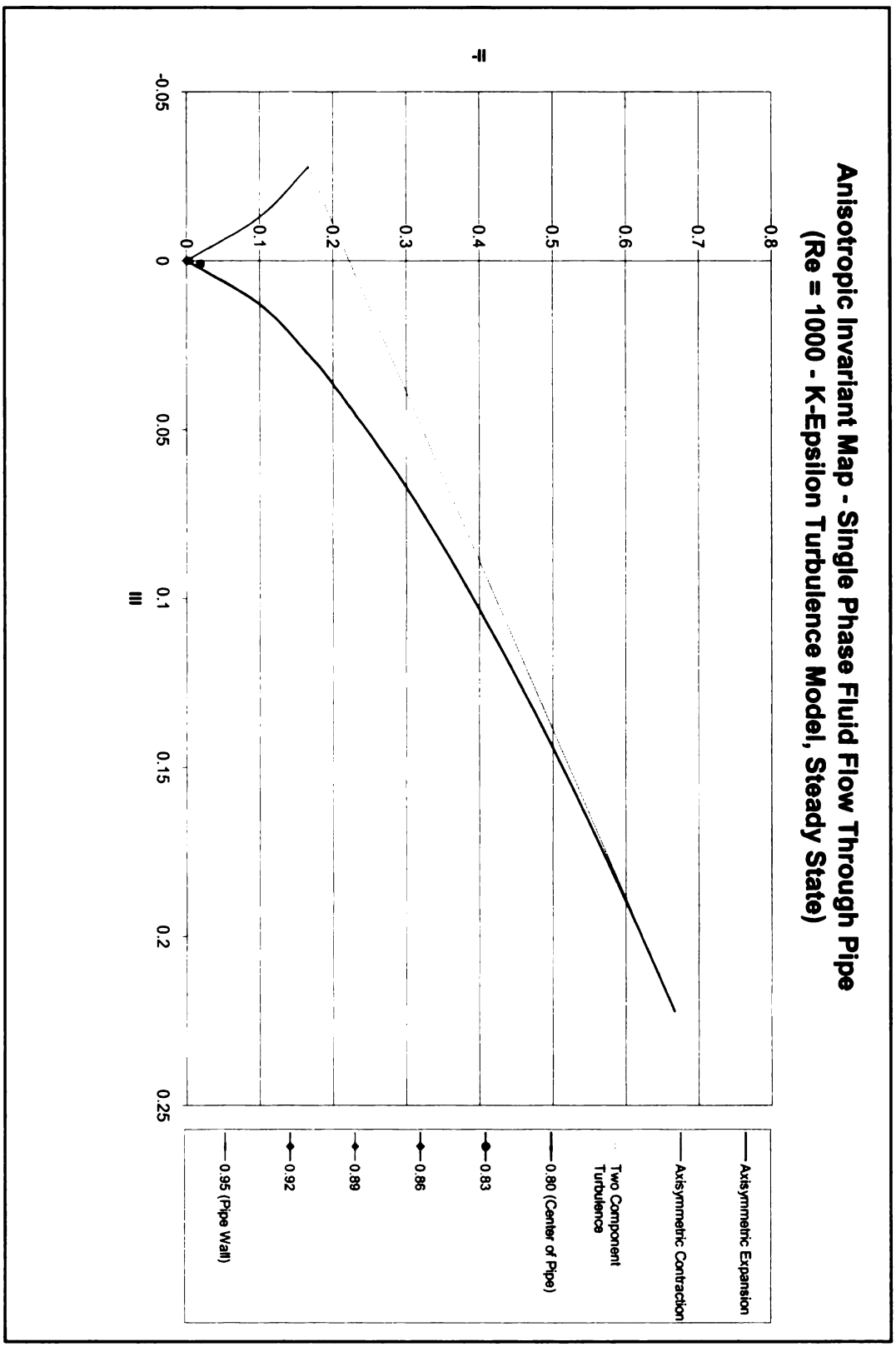

Figure 2.17: Plot of the Anisotropic Invariant Map generated for single phase fluid flow through a pipe using the K-Epsilon Turbulence Model at Re No. = 1000.

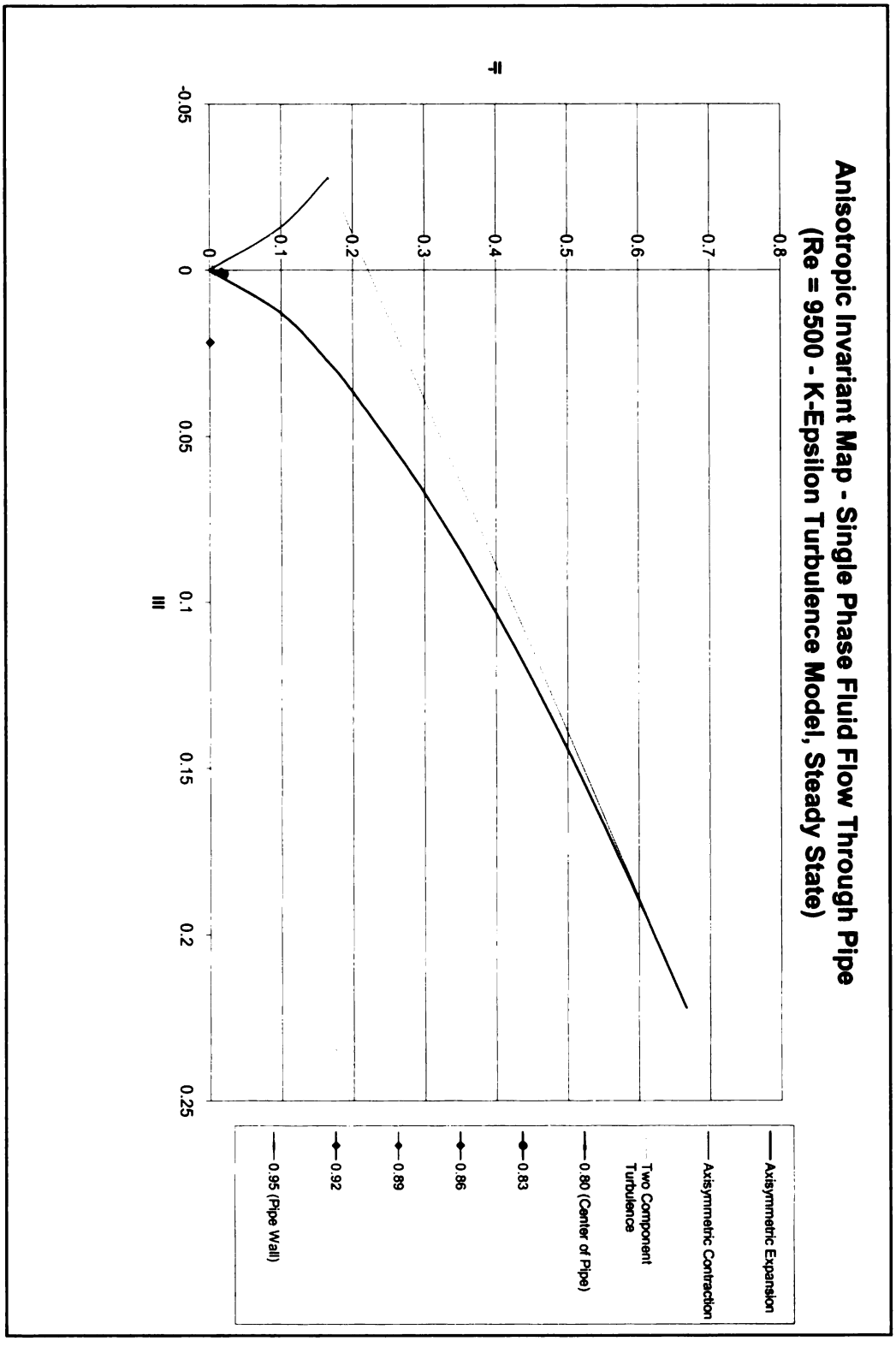

Figure 2.18: Plot of the Anisotropic Invariant Map generated for single phase fluid flow through a pipe using the K-Epsilon Turbulence Model at Re No. = 9500.

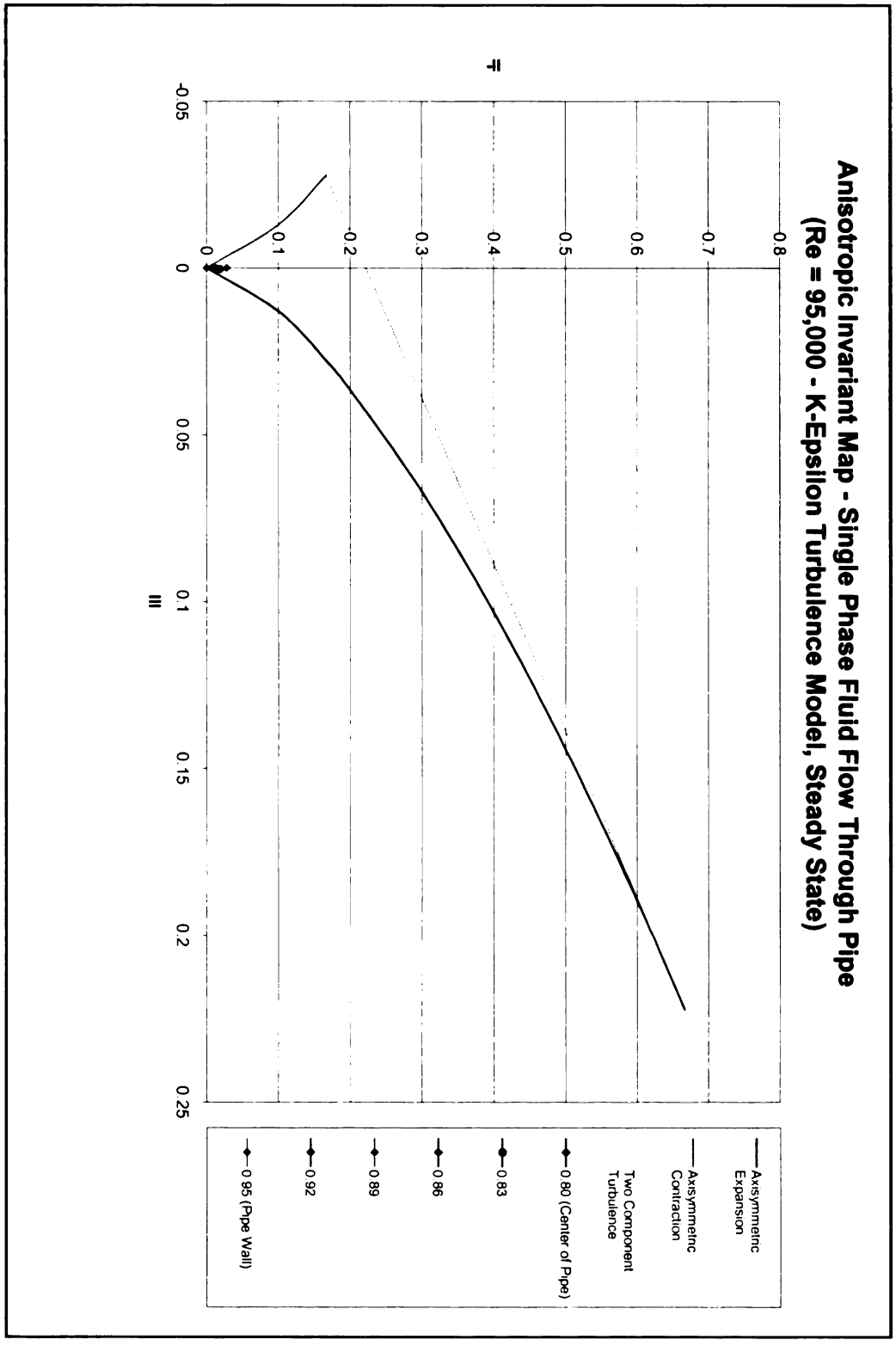

Figure 2.19: Plot of the Anisotropic Invariant Map generated for single phase fluid flow through a pipe using the K-Epsilon Turbulence Model at Re No. = 95,000.

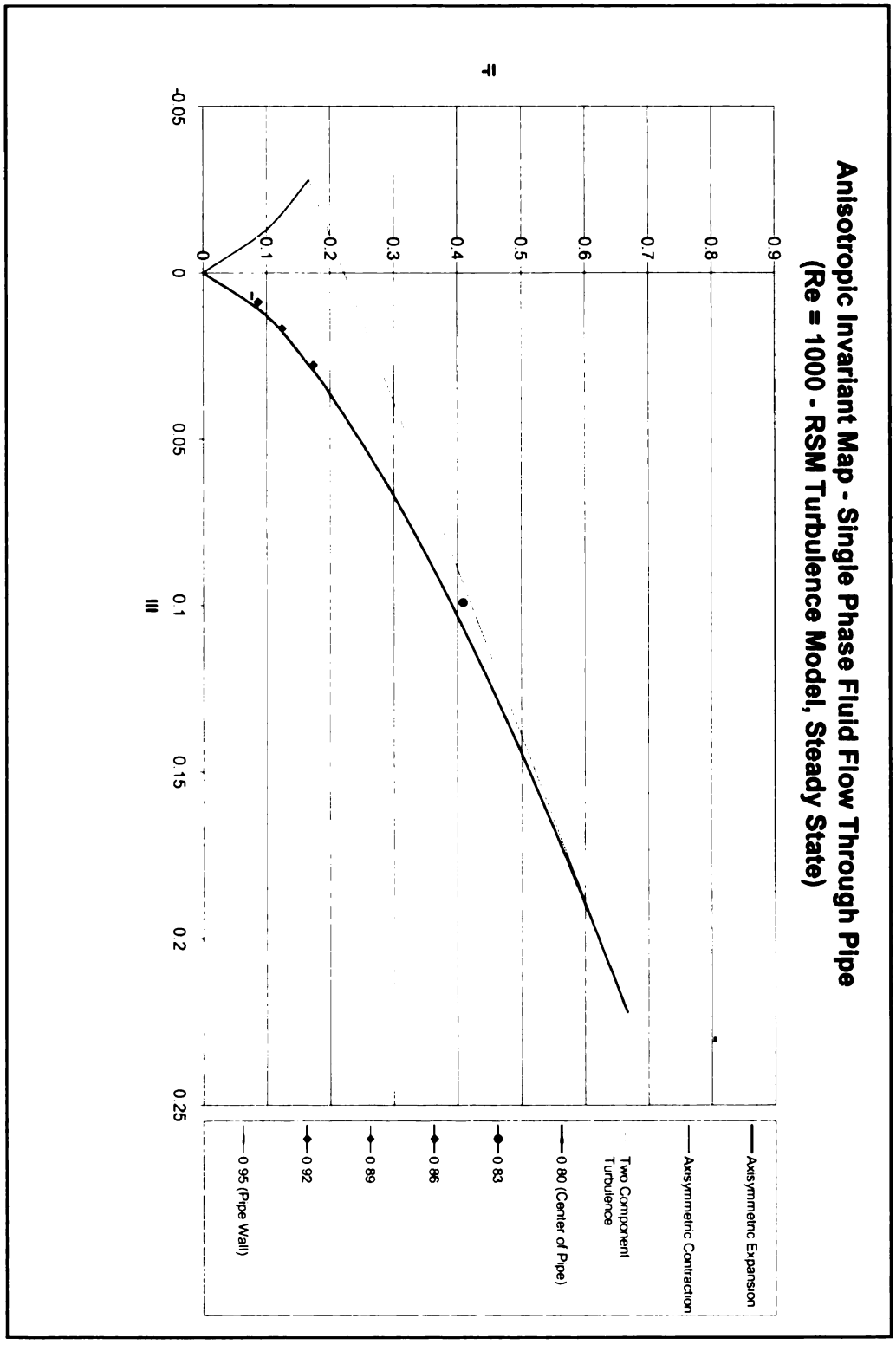

Figure 2.20: Plot of the Anisotropic Invariant Map generated for single phase fluid flow through a pipe using the Reynolds Stress Turbulence Model at Re No. = 1000.

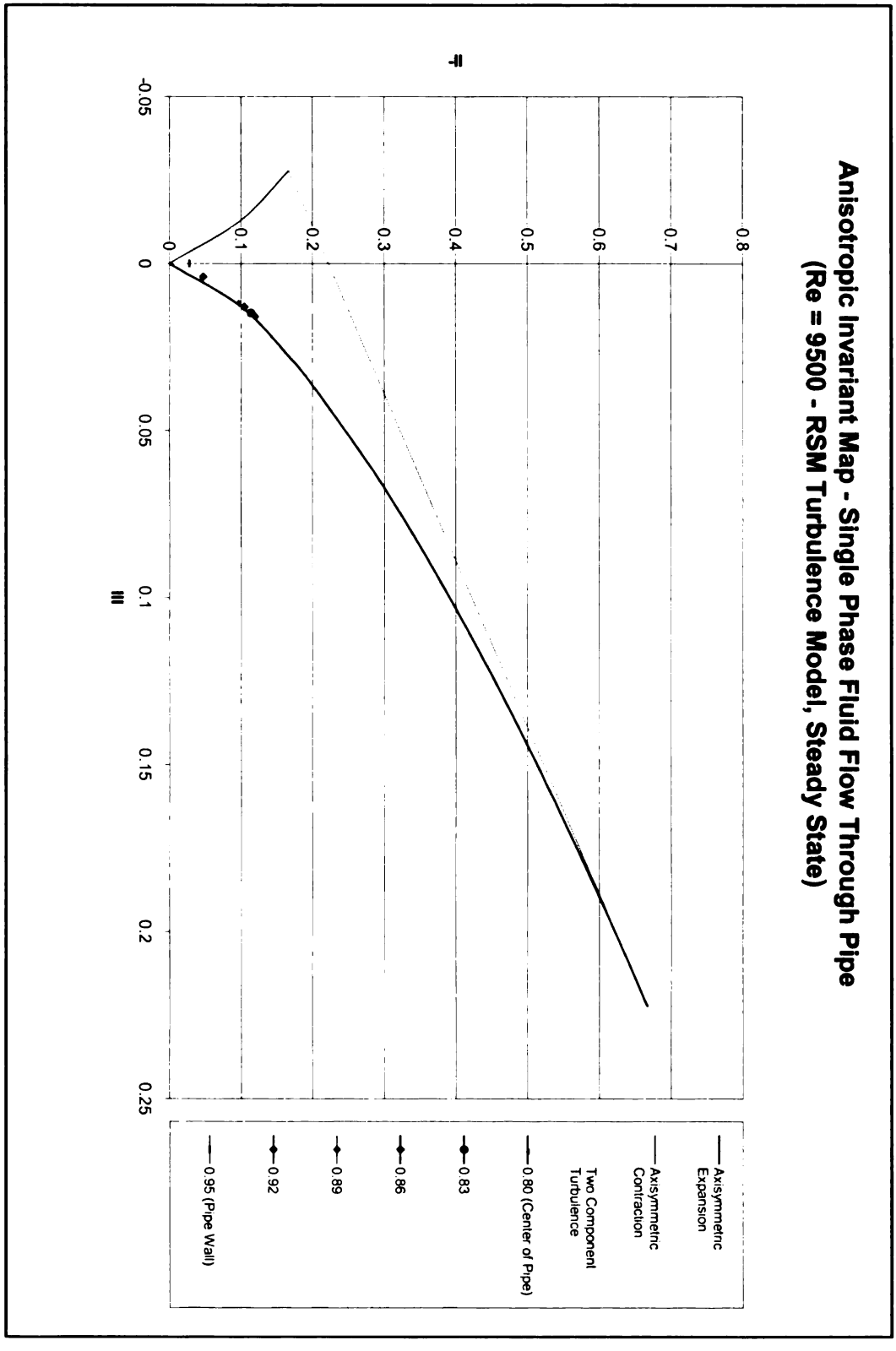

Figure 2.21: Plot of the Anisotropic Invariant Map generated for single phase fluid flow through a pipe using the Reynolds Stress Turbulence Model at Re No. = 9500.

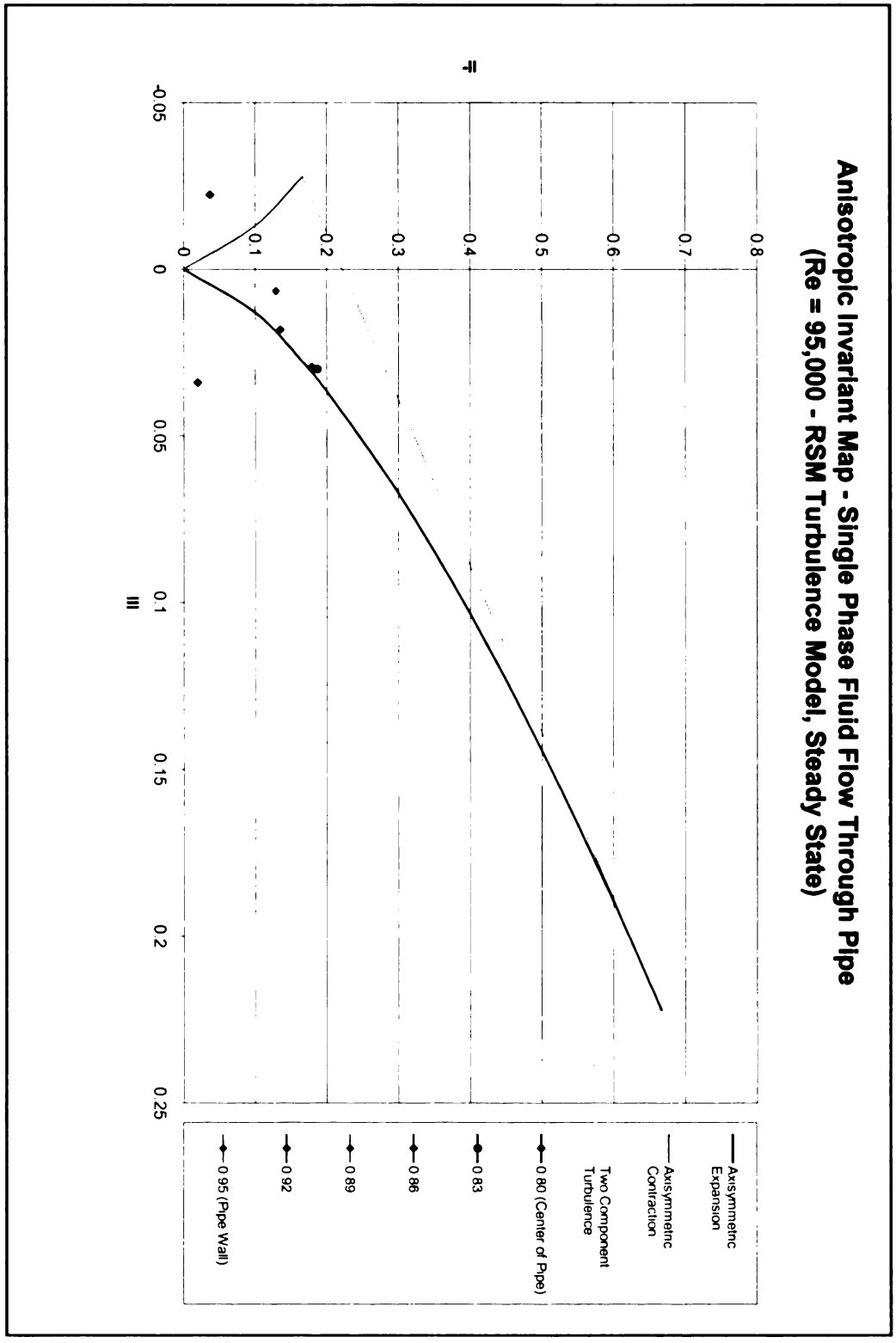

Figure 2.22: Plot of the Anisotropic Invariant Map generated for single phase fluid flow through a pipe using the Reynolds Stress Turbulence Model at Re No. = 95,000.

Figure 2.23 illustrates the Velocity Profile of Fully Developed Flow generated for single phase fluid flow through a pipe using the K-Epsilon and Reynolds Stress Turbulence Model at different Reynolds numbers. The theoretical data was calculated from equations 2.9 and 2.10 above. This figure shows that the Reynolds number value of 95,000 produces a velocity profile closest to the theoretical value for both turbulence models. The remaining velocity profiles over predict the turbulent flow at the lower Reynolds number values and especially the Realizable K-Epsilon model at a Reynolds number value of 1000.

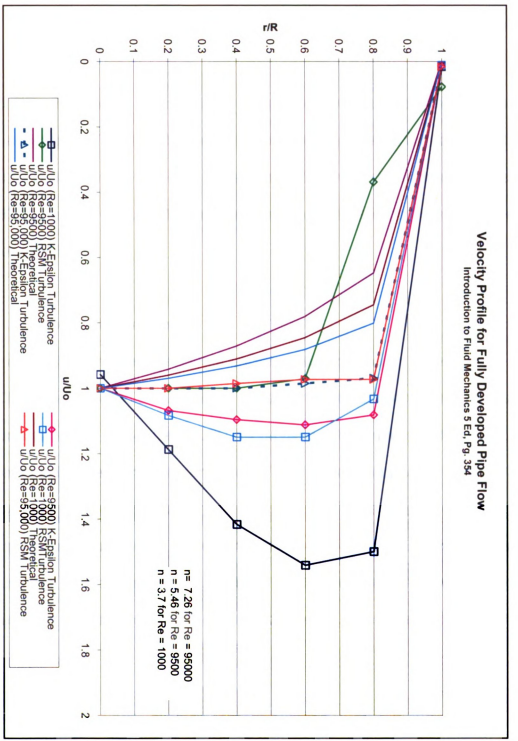

Figure 2.23: Plot of the Velocity Profile of Fully Developed Flow generated for single phase fluid flow through a pipe using the K-Epsilon and Reynolds Stress Turbulence Model at different Reynolds numbers.

III. NATURAL CONVECTION IN A 2D SQUARE ENCLOSURE

This chapter focuses on the two dimensional model of natural convection in a square enclosure. The two-dimensional model was evaluated with the use of Fluent CFD Software to simulate natural convection inside of a square enclosure. The 2D model was evaluated using the Realizable K-Epsilon turbulence model without radiation.

III.a. Problem Description

A two dimensional model of a square enclosure was created in order to learn how CFD could be used to numerically simulate natural convection heat transfer. This understanding of the use of CFD will be used subsequently in the next chapter to aid in the numerical simulation of the hot soaking phenomenon.

The square enclosure model is two-dimensional consisting of four walls. Figure 3.1 illustrates the geometry and quad mesh used to create the 2D model. Figure 3.2 illustrates a closer view of the quad mesh used to create the 2D model.

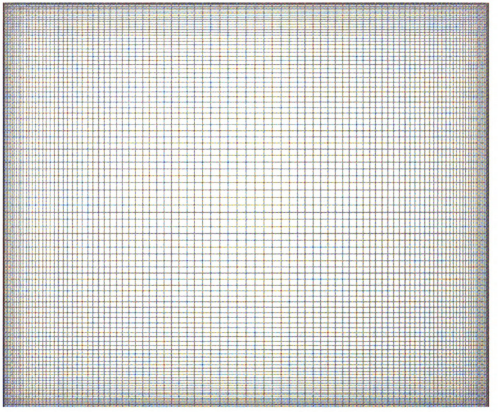

Figure 3.1: Plot of the quad grid mesh used for the 2D Enclosure.

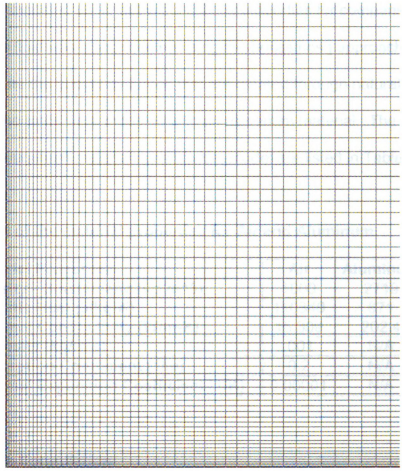

Figure 3.2: Plot of a closer view of the quad grid mesh used for the 2D Enclosure.

The 2D model has a height and width of 1.3 meters. The fluid inside the enclosure was modeled as air but with fictitious properties for comparison purposes. The fluid was also modeled using the Boussinesq approach to properly simulate the buoyancy forces that are created through natural convection. The walls were modeled with an aluminum material. The properties of the air and aluminum materials used in this model are listed in Table 3.1.

Table 3.1: List of the material properties for Air and Aluminum.

Material Properties	Air	Aluminum
Density - Boussinesq (kg/m^3)	1000	2719
Specific Heat (J/kg-K)	110340	871
Thermal Conductivity (W/m-K)	15.309	202.4
Viscosity (kg/m-s)	.001	N/A
Absorption Coefficient (1/m)	0.2	N/A
Thermal Expansion Coefficient (1/K)	0.00001	N/A

III.b. Problem Formulation

The operating conditions and boundary conditions used for CFD computations of the 2D natural convection model are specified below. The values of the operating and boundary conditions were selected so that the results can be compared to those of a tutorial model created by Fluent, Inc in order to understand how to model heat transfer. The model was analyzed using a steady state calculation.

Operating Conditions

The operating conditions used in this model were specified for the flow field. The

temperature of the flow field was specified as 1000 degrees Kelvin. The operating pressure was specified as 101,325 Pascals. Gravity was activated in the model and set to -6.96×10^{-5} m/s^2.

Boundary Conditions

Boundary conditions were used to set conditions for fluid flow and heat transfer on the boundary or surfaces of the model. The model for this study contains zone surfaces. Three different boundary types were used to define the boundary conditions for the different zones in the model. These boundary types are fluid, fixed temperature wall, and adiabatic wall. The fluid properties and operating conditions were previously described.

The fixed temperature wall zones were used to define the left and right walls of the enclosure. The fixed temperature of the right wall was specified as 2000 degrees Kelvin and the fixed temperature of the left wall was specified as 1000 degrees Kelvin. These specifications were used to describe a hot and cold wall. This temperature difference will induce the natural convection that will occur inside the enclosure. The adiabatic wall zones were applied to the top and bottom wall of the enclosure. The zones were used to specify a heat flux of 0 W/m^2.

The laminar flow model was used in the evaluation of the predictions of natural convection using the Fluent CFD Software. Turbulence modeling was not used

in this study in order to focus the buoyant flow by natural convection.

III.c. Governing Equations

Fluid flow and heat transfer were used to simulate natural convection in a 2D enclosure. The fluid flow is solved by the calculation of the following conservation of mass and momentum equations (Fluent 2005):

Conservation of Mass:

$$\frac{\partial \rho}{\partial t} + \nabla \cdot (\rho \vec{v}) = S_m \tag{3.1}$$

And the momentum equation in an inertial reference frame:

$$\frac{\partial}{\partial t}(\rho \vec{v}) + \nabla \cdot (\rho \vec{v} \vec{v}) = -\nabla p + \nabla \cdot (\bar{\bar{\tau}}) + \rho g + \vec{F} \tag{3.2}$$

Turbulence Modeling

The variation of the k-epsilon model chose for this study is the realizable k-epsilon model. The following are transport equations that FLUENT uses to calculate turbulence with the realizable k-epsilon model (Fluent 2005):

$$\frac{\partial}{\partial t}(\rho k) + \frac{\partial}{\partial x_j}(\rho k u_j) = \frac{\partial}{\partial x_j}\left[\left(\mu + \frac{\mu_t}{\sigma_k}\right)\frac{\partial k}{\partial x_j}\right] + G_k + G_b - \rho\varepsilon \tag{3.3}$$

$$\frac{\partial}{\partial t}(\rho \varepsilon) + \frac{\partial}{\partial x_j}(\rho \varepsilon u_j) = \frac{\partial}{\partial x_j}\left[\left(\mu + \frac{\mu_t}{\sigma_\varepsilon}\right)\frac{\partial \varepsilon}{\partial x_j}\right] + \rho C_1 S\varepsilon - \rho C_2 \frac{\varepsilon^2}{k + \sqrt{\nu\varepsilon}} + C_{1\varepsilon}\frac{\varepsilon}{k} C_{3\varepsilon} G_b \tag{3.4}$$

Heat Transfer

The energy equation was used for the calculation of heat transfer. All modes of heat transfer was calculated for this study. The modes of heat transfer are conduction, convection, and radiation. The following form of the energy equation was specified for the calculation of conduction and convection heat transfer for the Realizable K-Epsilon model (Fluent 2005):

$$\frac{\partial}{\partial t}(\rho E) + \frac{\partial}{\partial x_i}(u_i(\rho E + p)) = \frac{\partial}{\partial x_j}\left(k_{eff}\frac{\partial T}{\partial x_j} + u_i(\tau_{ij})_{eff} \right) \quad (3.5)$$

Nusselt Number Computation

The following are the analytical solutions for the computations of the average nusselt number published by different sources.

Experimental Calculation of the average Nusselt number:

$Nu_f = 0.062xRa^{1/3}$, (Elsherbiny et al., 1982) (3.6)

$Nu_f = 0.082xRa^{1/3,}$ (Markatos and Pericleous 1984) (3.7)

Empirical Correlation:

$$Nu_f = 0.18\left(\frac{\mathrm{Pr}}{0.2+\mathrm{Pr}}Ra_L\right)^{0.29}, \text{(Catton, 1978)} \quad (3.8)$$

Where Pr is the Prandtl Number and Ra_L is the Rayleigh Number.

III.d. Numerical Method of Solution

Hyper Mesh and FLUENT CFD programs were used in this study to numerically simulate natural convection in a 2D enclosure. To begin, the volume of the 2D model of a square enclosure was constructed with quad elements using Hyper Mesh. The volume in this model was used to simulate the air inside the enclosure. After the volume was generated, the model was imported into the FLUENT CFD program to numerically simulate natural convection.

III.e. Numerical Results

As mentioned previously, a two-dimensional model of an enclosure containing hot and cold walls was evaluated by using CFD software to predict natural convection in the square enclosure. The low temperature wall and a high temperature walls were created to produce natural convection inside an enclosure. The case was used to study the influence of turbulence on natural convection through the use of the realizable k-epsilon turbulence model. Figure 3.3 and Figure 3.4 illustrate the comparison between the model generated by Fluent, Inc. and the natural convection simulation model. The model generated by Fluent, Inc. contain was performed with laminar flow without radiation. As shown in Figure 3.3, the natural convection heat transfer process produces non-symmetric contours of the velocity stream function. The contours display a trend of warm air rising near the hot wall (then becoming cooled) and cool air falling near the cool wall (then becoming warm). Figure 3.4 shows that the use of the Realizable K-Epsilon produces a similar velocity stream function

distribution through natural convection but at a large magnitude. This is expected due to the higher velocity created by the introduction of turbulent flow. The percent error generated by the comparison of the model with realizable K-Epsilon turbulence to the model without turbulence is 23.86%.

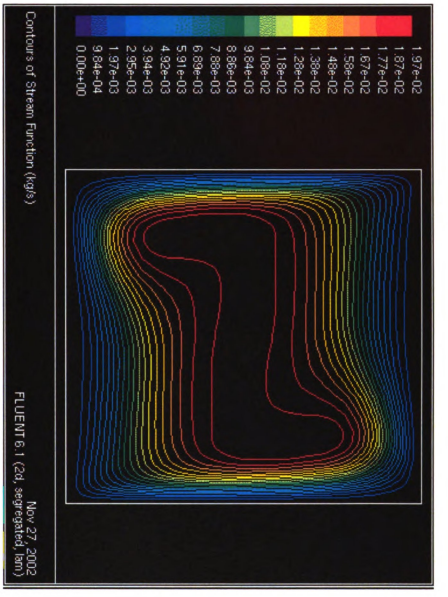

Figure 3.3: Plot of the contours of the stream function generated inside the 2D Enclosure for the model (with laminar flow but without radiation) published in Fluent 6.1 tutorial guide.

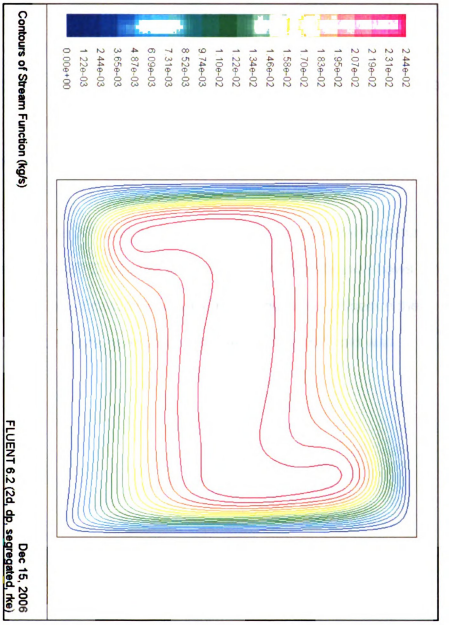

Figure 3.4: Plot of the contours of the stream function generated inside the 2D Enclosure for the model generated with Realizable K-Epsilon Turbulence model but without radiation.

Figure 3.5 illustrates the contours of the velocity magnitude generated inside the 2D Enclosure for the Realizable K-Epsilon Turbulence model without radiation. Although not shown, the vectors of the velocity magnitude are very close to the laminar flow model mentioned above. The figure shows the momentum boundary layer along both the hot (right) and the cold (left) walls.

Figure 3.6 and Figure 3.7 illustrate the contours of the static temperature generated inside the 2D Enclosure for both models. This figure shows that the use of the realizable K-Epsilon turbulence model does not influence the distribution of temperature generated between the hot and cold wall.

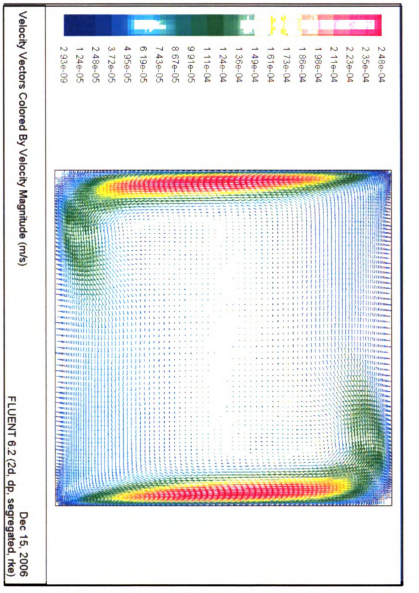

Figure 3.5: Plot of the vectors of the velocity magnitude generated inside the 2D Enclosure for the Realizable K-Epsilon Turbulence model without radiation.

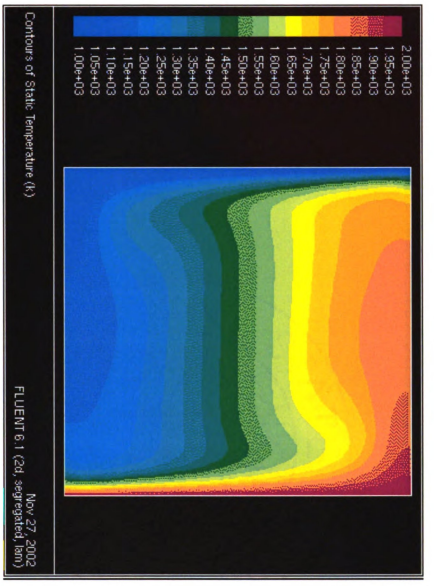

Figure 3.6: Plot of the contours of the static temperature generated inside the 2D Enclosure for the model (with laminar flow but without radiation) published in Fluent 6.1 tutorial guide.

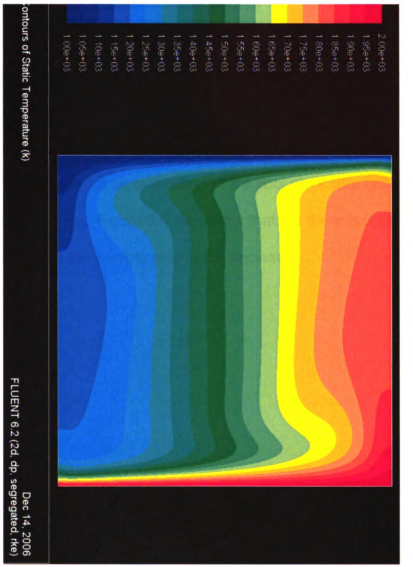

Figure 3.7: Plot of the contours of the static temperature generated inside the 2D Enclosure for the model generated with Realizable K-Epsilon Turbulence model but without radiation.

Figure 3.8 and Figure 3.9 illustrate the vectors of the velocity in the Y direction generated inside the 2D Enclosure for both models. The velocity graph represents the rising plume of lighter hot air on the right side of the enclosure, and the falling plume of heavier cool air on the left side of the enclosure. This behavior is caused by the buoyancy forces generated by changes in density and gravity. The rising of the hot air and falling of the cool air occurs faster in the model without turbulence. Figure 3.9 also show that the there is a region of cool air that is located near the warmer side of the enclosure.

Figure 3.8: Plot of the of the velocity in the Y direction generated inside the 2D Enclosure for the model (with laminar flow but without radiation) published in Fluent 6.1 tutorial guide.

Figure 3.9: Plot of the of the velocity in the Y direction generated inside the 2D Enclosure for the model generated with Realizable K-Epsilon Turbulence model but without radiation.

The model (with Laminar flow without radiation) published in Fluent 6.1 tutorial guide produces a total heat transfer flux of 138559.44 W/m^2. The Model generated with Realizable K-Epsilon Turbulence model but without radiation produces a total heat transfer flux of 139036 W/m^2. The percent difference between the laminar flow model and the realizable K-Epsilon turbulent flow model is 0.34%.

Figure 3.10 illustrates the plot of dimensionless height (in the y-direction) versus dimensionless temperature generated inside the 2D Enclosure. The graph displays data for the Realizable K-Epsilon turbulence model without radiation and for reference data calculated with an aspect ratio of 6 and a Rayleigh number of $Ra=7.12x10^{10}$ (Velusamy et al., 2001). It is shown that the trend of the 2D enclosure of the Realizable K-Epsilon turbulence model similar to the theoretical reference data. This shows that the model has generated a good predicting of natural convection in a 2D enclosure.

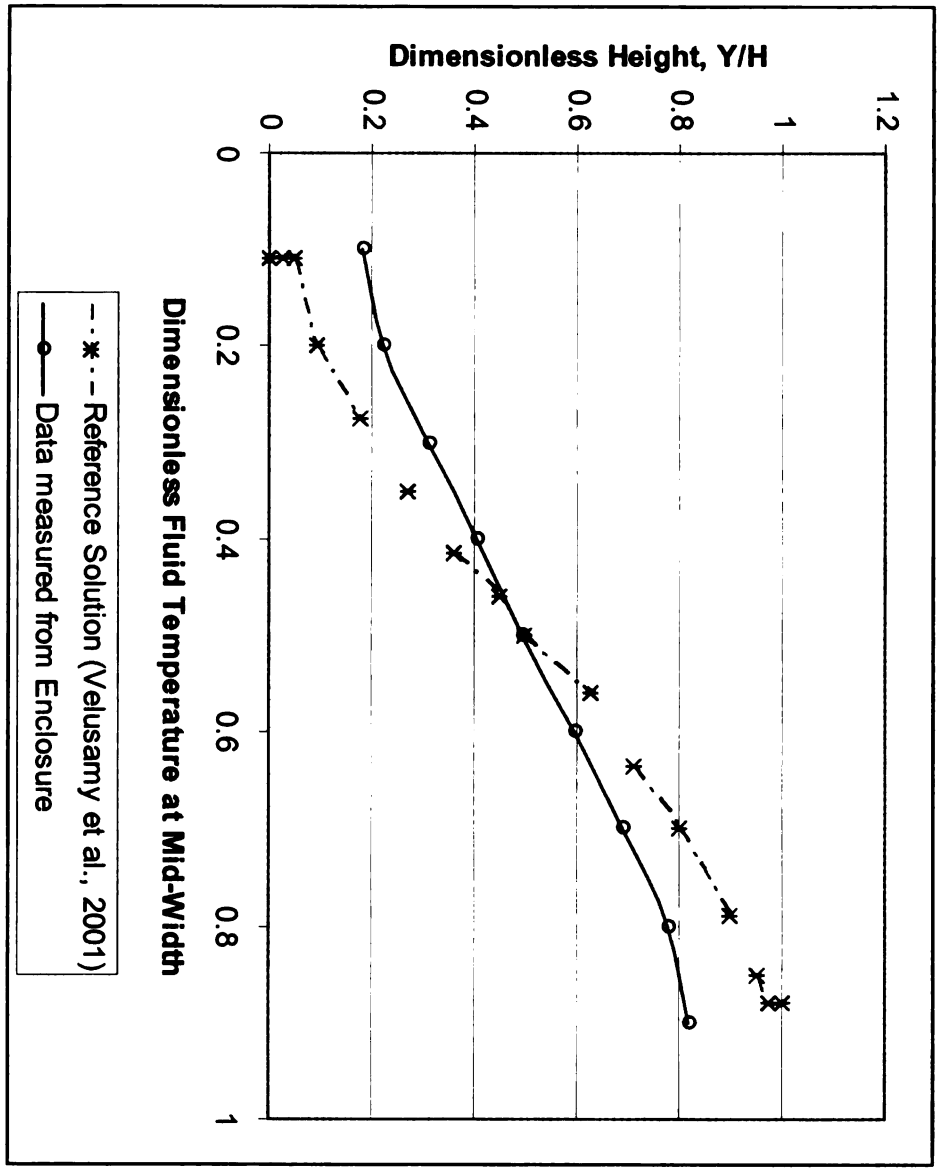

Figure 3.10: Plot of dimensionless height (in the y-direction) versus dimensionless temperature at mid-width generated inside the 2D Enclosure for: (a) the Realizable K-Epsilon turbulence model without radiation and (b) the reference solution measure with an aspect ratio of 6 and Rayleigh number of 7.12×10^{10} (Velusamy et al. (2001)).

Table 3.2 lists the computations of the average nusselt number as published by different sources. The predicted nusselt number computed by the Fluent CFD software is closest to the experimental calculation performed by Elsherbiny et al. (1982). The percent error calculated for the predicted measurement is 13.48%.

Table 3.2: List of the average Nusselt number published by different sources.

Rayleigh No.	10^{10}
Nusselt Number (Fluent - CFD prediction)	259.5072
Nusselt Number (Elsherbiny et al. – experiment)	228.7308
Nusselt Number (Markatos and Pericleous – experiment)	302.5149
Nusselt Number (Catton – Heat Transfer Book)	212.9974

IV. TWO-DIMENSIONAL MODEL OF CYLINDER ABOVE A HEATED PLATE

This chapter focuses on the two dimensional model which was used to investigate the hot soaking phenomenon using turbulence modeling and heat transfer. The two-dimensional model consists of a hollow cylinder above a heat hollow horizontal plate contained within a four-sided enclosure. The 2D model was evaluated using the Realizable K-Epsilon, K-Omega, and Reynolds Stress turbulence models. The 2D model was evaluated using different grid sizes ranging from coarse to fine.

IV.a. Problem Description

A simplified model was created in order to learn how CFD could be used to numerically the heat transfer of the hot soaking phenomenon. This understanding of the use of CFD was used to aid in the numerical simulation of the hot soaking process. The simplified model is two-dimensional consisting of a heated horizontal plate and a hollow cylinder both located inside of a four-sided enclosure. Figures 4.1 & 4.2 illustrate the geometry of the model. Figures 4.3, 4.4, & 4.5 illustrate the type of mesh generated for the model.

The outside surface of the heated plate is 0.086 meters long by 0.03 meters wide. The inside diameter of the hollow cylinder is 0.032 meters and the outside diameter is 0.04 meters. The enclosure is 1 meter in height by 1.5

meters wide. The thickness of the hollow cylinder and heated plate is 0.004 meters.

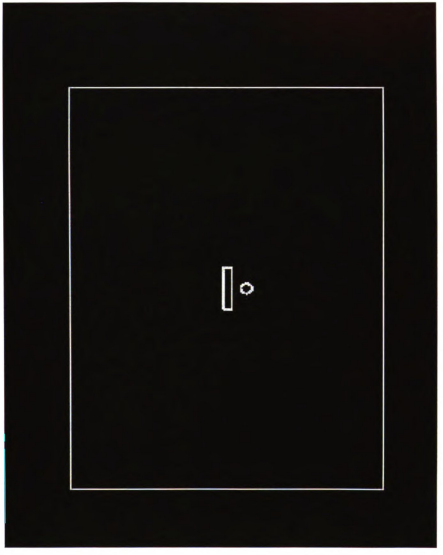

Figure 4.1: Plot of the geometry of the 2D model of a cylinder above a heated plate.

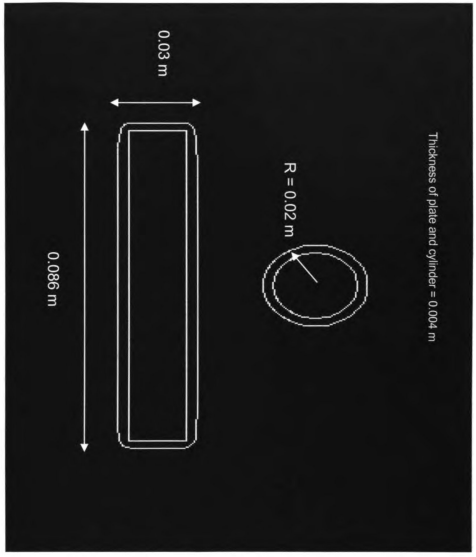

Figure 4.2: Plot of a closer view of the geometry of the 2D model of a cylinder above a heated plate.

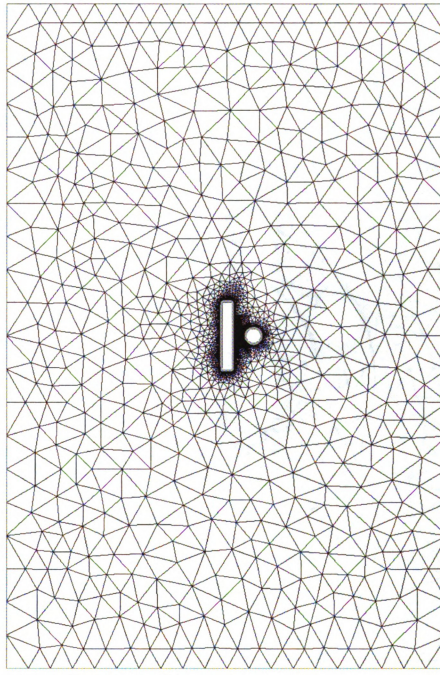

Figure 4.3: Plot of the meshed domain of the 2D model of a Cylinder above a heated plate.

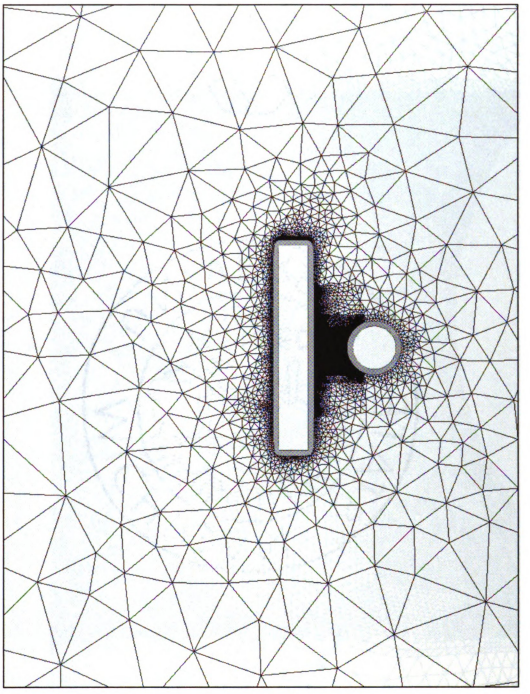

Figure 4.4: Plot of a closer view of the meshed domain of the 2D model of a Cylinder above a heated plate.

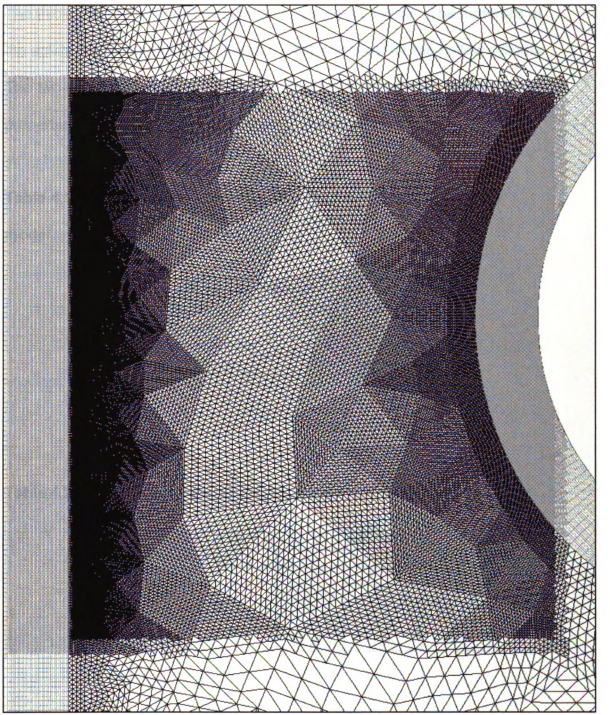

Figure 4.5: Plot of the triangular and quad shaped elements used to mesh the domain of the 2D model of a Cylinder above a heated plate.

The thickness of each component was modeled as a solid. The materials of the solids are aluminum for the heated plate and steel for the hollow cylinder. The two-dimensional model component materials are listed in Table 4.1. The properties of air and the materials used in this model are listed in Table 4.2.

Table 4.1: List of the materials used for the components of the 2D model.

2D Model Component Materials		
Component	**Zone**	**Material**
Enclosure	Wall	Aluminum
Hollow Cylinder	Wall	Steel
Heated Plate	Wall	Aluminum

Table 4.2: List of the properties of Air, Aluminum, and Steel.

Properties of Materials for 2D Simplified Model			
Thermo-physical Property	**Air**	**Aluminum**	**Steel**
Density (kg/m^3)	1.225	2719	8030
Specific Heat	1006.43	871	502.48
Thermal Conductivity	0.0242	202.4	16.27
Viscosity	1.79E-05	N/A	N/A
Molecular Weight	28.966	N/A	N/A

IV.b. Problem Formulation

The initial conditions and boundary conditions that were used for the 2D model will now be specified. This model was analyzed using the steady state condition. The steady state calculation of the 2D model was used as the initial conditions for the transient analysis of the 2D model.

Initial Conditions

The initial conditions used in this model were specified for the flow field and the walls of the components. The temperature of the flow field was specified as 353.15 degrees Kelvin. The operating pressure was specified as 101,325 Pascals. The initial velocity was specified as 13.89 m/s.

The initial temperature of the interior wall of the heated plate was specified as 911.15 degrees Kelvin. The other remaining surfaces of the heated plate and hollow cylinder were modeled as adiabatic walls with a heat flux of 0 W/m^2. The front wall of the four-sided enclosure was modeled as a velocity inlet. The rear wall of the four-sided enclosure was modeled as a pressure outlet, the gauge pressure was specified as 0 Pascals and the backflow total temperature was specified as 353.15 K. The bottom wall of the four-sided enclosure was modeled as a moving, adiabatic wall. The velocity of the moving wall was defined as 13.89 m/s. The heat flux of the wall was specified as 0 W/m^2 with an internal emissivity of 1. The top wall of the four-sided enclosure was modeled as symmetry, due to the nature of this

boundary condition, the heat flux, normal velocity, and velocity gradients are assumed to have a value of zero.

Boundary Conditions for Transient Analysis

Boundary conditions were used to set conditions for fluid flow and heat transfer on the boundary or surfaces of the model. Five different boundary types were used to define the boundary conditions for the different zones in this model. These types are fluid, solid, fixed temperature wall, fixed heat flux wall, and coupled wall boundary conditions.

The fluid zone and fixed temperature wall zones have been defined in the previous chapter. The solid zone was used to define the boundary conditions of the solid used to represent the thickness of the cylinder and the horizontal plate. A solid zone represents a group of cells that is used to solve conduction heat transfer. In this model, prisms were extruded to create solids. Prisms were extruded on both the cylinder and plate to represent the thickness of the components in order to calculate conjugate heat transfer. Conjugate heat transfer was used to determine the conduction through the wall of the horizontal plate as well as the radiation from the surface of the horizontal plate to the cylinder. The solid zone also participates in radiation.

Wall zones were used to define the thermal boundary conditions at the wall. The wall zones used in this model are the enclosure, the plate, and the

cylinder. The fixed heat flux wall boundary condition was used for the walls of the enclosure, the outer surface of the horizontal plate, and both surfaces of the cylinder. The heat flux was set at zero to define an adiabatic wall. The fixed heat flux boundary condition represents the temperature gradient at the wall of the modeled components by using Fourier's Law and is given by (Fluent 2005):

$$q_x'' = -k\frac{\partial T}{\partial x} = 0 \qquad (4.1)$$

This boundary condition can be referred to as the Neumann condition or a boundary condition of the second kind. The wall thickness and heat generation rate of the walls modeled were specified as zero.

The walls of the outer plate surface and outer diameter of the cylinder were modeled as coupled two-sided walls. When a wall zone contains a solid or a fluid on each side, it is considered to be a two-sided wall and shadow zones are created right next to the wall zone. Shadow zones are used to specify boundary conditions distinctly on each side of the zone. The wall zones and shadow zones of the plate and outer diameter of the cylinder are coupled together. Coupled means that the both zones are grouped together and the heat transfer is calculated directly from the solution in the adjacent cells without specifying any additional boundary conditions.

The horizontal plate represents the source of heat in this study. A fixed temperature wall boundary condition was applied to the wall of the inner surface of the horizontal plate to simulate the temperature of the heated plate. A temperature profile was used to represent the temperature of the inner surface of horizontal plate as it changed with time. This temperature profile is shown in the Figure 4.6 below.

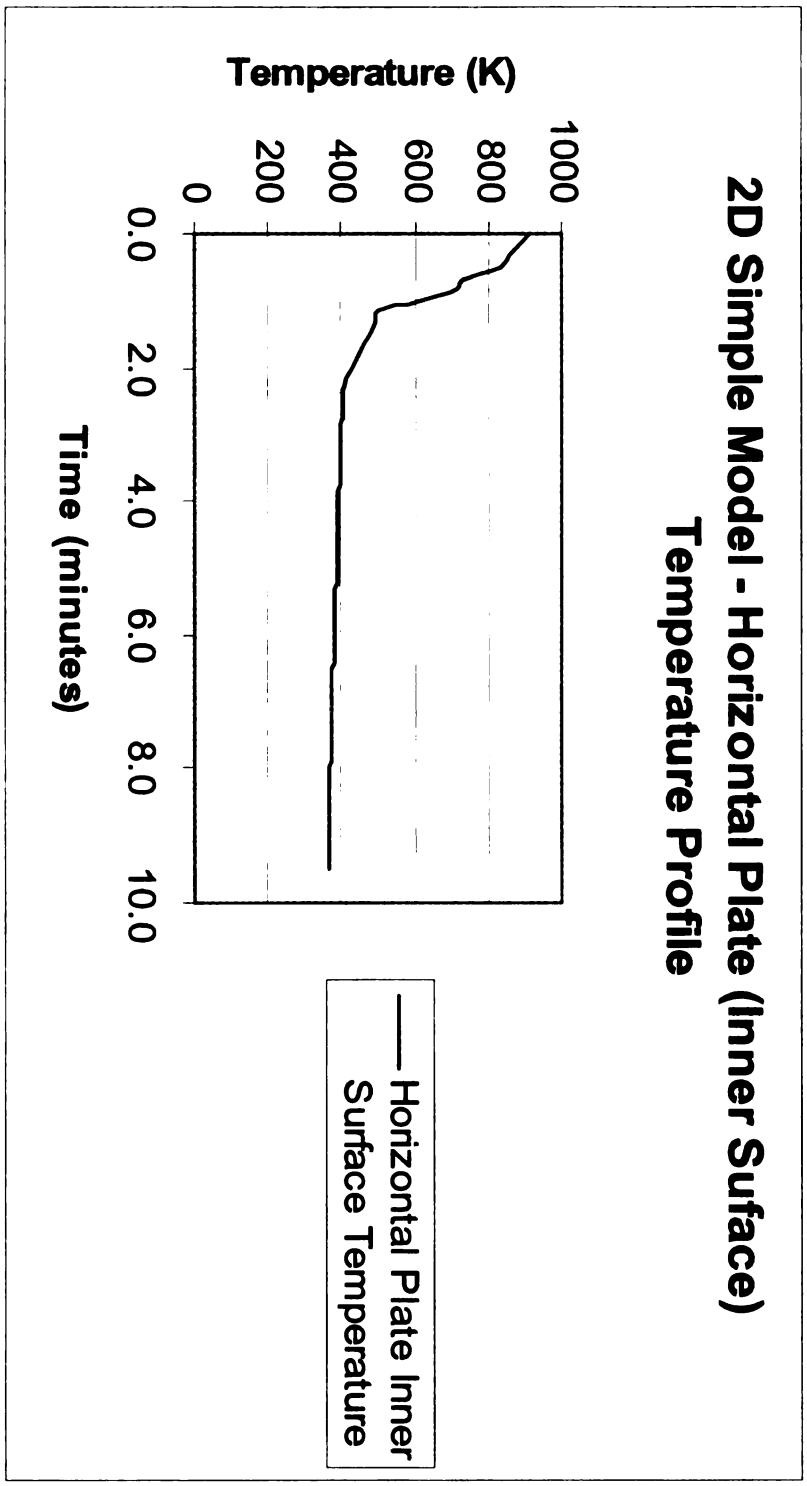

Figure 4.6: Plot of the temperature profile specified for the inner surface of the heated plate.

Other boundary conditions were also defined on the walls of this model. The walls that were defined in this model (with the exception of the bottom wall of the enclosure) were specified as stationary, non-moving walls. The shear condition was defined at these walls as the slip wall condition that is equivalent to zero shear stress. The roughness value of the walls was set to zero to represent smooth walls. The radiation is defined at the walls as diffuse and with an emissivity of one.

IV.c. Governing Equations

Fluid flow and heat transfer were used to simulate the hot soaking phenomenon of the 2D model of a hollow cylinder above a hollow heated plate. The fluid flow is solved by the calculation of the following conservation of mass and momentum equations (Fluent 2005):

Conservation of Mass Equation:

$$\frac{\partial \rho}{\partial t} + \nabla \cdot (\rho \vec{v}) = S_m$$

(4.2)

Momentum Equation in an inertial reference frame:

$$\frac{\partial}{\partial t}(\rho \vec{v}) + \nabla \cdot (\rho \vec{v} \vec{v}) = -\nabla p + \nabla \cdot (\bar{\bar{\tau}}) + \rho g + \vec{F}$$

(4.3)

Turbulence Modeling

The governing equations used for the K-Epsilon and Reynolds Stress Model were defined in the previous chapter. The variation of the k-omega model chosen for this study is the standard k-omega model. The following are the transport equations that were used to calculate turbulence with the standard k-omega model (Fluent 2005):

$$\frac{\partial}{\partial t}(\rho k) + \frac{\partial}{\partial x_i}(\rho k u_i) = \frac{\partial}{\partial x_j}\left[\Gamma_k \frac{\partial k}{\partial x_j}\right] + G_k \qquad (4.4)$$

$$\frac{\partial}{\partial t}(\rho w) + \frac{\partial}{\partial x_i}(\rho w u_i) = \frac{\partial}{\partial x_j}\left[\Gamma_w \frac{\partial w}{\partial x_j}\right] + G_w \qquad (4.5)$$

Heat Transfer

The energy equation was used for the calculation of heat transfer. All modes of

heat transfer was calculated for this study. The modes of heat transfer are

conduction, convection, and radiation. The following form of the energy equation

was specified for the calculation of conduction and convection heat transfer

(Fluent 2005):

$$\frac{\partial}{\partial t}(\rho E) + \frac{\partial}{\partial x_i}(u_i(\rho E + p)) = \frac{\partial}{\partial x_j}\left(k_{eff}\frac{\partial T}{\partial x_j} + u_i(\tau_{ij})_{eff}\right)$$

(4.6)

The following equation was used to solve radiation heat transfer for an absorbing, emitting, and scattering medium at position $\vec{r}$ in the direction $\vec{s}$. This equation represents the Discrete Ordinates Model of radiation.

$$\frac{\partial I(\vec{r},\vec{s})}{\partial t} + (a+\sigma_s)I(\vec{r},\vec{s}) = an^2\frac{\sigma T^4}{\pi} + \frac{\sigma_s}{4\pi}\int_0^{4\pi} I(\vec{r},\vec{s}')\Phi(\vec{s},\vec{s}')d\Omega' \quad (4.7)$$

Pressure Distribution Computation

The following analytical equation was used to compute the surface pressure distributions for boundary layer flow around the cylinder above the heated plate.

Pressure Distribution:

$$C_p = 1 - 4\sin^2(theta), \text{ (Munson et al., 2002)} \quad (4.8)$$

IV.d. Anisotropic Invariant Map

The anisotropic invariant map was used to evaluate the numerical predictions of Hot soaking in this study. In this study, the Reynolds stress tensors will be determined for the Realizable K-Epsilon, K-Omega, and Reynolds Stress turbulence models. The derivations of anisotropy for the Realizable K-Epsilon and Reynolds Stress model will be similar to the derivations discussed in the previous chapter. However, since a 2D model was used for this study, the

Z – component of the Reynolds stress has a value of zero. The following equations were used to determine the anisotropy of the K-Omega turbulence model utilizing the Boussinesq Approach:

$$-\overline{\rho u_i' u_j'} = \mu_t\left(\frac{\partial u_i}{\partial x_j}+\frac{\partial u_j}{\partial x_i}\right)-\frac{2}{3}\left(\rho k+\mu_t\frac{\partial u_i}{\partial x_i}\right)\delta_{ij}$$

(4.9)

$$\overline{u'u'} = -\frac{\mu_t}{\rho}\left(2\frac{\partial u}{\partial x}\right)+\frac{2}{3}\left(k+\frac{\mu_t}{\rho}\frac{\partial u}{\partial x}\right)$$

(4.10)

$$\overline{v'v'} = -\frac{\mu_t}{\rho}\left(2\frac{\partial v}{\partial y}\right)+\frac{2}{3}\left(k+\frac{\mu_t}{\rho}\frac{\partial v}{\partial y}\right)$$

(4.11)

$$\overline{w'w'} = 0$$

(4.12)

$$\overline{u'v'} = -\frac{\mu_t}{\rho}\left(\frac{\partial u}{\partial y}+\frac{\partial v}{\partial x}\right)$$

(4.13)

An additional study was created in order to determine the physical realizability of the turbulence generation influence by heat transfer. The focus of this study was to evaluate the mean temperature in addition to the Reynolds stresses generated by turbulence which the following:

$$< u'u'T >$$

(4.14)

T is the mean temperature calculated by the Fluent CFD code in degrees Kelvin.

The instantaneous change in mean temperature can be determined by adding the fluctuating component of temperature (T') to the steady component of temperature <T>:

$$T = T' + < T >$$

(4.16)

Multiplying this equation by the any component of the Reynolds stress, will produce the following:

$$< u'u'T >=< u'u'T' > + < u'u' >< T >$$

(4.17)

$< u'u'T' >$ was determined from the following equation of the turbulent diffusion of the heat flux:

$$< u'u'T' >= -C_\theta \frac{k}{\varepsilon}\left(\overline{u'u'}\frac{\partial \overline{u'T}}{\partial x}\right)$$

(4.18)

where $-C_\theta$ represents a coefficient with a value of 0.22. The term $\left(\frac{\partial \overline{u'T}}{\partial x}\right)$ in the expression above represents the gradient of the heat flux $< u'T >$. The expression $< u'u' >< T >$ in equation (4.18) represents the product of the Reynolds stress and mean temperature. The addition of equation (4.17) and

equation (4.18) was used to evaluate the variance of turbulence and heat transfer for this model:

$$< u'u'T >= -C_\theta \frac{k}{\varepsilon}\left(\overline{u'u'}\frac{\partial \overline{u'T}}{\partial x}\right) + < u'u' >< T >$$

(4.19)

This term was evaluated in a similar matter to the Reynolds stress term in Chapter II by calculating the second and third invariants to create an Anisotropic Invariant map of turbulent heat transfer. Figure 4.7 represents an illustration of the region where the turbulence anisotropy was calculated to evaluate the anisotropic invariance of the turbulent heat transfer generated in this model. The turbulent anisotropy was calculated along the line between bottom wall of cylinder and top of heated plate centered at x = 0.

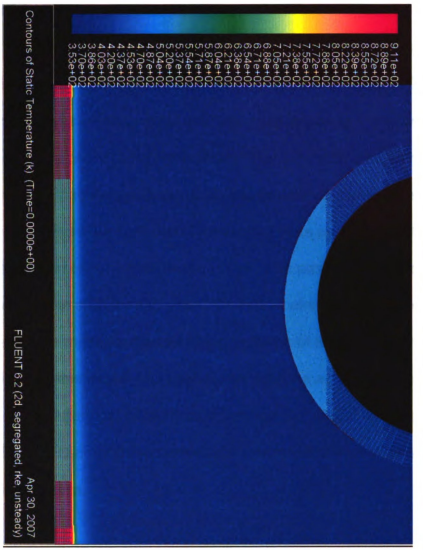

Figure 4.7: Illustration of the region (line between bottom wall of cylinder and top of heated plate centered at x = 0) where the turbulence anisotropy was calculated to evaluate the anisotropic invariance of the turbulent heat transfer generated by the model in equation (4.19).

IV.e. Numerical Method of Solution

HyperMesh, TGrid, and FLUENT CFD programs were also used in this study to numerically simulate the hot soaking process as mentioned above. To begin, a 2D model was constructed of a hollow cylinder above a hollow plate located inside an enclosure using HyperMesh. The 2D model was then imported into the TGrid program to generate the volume elements. Prisms were initially grown from the surfaces of the heated plate and the cylinder for the proper calculation of conjugate heat transfer. The prisms will be modeled as the solid wall of the cylinder and plate. Triangular elements were then used to generate the mesh for the remaining surfaces of the model. The triangular volume in this model was used to simulate the air between the cylinder and plate. After the volume was generated, the model was imported into the FLUENT CFD program to numerically simulate the phenomenon of the hot soaking process.

The focus of this study was to create a numerical simulation process of the hot soaking phenomenon. This was achieved by performing an analysis study of the heat transfer process between the cylinder and plate. To understand the hot soaking process, the dominant mode of heat transfer had to be determined. Conduction, convection, and radiation were studied to establish the dominant mode of heat transfer. Two cases were studied to determine the best process of numerical simulation of the hot soaking

process using CFD. These two cases were used to study the grid sensitivity and turbulence modeling to evaluate how they both affect the hot soaking process.

Grid Sensitivity Study

Grids are elements that consist of triangular or equilateral cells and nodes commonly known as grid points. There are many combinations of grids that can be used to build models. Two types of grids that are most commonly used are structured or unstructured grids. Structured grids consist of grids that are generated in a uniform manner and that are similar in shape and size. Unstructured grids are comprised of a grid patterns that are not uniform. Unstructured grids are rarely the same shape or size. The geometries primarily used in fluid flow and heat transfer problems are complex. The construction of grids for a complex geometry using structured elements such as quadrilateral and hexahedral is very time consuming and nearly unfeasible. The best type of grid to use for a complex geometry is an unstructured grid with triangular and tetrahedral elements because it is less time consuming and allows the use of fewer elements.

Hypermesh and Tgrid are pre-processors that were used primarily in this study for the creation of the 2D triangular unstructured mesh. The 2D model was then imported into the Fluent program, which was used to create the different topologies using solution-adaption grid refinement. Solution-

adaption grid refinement was used to refine the grids that are located between the cylinder and plate. The grids in this area are important to the evaluation the hot soaking phenomenon. To adapt grids in the FLUENT program, the region adaption method was used. This method allows the user to define and select the specific region of cells for grid adaption. The first 2D volume mesh generated consisted of coarse grids that did not produce accurate data (See Figure 4.8(a)). As a result, "finer" meshes were created between the cylinder and plate to produce more accurate results. The finest mesh which produced the most accurate results is shown in Figure 4.8(d).

Each of the grid meshes were studied in order to determine how the results generated from the numerical simulations were affected by the size of the grid. This is considered a Grid Sensitivity study. If the solution is dependent upon the grid size, then an optimum grid size will need to be use when creating a simulation of the hot soaking process. If the solution is not dependent upon the grid size, less grids can be used which can decrease the time it takes to create the model and increase the speed of the calculations.

IV.f. Numerical Results

As mentioned previously, two different cases were examined to determine the optimal process to numerically simulate the hot soaking process. These two cases were used to study the grid sensitivity and turbulence modeling. To examine the grid sensitivity, the 2D model was modified by creating a range

of models containing different size elements located between the heated plate and cylinder. The main focus of this examination is the affect the grid size has on the accuracy of the results. Finally, to examine turbulence modeling, the boundary conditions of the 2D model will be modified by using the Realizable K-Epsilon, K-Omega, and Reynolds Stress turbulence models.

Case I: Grid Sensitivity Study

Figure 3.7 Illustrates the different types of grid adaption refinements that were generated between the cylinder and heated plate. Four different grid types were generated for the grid sensitivity study. Figure 4.8 (a) represents the grid adaption model Type 1. This grid is course compared to the other three grid adaption models. Figure 4.8 (b) represents the grid adaption model Type 2 which displays one level of grid refinement. Figure 4.8 (c) represents the grid adaption model Type 3 which displays a level of refinement greater than the Type 2 grid refinement. Finally, Figure 4.8 (d) represents the grid adaption model Type 4 which displays the finest grid refinement.

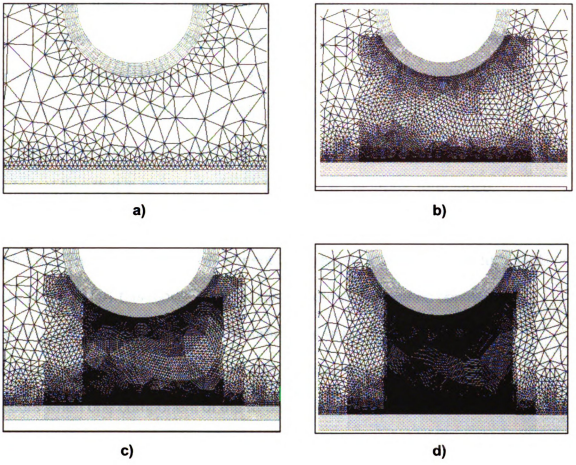

Figure 4.8: Plot of the different types of grid adaption refinements that were generated between the cylinder and heated plate: (a) represents Grid Type 1 (the course grid), (b) represents Grid Type 2 (c) represents Grid Type 3 and (d) represents Grid Type 4 (the finest grid).

Figures 4.9 through 4.12 illustrate the Anisotropic invariant Maps generated from the steady state calculation of the Reynolds Stress Model for the four different grid types. In Figures 4.9, 4.10, and Figure 4.11, the grid types used produced both physically unrealizable and realizable turbulent flow. The realizable turbulence generated by these grid configurations produces turbulent flow that is close to isotropic turbulence. Isotropic turbulence represents turbulent flow with zero anisotropy. In Figure 4.12, the turbulence generated by the type 4 grid refinement is physically realizable. The turbulent flow produced by this model tends to range from axisymmetric contraction ("Disk-Like") turbulence to isotropic turbulence according to the diagram. According to Krogstag and Simonsen (2005), the "Disk-Like" turbulence occurs when one component of the turbulent kinetic energy is smaller than the other two components of turbulent kinetic energy which are equal.

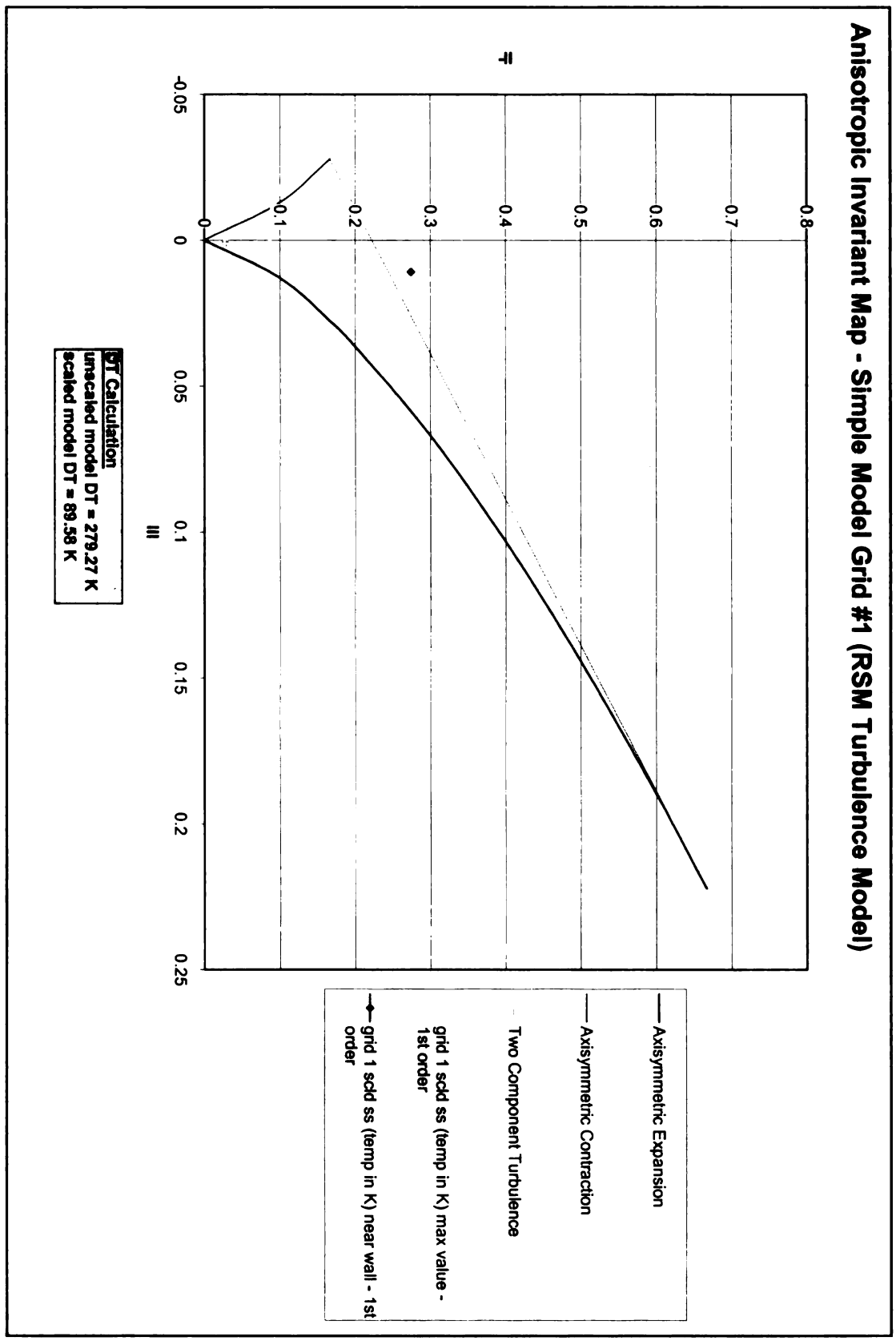

Figure 4.9: Plot of the Anisotropic Invariant Map generated from the steady state calculation of the Reynolds Stress Model for Grid Type 1.

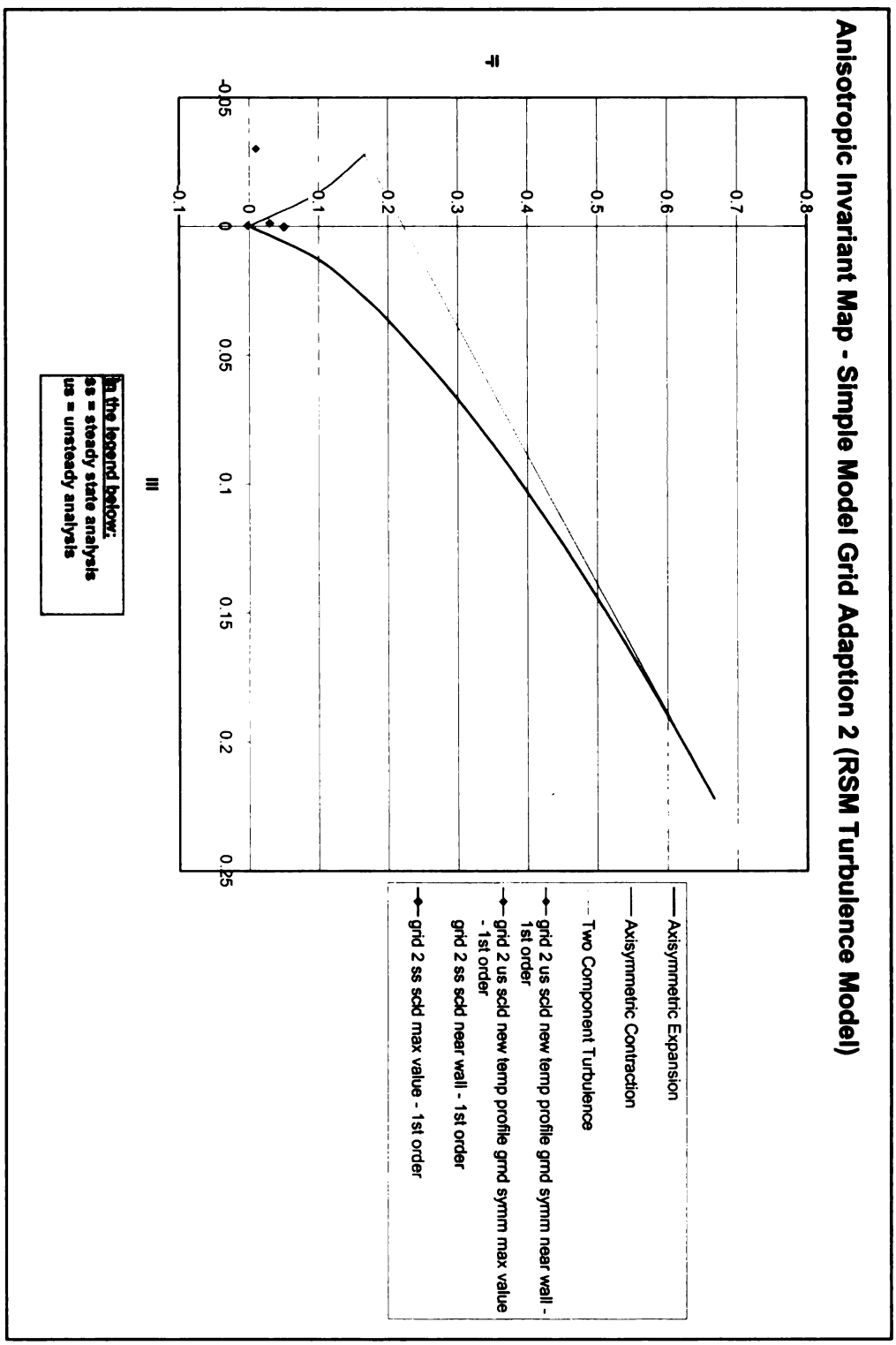

Figure 4.10: Plot of the Anisotropic Invariant Map generated from the steady state and transient calculation of the Reynolds Stress Model for Grid Type 2.

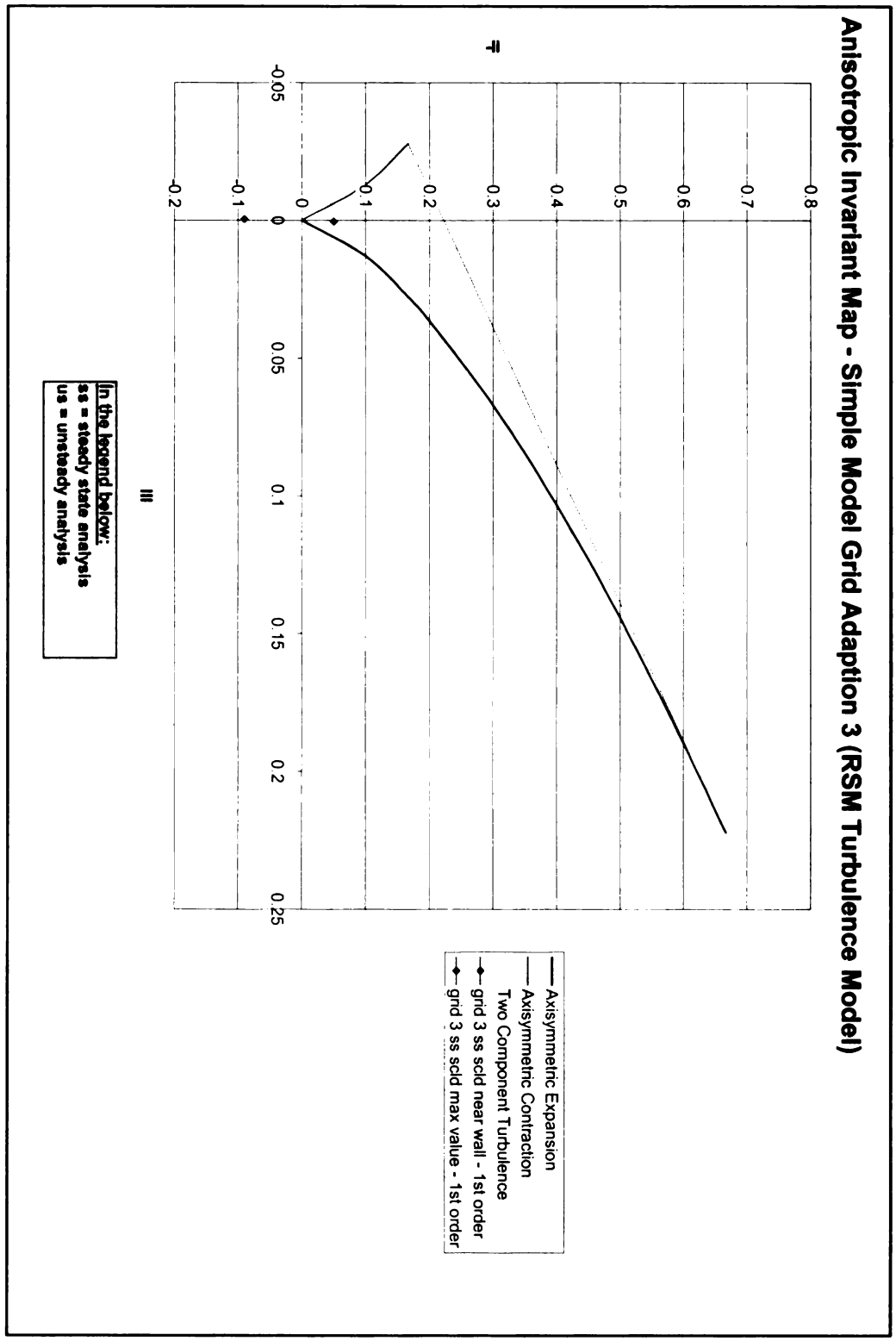

Figure 4.11: Plot of the Anisotropic Invariant Map generated from the steady state calculation of the Reynolds Stress Model for Grid Type 3.

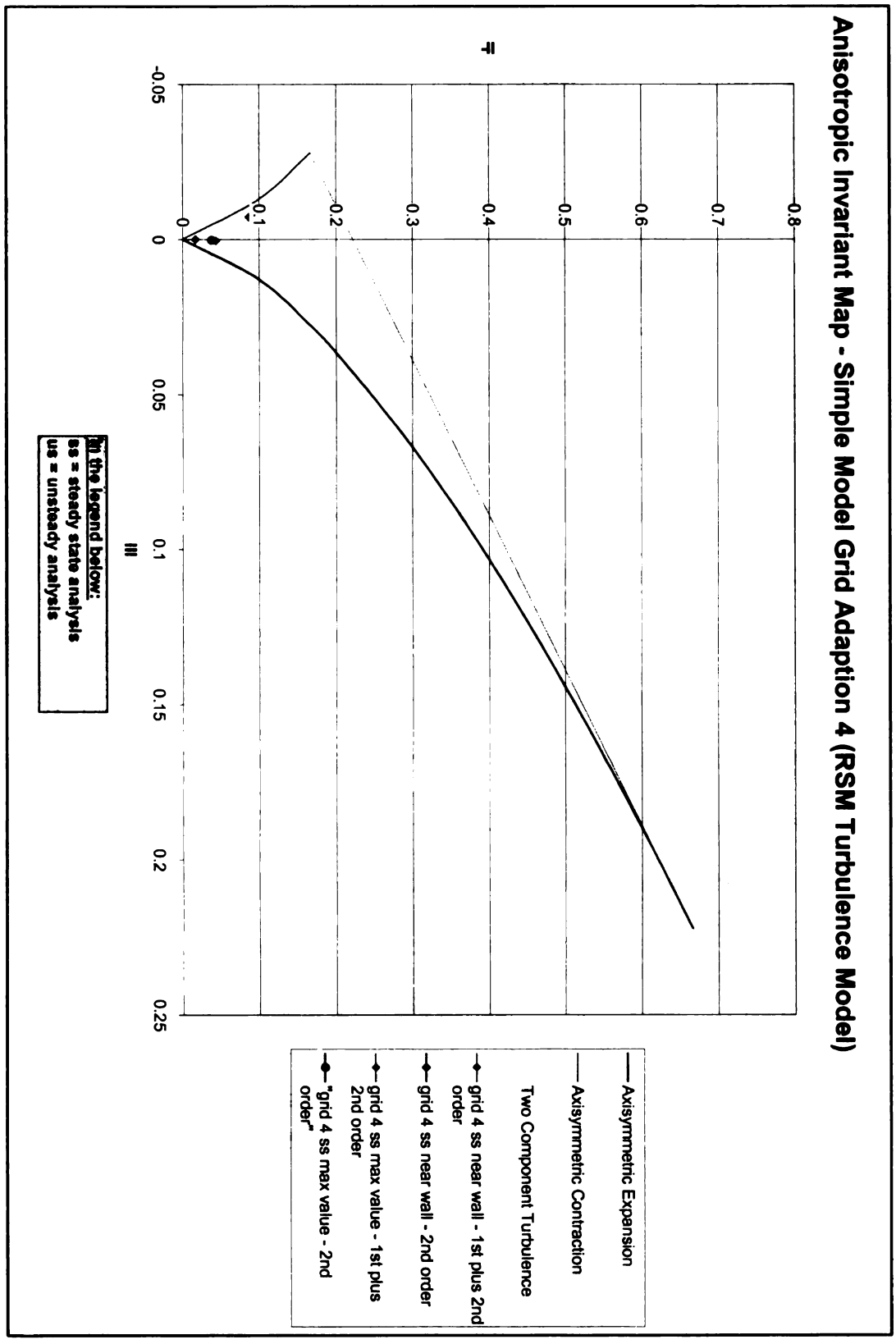

Figure 4.12: Plot of the Anisotropic Invariant Map generated from the steady state calculation of the Reynolds Stress Model for Grid Type 4.

Figure 4.13 illustrates the Anisotropic Invariant Map generated from the model's maximum anisotropy values of the transient calculation of the K-Epsilon Model for Grid Type 4. The anisotropy was calculated from the maximum Reynolds stress values of the entire model. It is shown in this Figure that anisotropy decreases as time increases. The turbulent flow becomes more realizable as the length of time to calculate the model increases. Figure 4.14 displays the anisotropy calculations generated for the last two intervals of time equal to 1,155.5 seconds and 1,173 seconds. The turbulence flow becomes physically realizable after the time interval of 990.5 seconds according to Table 4.3. The turbulent flow of this model tends to display axisymmetric expansion ("Rod-like") turbulence. The "Rod-like" turbulence was defined previously in Chapter II. Figure 4.15 illustrates the Anisotropic Invariant Map generated from the transient calculation of the K-Epsilon Model for Grid Type 4. These anisotropy values were calculated near the bottom wall of the cylinder. The turbulence generated for this model over time is physically realizable. The turbulence generated is near the axisymmetric contraction and isotropic zones.

Figure 4.13: Plot of the Anisotropic Invariant Map generated from the transient calculation of the K-Epsilon Model for Grid Type 4 (Maximum Anisotropy Value of Model).

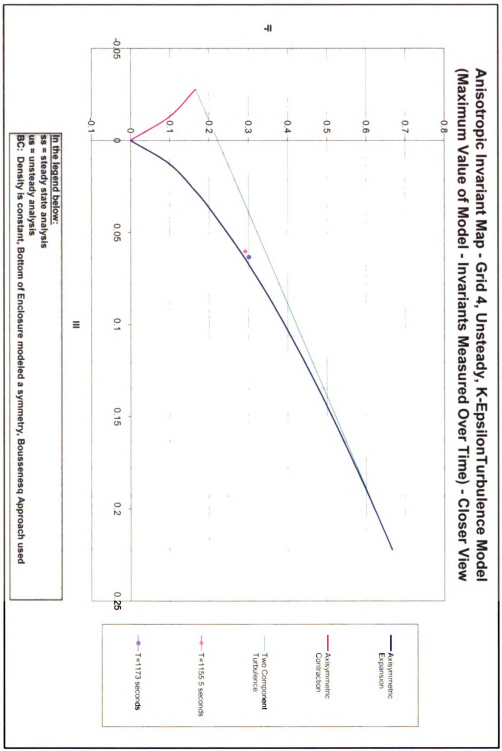

Figure 4.14: Plot of a closer view of the Anisotropic Invariant Map generated from the transient calculation of the K-Epsilon Model for Grid Type 4 (Maximum Anisotropy Value of Model).

Table 4.3: List of the second (II) and third (III) scalar invariants of anisotropy over a range of time from zero seconds to 1,173 seconds generated from calculating the maximum anisotropy value of model for the Grid Type 4 K-Epsilon Model.

Time (seconds)	Invariant -II (Max Value)	Invariant III (Max Value)
0	3497.45	1165.78
60	4154.35	1384.75
120	832.78	277.56
180	544.12	181.34
240	290.30	96.73
360	4283.64	1427.84
540	210.36	70.08
660	15.19	5.03
840	3.15	1.01
990.5	-0.29	-0.13
1155.5	0.29	0.06
1173	0.30	0.06
Shaded area represents unrealizable turbulence anisotropy		

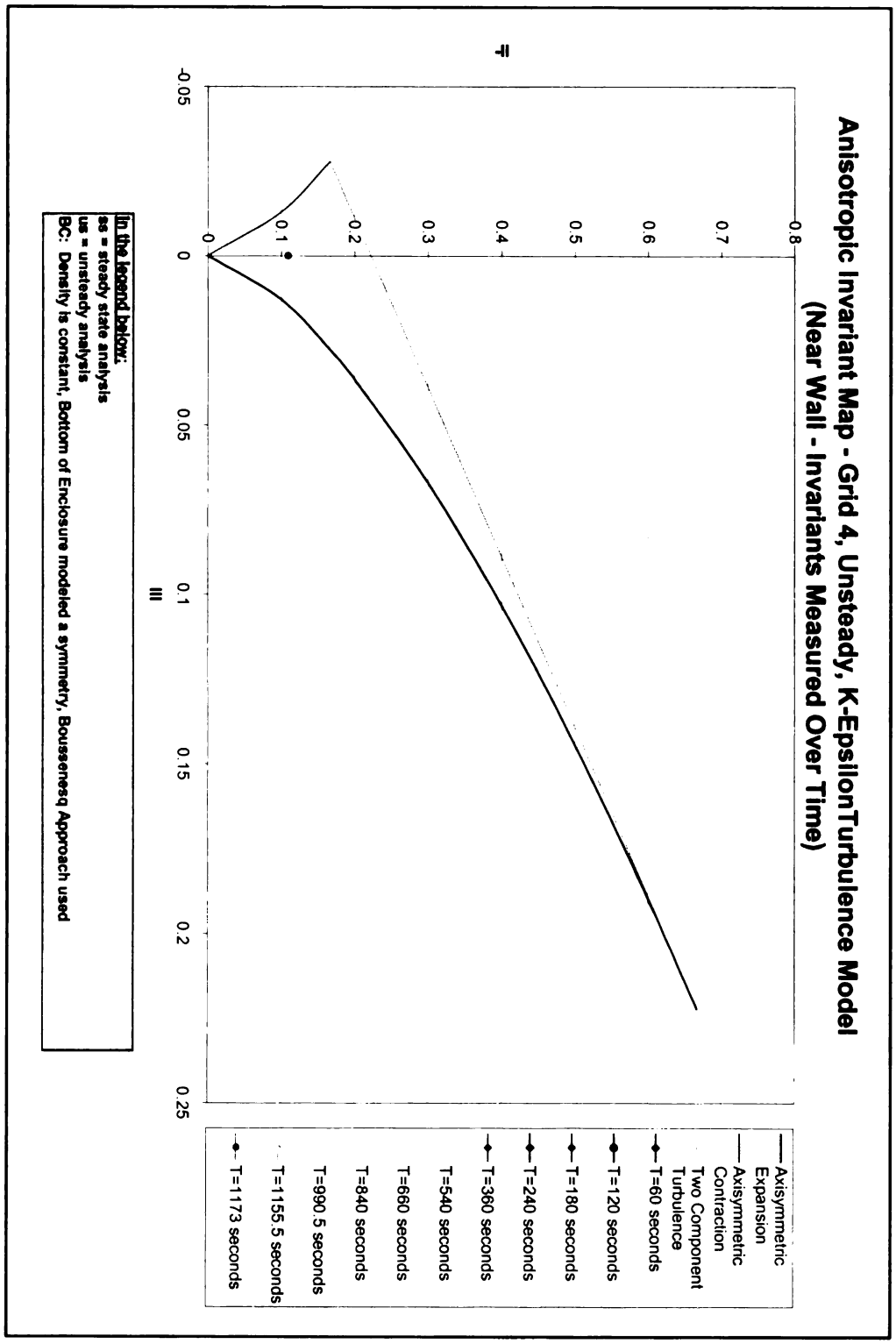

Figure 4.15: Plot of the Anisotropic Invariant Map generated from the transient calculation of the K-Epsilon Model for Grid Type 4 (Anisotropy Value Near Wall of Cylinder).

Figure 4.16 illustrates a plot of the Grid Refinement versus the turbulence Y+ values generated at the bottom wall of cylinder. The Y+ value measures the distance of the boundary layers in which laminar and turbulent flow develop. In this model it is shown that the Y+ value measured decreases with grid refinement of the model. This displays that out of the four models chosen for this study, the grid type 4 model was the best at predicting the nature of the boundaries in the near wall region of the bottom wall of the cylinder.

Figure 4.17 illustrates the Hot Soaking temperature profile of the bottom wall of the cylinder generated from the transient calculation of the K-Epsilon Model for Grid Type 4. As mentioned previously the objective of this thesis is to simulate the hot soaking phenomenon through CFD with a cylinder above a heated plate. This graph shows the temperature data measured on the bottom of the hollow cylinder over time. The temperature of the bottom wall of the cylinder reaches a peak at 300 seconds. The temperature of the bottom wall of the cylinder then decreases reaching steady state. This temperature behavior clearly displays the hot soaking phenomenon described in Chapter I.

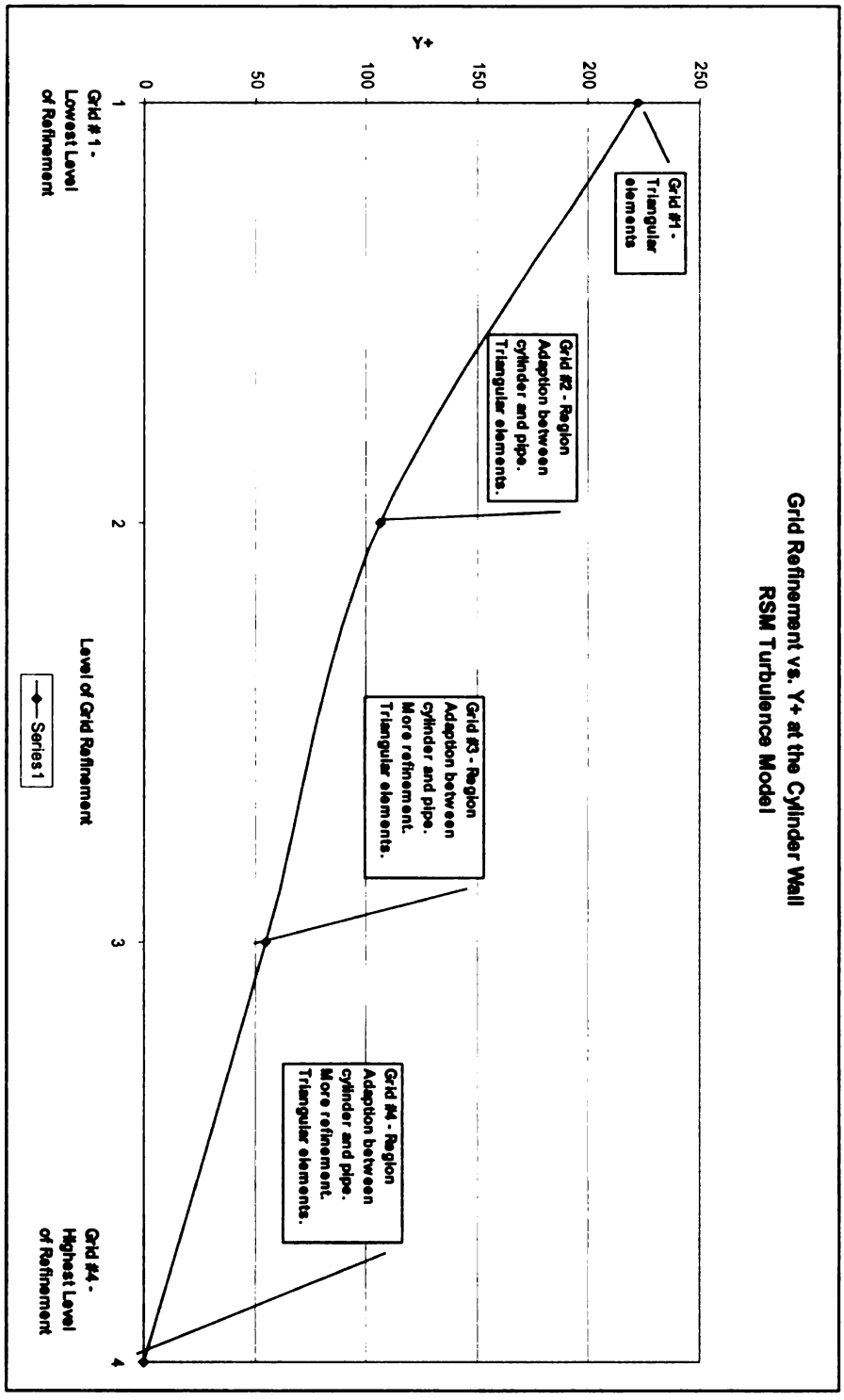

Figure 4.16: Plot of the Grid Refinement versus the Turbulence Y+ values generated at the bottom cylinder wall.

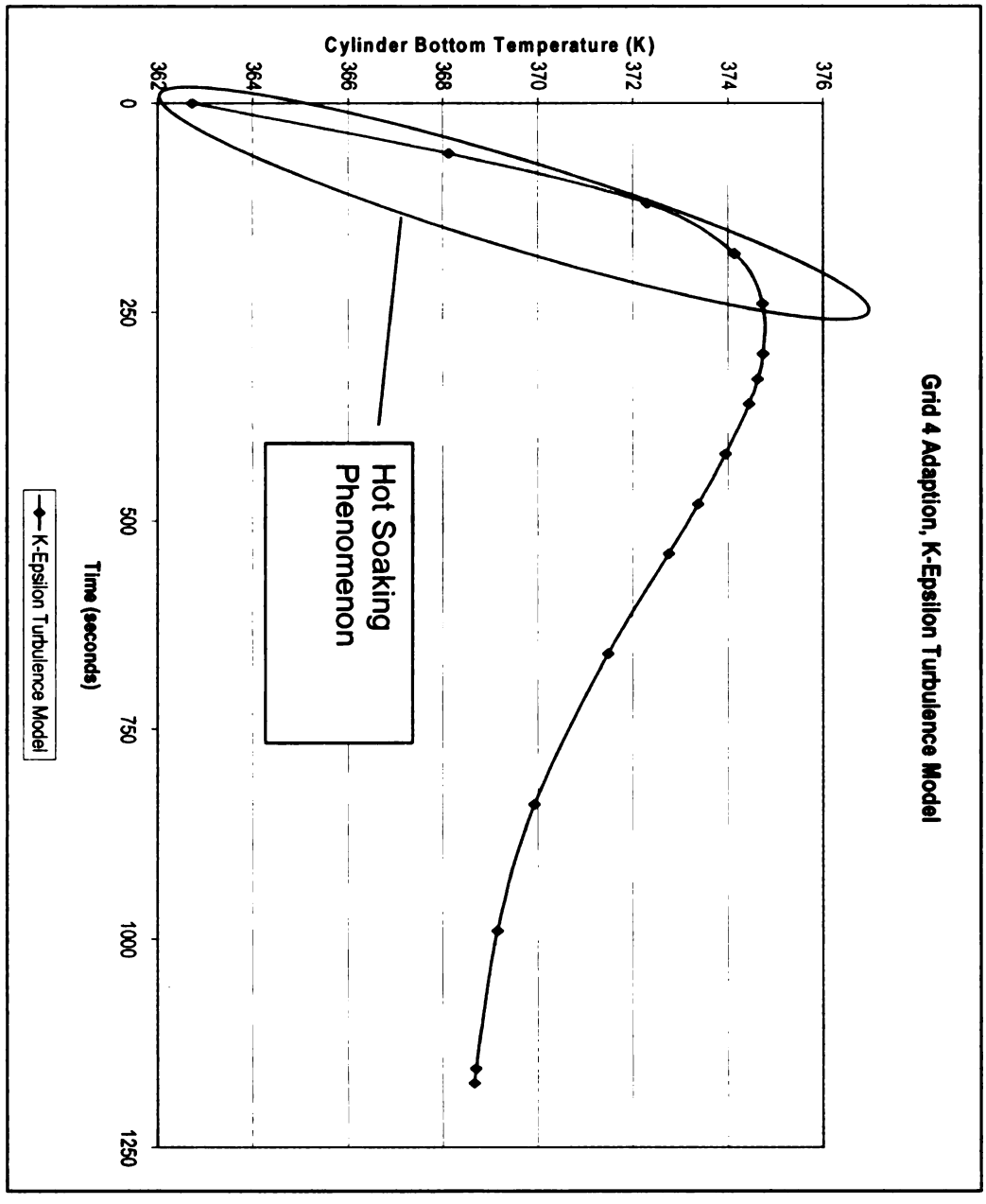

Figure 4.17: Plot of the Hot Soaking temperature profile of the bottom wall of the cylinder generated from the transient calculation of the K-Epsilon Model for Grid Type 4.

Figure 4.18 illustrates the temperature profiles of the bottom wall of the cylinder generated from the transient calculation of the K-Omega and Reynolds Stress Turbulence Models for Grid Type 4. As shown by the temperature profiles, these models did not accurately simulate the hot soaking process. These temperature profiles do not display an abrupt increase in temperature on the bottom wall of the cylinder. It is also important to determine the dominant mode of heat transfer that produces the high temperature on the bottom wall of the cylinder.

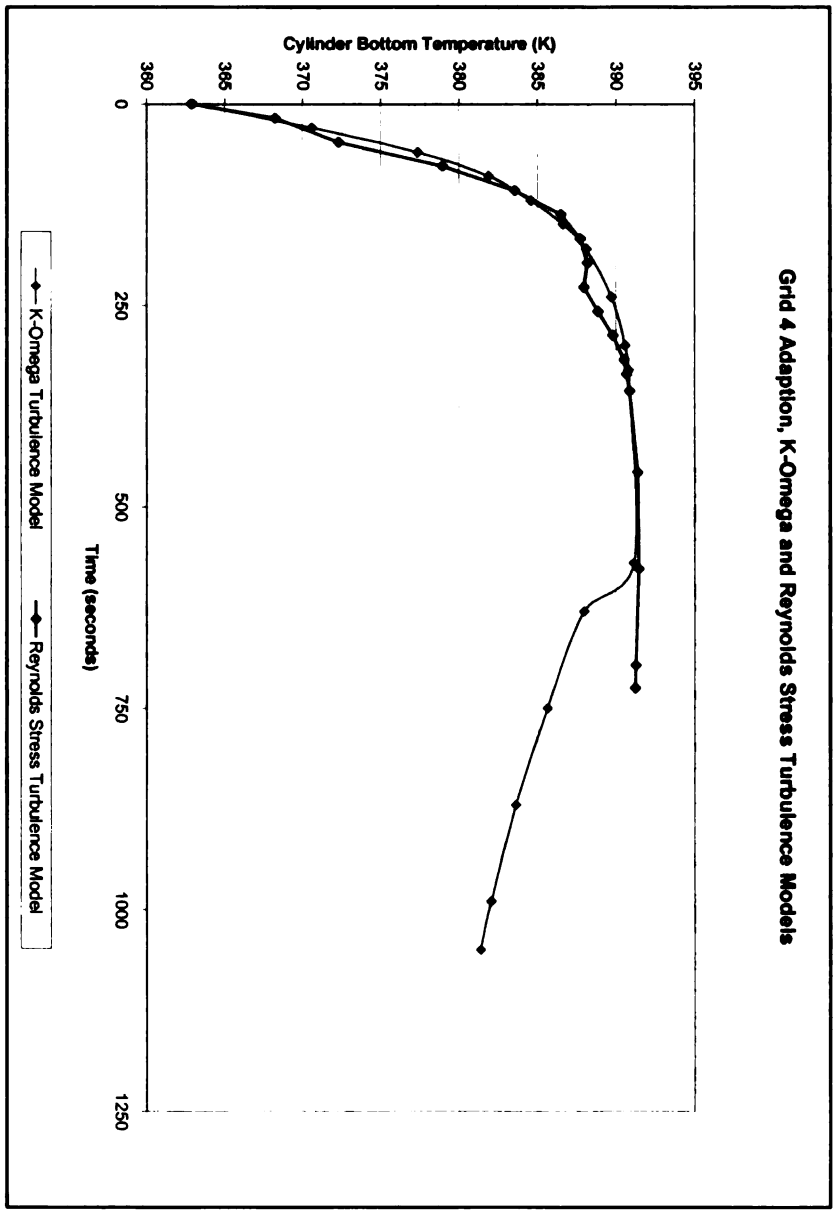

Figure 4.18: Plot of the temperature profiles of the bottom wall of the cylinder generated from the transient calculation of the K-Omega and Reynolds Stress Turbulence Models for Grid Type 4.

Figure 4.19 illustrates the dominant mode of heat transfer generated as a result of the hot soaking phenomenon on the top wall of the plate. This graph shows that that natural convection is the dominant mode of heat transfer produced by the hot plate during the initial phase of the hot soaking process. It also shows that the natural convection reaches equilibrium along with the other modes of heat transfer after 400 seconds. Natural convection is the highest contributor of temperature generation on the bottom wall of the cylinder.

Figure 4.20 illustrates the modes of heat transfer generated as a result of the hot soaking phenomenon on the bottom wall of the cylinder. It is shown that radiation is the second highest mode of heat transfer during the initial phase of the hot soaking process.

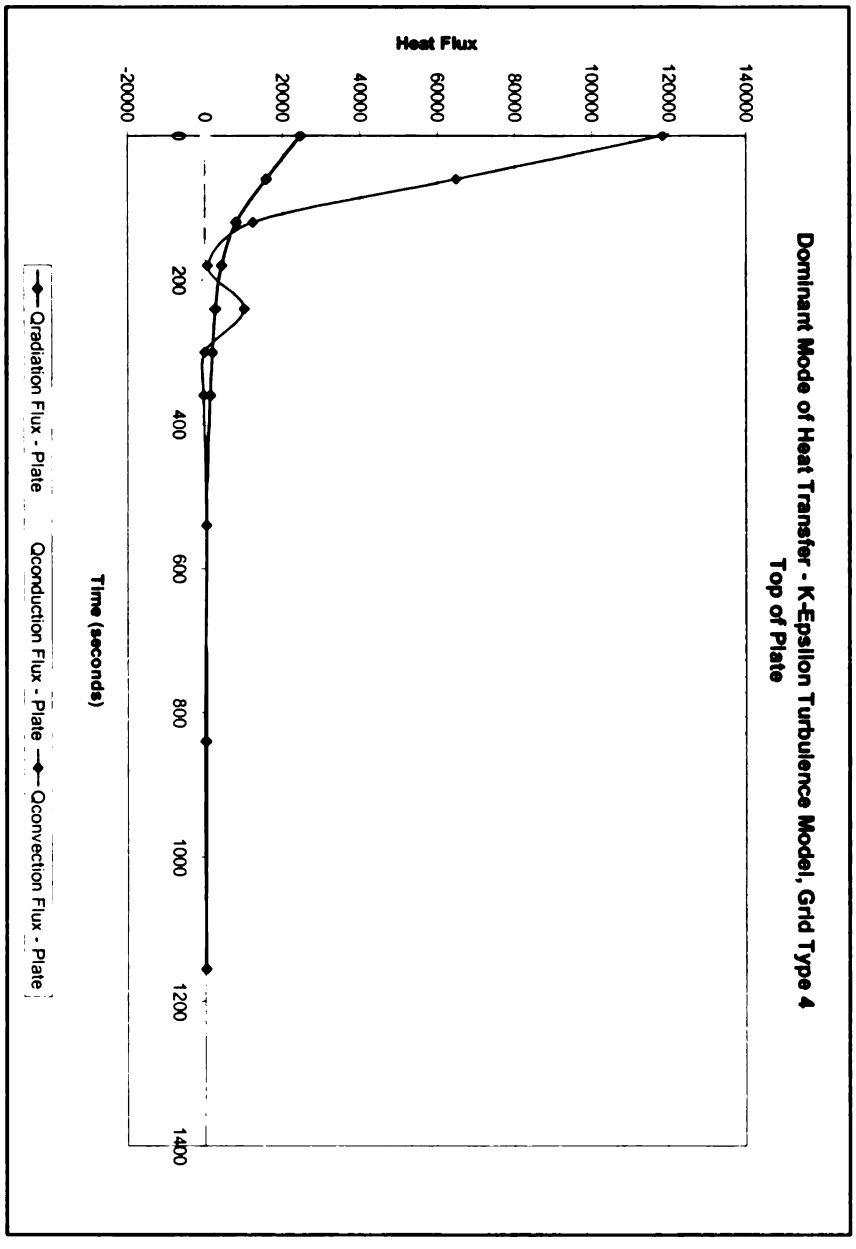

Figure 4.19: Plot of the dominant mode of heat transfer generated as a result of the hot soaking phenomenon on the top wall of the plate for K-Epsilon Model.

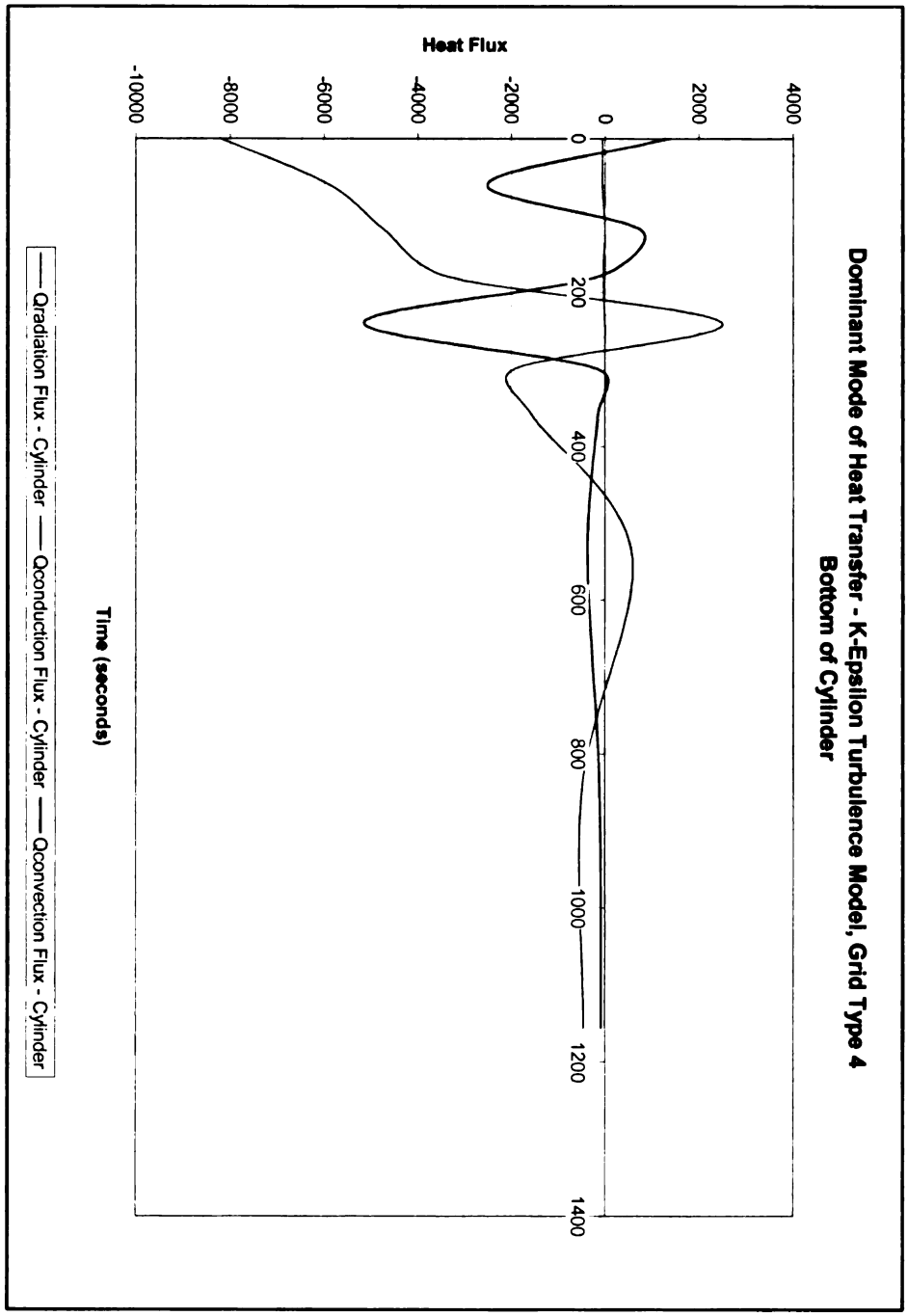

Figure 4.20: Plot of the modes of heat transfer generated as a result of the hot soaking phenomenon on the bottom wall of the cylinder for K-Epsilon Model.

Case II: Turbulence Model Study

Figure 4.21 illustrates the Anisotropic Invariant Map generated from the use of different turbulence models for Grid Type 4 measured at steady state. The anisotropy value was measured near the bottom wall of the cylinder. It is shown in this graph that the Reynolds Stress model, K-Epsilon and K-omega turbulence models generate physically realizable turbulence near the bottom wall of the cylinder.

Figure 4.22 illustrates the Anisotropic Invariant Map generated from the K-Epsilon turbulence models for Grid Type 4 measured near the bottom wall of the cylinder during the transient state. This graph shows that the K-Epsilon turbulence model produces physically realizable turbulence when measured over time. The turbulence generated is centered between the axisymmetric contraction, axisymmetric expansion, and isotropic two-component turbulence. Figure 4.23 illustrates the Anisotropic Invariant Map generated from the K-Omega turbulence models for Grid Type 4 measured near the bottom wall of the cylinder during the transient state. It is shown in this graph that the K-omega turbulence model generates physically realizable turbulence that range from axisymmetric contraction to axisymmetric expansion over time. Figure 4.24 illustrates the Anisotropic Invariant Map generated from the Reynolds Stress turbulence models for Grid Type 4 measured near the bottom wall of the cylinder during the transient state. This graph shows that the Reynolds Stress turbulence model produces unrealizable turbulence near

the bottom wall of the cylinder. The anisotropy becomes more unrealizable as the length of time increases. Overall, the K-Epsilon turbulence model produces a constant state of realizable turbulence when compared to the varying realizable turbulence of the K-Omega model and the unrealizable turbulence of the Reynolds Stress Model.

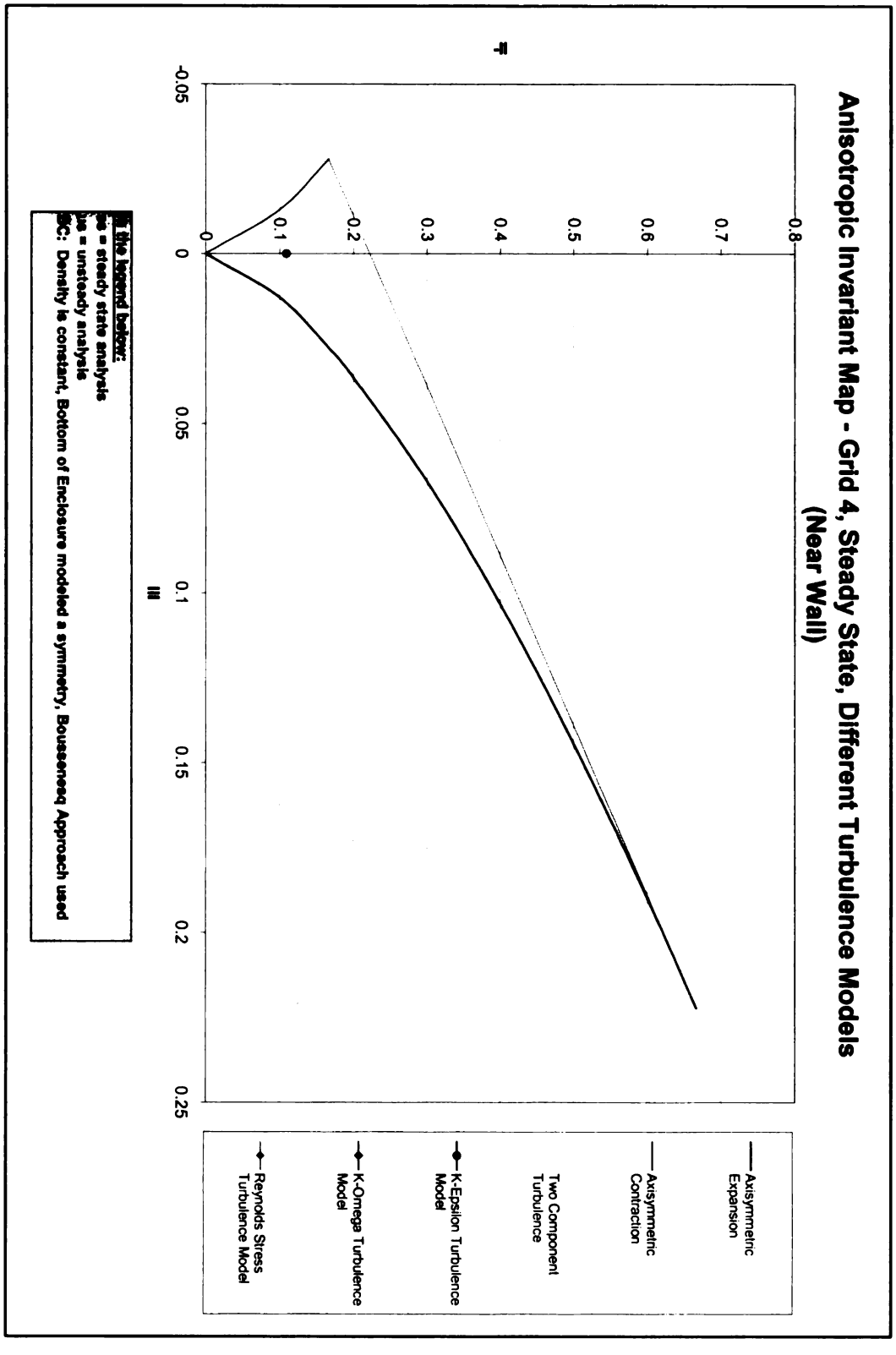

Figure 4.21: Plot of the Anisotropic Invariant Map generated from the use of different turbulence models for Grid Type 4, steady state (Anisotropy Value Near Wall of Cylinder).

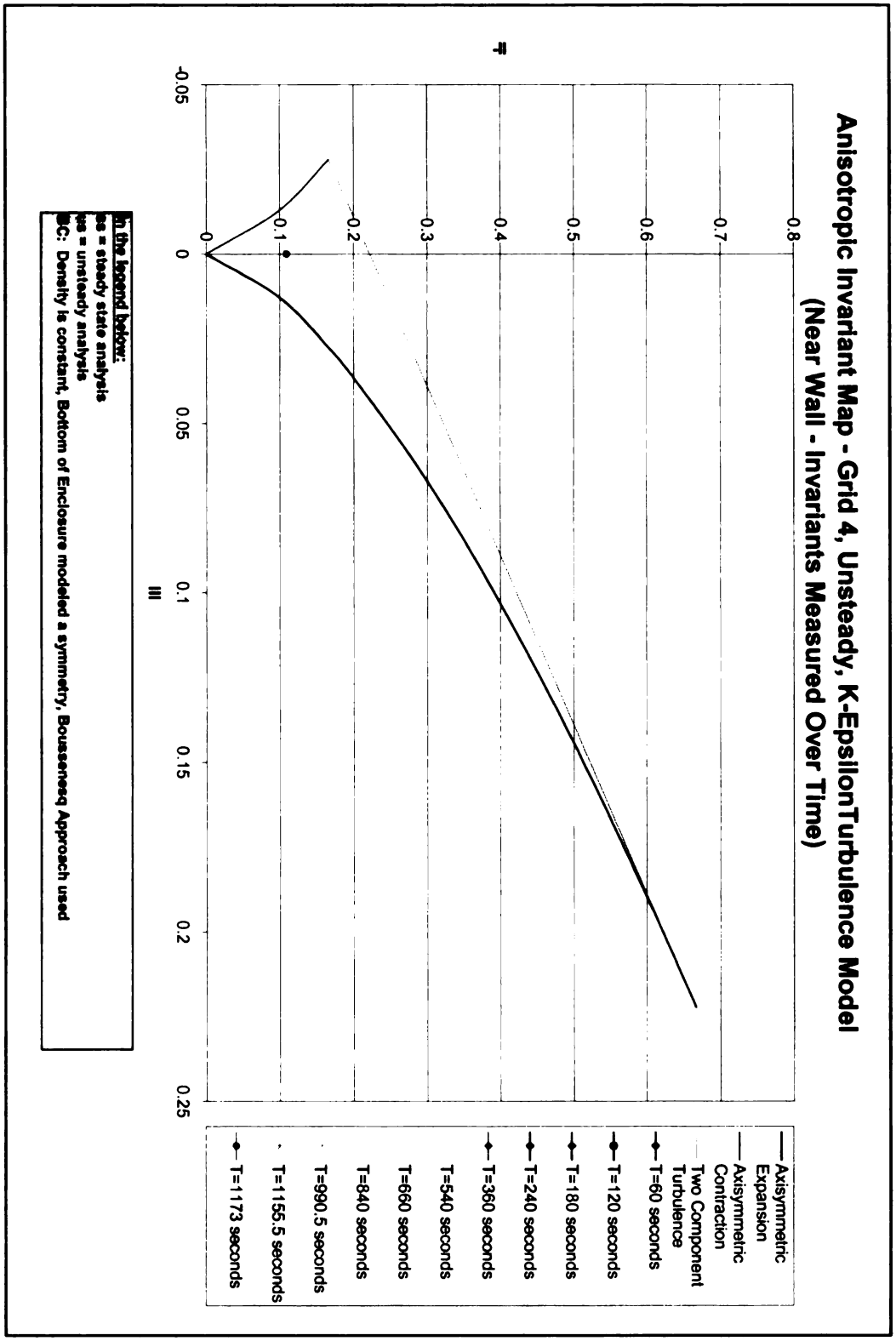

Figure 4.22: Plot of the Anisotropic Invariant Map generated from the K-Epsilon turbulence models for Grid Type 4, unsteady (Anisotropy Value Near Wall of Cylinder).

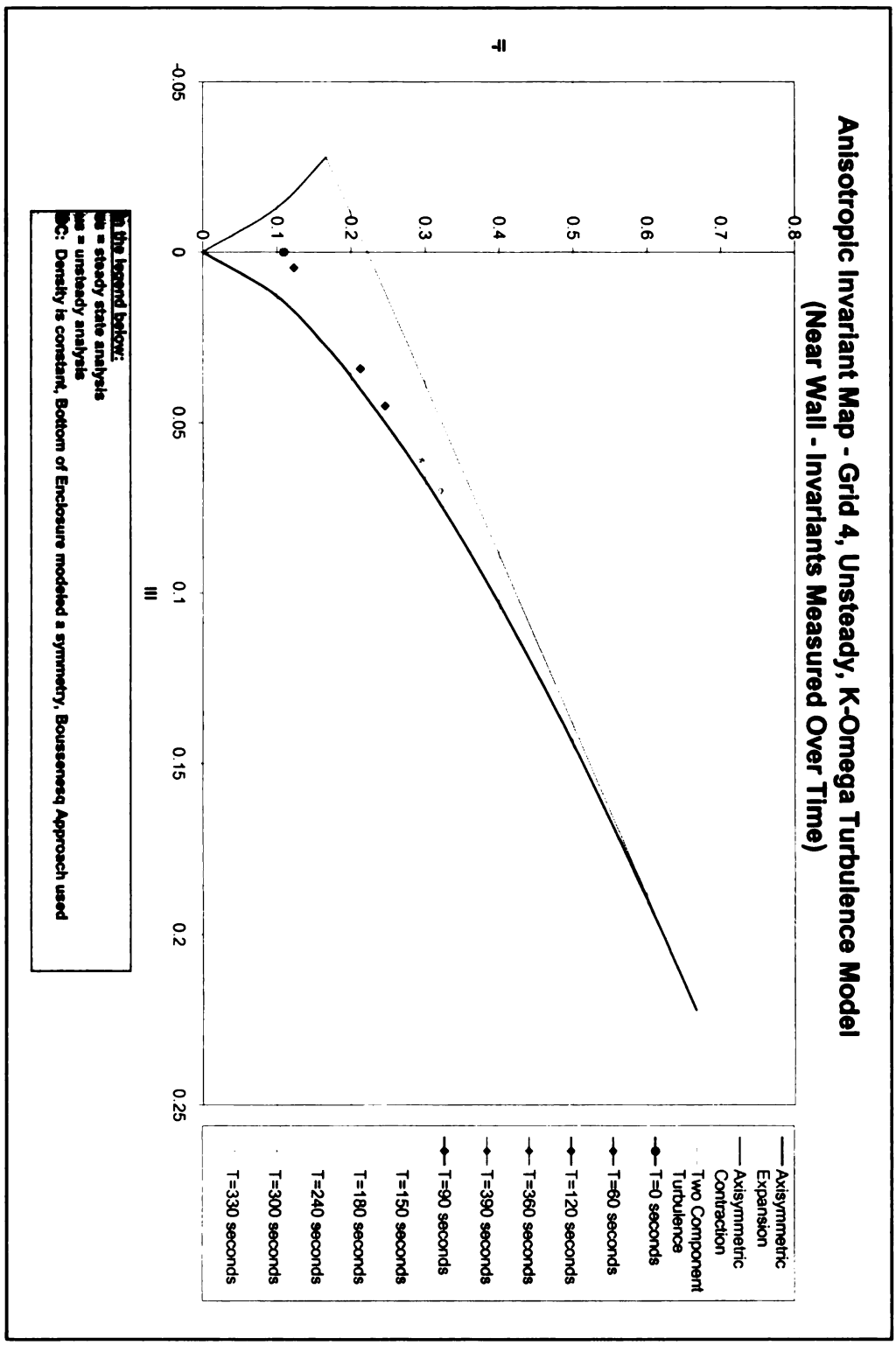

Figure 4.23: Plot of the Anisotropic Invariant Map generated from the K-Omega turbulence models for Grid Type 4, unsteady (Anisotropy Value Near Wall of Cylinder).

Figure 4.24: Plot of the Anisotropic Invariant Map generated from the Reynolds Stress turbulence models for Grid Type 4, unsteady (Anisotropy Value Near Wall of Cylinder).

Figure 4.25 illustrates the surface pressure distribution generated on the bottom wall of the cylinder. This graph shows a plot of the theoretical description of the surface pressure distribution for boundary layer flow generated around a circular cylinder. The surface pressure distribution was predicted using the grid type 4 K-Epsilon turbulent model. The model predicts the boundary layer similar to he theoretical data from *theta* = 30 to *theta* = to 150. The value of *theta* > 150 shows that the there is boundary layer separation due to turbulence toward the rear of the cylinder.

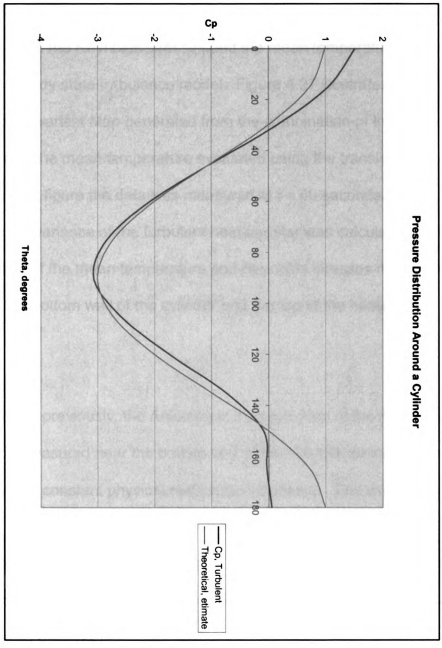

Figure 4.25: Plot of the surface pressure distribution generated on the bottom wall of the cylinder.

Figure 4.26 illustrates the Anisotropic Invariant Map generated from the combination of the Reynolds stresses and the mean temperature evaluated using the steady state turbulence model. Figure 4.27 illustrates the Anisotropic Invariant Map generated from the combination of the Reynolds stresses and the mean temperature evaluated using the transient turbulence model. In this figure the data was measured at t = 60 seconds. The anisotropic invariance of the turbulent heat transfer was calculated using a combination of the mean temperature and Reynolds stresses measured between the bottom wall of the cylinder and the top of the heated plate (see Figure 4.6).

As mentioned previously, the Anisotropic Invariant Map of the K-Epsilon turbulence measured near the bottom wall of the cylinder during the transient state shows a constant physical realizable turbulence. The evaluation of the turbulent heat transfer anisotropy at steady state displays physically realizable turbulent flow. The turbulence generated represents axisymmetric contraction. The evaluation of the turbulent heat transfer anisotropy at t = 60 seconds also displays physically realizable turbulent flow. The turbulence generated in this model ranges from axisymmetric contraction turbulence to axisymmetric expansion turbulence.

Figure 4.26: Plot of the Anisotropic Invariant Map generated from the combination of the Reynolds stresses and the mean temperature evaluated using the steady state K-Epsilon turbulence models for Grid Type 4.

Figure 4.27: Plot of the Anisotropic Invariant Map generated from the combination of the Reynolds stresses and the mean temperature evaluated using the unsteady K-Epsilon turbulence models for Grid Type 4 at T = 60 seconds.

V. CONCLUSIONS AND RECOMMENDATIONS

The focus of this thesis is to investigate the hot soaking phenomenon by quantifying the effect of the temperature generated on a hollow cylindrical component above a heated hollow horizontal plate. This investigation will be used to create a simple numerical simulation of the hot soaking process to aid in further study of the thermal characteristics of vehicle components contained within the underhood and underbody of a vehicle. The numerical simulations were performed using the CFD Software Fluent.

V.a. Conclusions

Single Phase Fluid Flow through a Pipe with a 90 Degree Bend

The Reynolds Stress turbulence model and the realizable K-Epsilon turbulence model produce both physically realizable and unrealizable turbulence. The physically realizable turbulence produced by the Reynolds Stress turbulence model displays turbulent flow that ranges from Two-component turbulence to axisymetric-expansion to isotropic turbulence; however the realizable K-Epsilon turbulence model displays isotropic turbulent flow. The graph of the velocity profiles generated for fully developed flow shows that the turbulent flow generated with the Reynolds number value of 95,000 produces a velocity profile closest to the theoretical value for both turbulence models.

Natural Convection in a 2D Square Enclosure

The realizable K-Epsilon model produces a numerical prediction of the natural convection process similar to the prediction of laminar flow published in the Fluent 6.1 Tutorial Guide. The use of the realizable K-Epsilon model with the boussinesq approach provided an accurate simulation of the buoyancy effects from natural convection. Figures 3-3 and 3-6 show the model's ability to simulate the rising plume of the lighter hot air and the falling plume of the heavier cold air created by the changes in temperature and density of the model. The comparison of the dimensionless height of the enclosure versus the dimensionless fluid temperature at mid width in Figure 3-7 to the theoretical data in Figure 3-8 further displays the model's ability to simulate natural convection.

Two Dimensional Model of a Cylinder above a Heated Plate

The Grid Type 4 refinement level produces the best prediction of realizable turbulent flow. The K-Epsilon turbulence model produces physically realizable turbulence when measured over time. The turbulence generated is centered between the axis-symmetric contraction, axis-symmetric expansion, and isotropic twp-component turbulence. Overall, the K-Epsilon turbulence model produces a constant state of realizable turbulence when compared to the varying realizable turbulence of the K-Omega model and the unrealizable turbulence of the Reynolds Stress Model.

The K-Epsilon model temperature profile shows an accurate simulation of the hot soaking phenomenon. It displays an abrupt increase in temperature on the bottom wall of the hollow cylinder. The temperature spike created on the bottom wall of the cylinder was generated from natural convection from the top of the heated plate. The surface pressure distribution measured around the hollow cylinder agrees with theoretical data and shows evidence of a turbulent boundary layer near the rear of the cylinder. The evaluation of the turbulent heat transfer anisotropy at steady state calculation and the transient calculation of t = 60 seconds displays physically realizable turbulent flow. The steady state calculation of anisotropy produces axisymmetric contraction turbulence. The unsteady calculation produces turbulence that ranges from axisymmetric contraction turbulence to axisymmetric expansion turbulence.

In conclusion, the study of the model of a hollow cylinder above a heat plate successfully produced a numerical simulation of the hot soaking phenomenon. Through the preliminary studies of the previous two cases of Single Phase Fluid Flow through a Pipe with a 90 Degree Bend and Natural Convection in a 2D Square Enclosure, the understanding of the use of CFD to numerically predict turbulent flow and heat transfer was achieved. This gained knowledge of the use of CFD to numerically simulate turbulence and heat transfer aided in the creation of the numerical simulation of the hot soaking process as well as the determination of the dominant mode of heat

transfer during this process. This model can now be used for studies of vehicle component that are exposed to extreme temperature conditions in environments without forced convection. Some recommendations are listed below regarding the development of a more robust simulation of the hot soaking process.

V.b. Recommendations

Based on the trend of the increased accuracy of turbulent flow predictions through grid refinement, it is recommended that the grids modeled during a hot soaking simulation require a high level of refinement. Although the realizable K-Epsilon model accurately simulated the hot soaking process, a highly refined grid model will allow the use of a variety turbulence models to simulate hot soaking for different testing conditions. An extensive study is required to evaluate the predictability of the turbulent heat flux through anisotropy and invariance. This study should carefully analyze of the use of different turbulence models as well as the different modes of heat transfer.

APPENDIX

APPENDIX A

SINGLE PHASE FLOW THROUGH A PIPE WITH 90 DEGREE BEND

Table A-1: List of the anisotropic values calculated to generate the Anisotropic Invariant Map generated for single phase fluid flow through a pipe using the K-Epsilon Turbulence Model at Re No. = 1000.

Pipe Flow Anisotropy Calculations		Radius = 0.80 (Center of Pipe)	Radius = 0.83	Radius = 0.86	Radius = 0.89	Radius = 0.92	Radius = 0.95 (Pipe Wall)
Near Wall of Cylinder	UU	0.0044419	0.005632	0.006524	0.007692	0.004979	0.004008838
	VV	0.0048533	0.004562	0.005174	0.005491	0.004309	0.004029562
	WW	0.0034057	0.003129	0.003781	0.003756	0.003781	0.003983238
	UV	0.0011337	0.001608	0.002032	0.001947	0.001607	0.000793417
	b11	0.0368254	0.106633	0.119728	0.166135	0.061799	0.000736508
	b22	0.0711111	0.023104	0.025941	0.023246	0.008647	0.002463492
	b33	-0.0495238	-0.08886	-0.07075	-0.08941	-0.03326	-0.00139683
	b12	0.0944762	0.125657	0.141088	0.12643	0.127528	0.066118095
	-II	0.0087597	0.021222	0.021805	0.020116	0.016835	0.004371739
	III	0.0003123	0.001184	0.001189	0.001084	0.000523	6.10383E-06

Table A-2: List of the anisotropic values calculated to generate the Anisotropic Invariant Map for single phase fluid flow through a pipe using the K-Epsilon Turbulence Model at Re No. = 9500.

Pipe Flow Anisotropy Calculations		Radius = 0.80 (Center of Pipe)	Radius = 0.83	Radius = 0.86	Radius = 0.89	Radius = 0.92	Radius = 0.95 (Pipe Wall)
Near Wall of Cylinder	UU	0.0001028	8.86E-05	6.4E-05	5.52E-05	4.22E-05	0.000012
	VV	0.0001281	9.49E-05	5.5E-05	4.5E-05	4.19E-05	0.000012
	WW	9.445E-05	5.83E-05	4.55E-05	4.12E-05	4.19E-05	0.000012
	UV	-4.163E-05	-3.2E-05	-9.8E-07	5.68E-06	6.2E-07	0
	b11	0.0093605	0.069412	0.076749	0.060952	0.0019	0
	b22	0.0936054	0.09786	0.019536	-0.01181	-0.00078	0
	b33	-0.0185034	-0.06827	-0.04186	-0.03886	-0.00052	0
	b12	-0.1387755	-0.14508	-0.00628	0.040571	0.004924	0
	-II	0.0187248	0.018918	0.000293	0.003876	2.6E-05	0
	III	0.0003401	0.000973	-6.1E-05	9.19E-05	1.33E-08	0

Table A-3: List of the anisotropic values calculated to generate the Anisotropic Invariant Map generated for single phase fluid flow through a pipe using the K-Epsilon Turbulence Model at Re No. = 95,000.

Pipe Flow Anisotropy Calculations		Radius = 0.80 (Center of Pipe)	Radius = 0.83	Radius = 0.86	Radius = 0.89	Radius = 0.92	Radius = 0.95 (Pipe Wall)
Near Wall of Cylinder	UU	0.024	0.027	0.032	0.039	0.044	0.039
	VV	0.009	0.01	0.012	0.016	0.027	0.061
	WW	0.002	0.002	0.003	0.006	0.012	0.027
	UV	0.012	0.012	0.015	0.019	0.025	0.037
	b11	-0.2380952	0.280303	0.333333	0.33908	0.261261	0.072916667
	b22	-0.297619	-0.106061	-0.083333	-0.057471	0.031532	0.302083333
	b33	-0.3253968	-0.287879	-0.270833	-0.229885	-0.171171	-0.05208333
	b12	0.047619	0.272727	0.3125	0.327586	0.337838	0.385416667
	-II	0.037289	0.186983	0.198785	0.179647	0.135196	0.129231771
	III	-0.0223203	0.029971	0.033972	0.029149	0.018126	0.006589536

Table A-4: List of the anisotropic values calculated to generate the Anisotropic Invariant Map for single phase fluid flow through a pipe using the K-Epsilon Turbulence Model at Re No. 1000.

Pipe Flow Anisotropy Calculations		Radius = 0.80 (Center of Pipe)	Radius = 0.83	Radius = 0.86	Radius = 0.89	Radius = 0.92	Radius = 0.95 (Pipe Wall)
Near Wall of Cylinder	UU	0.000001	0.000003	0.000008	0.000018	0.000024	0.000013
	VV	4.32E-09	4.32E-09	0.000001	0.000007	0.000025	0.000035
	WW	5.11E-09	5.11E-09	0.000001	0.000004	0.000013	0.000015
	UV	-0.0000016	-1.6E-06	0.000001	0.000007	0.000017	0.000013
	b11	0.1666667	0.416667	0.466667	0.309524	0.053763	-0.13636364
	b22	-0.3311733	-0.33225	-0.23333	-0.08333	0.069892	0.196969697
	b33	-0.3307783	-0.33206	-0.23333	-0.19048	-0.12366	-0.10606061
	b12	-0.8	-0.4	0.1	0.25	0.274194	0.196969697
	-II	0.8046099	0.4087	0.173333	0.124575	0.086715	0.076905418
	III	0.2299556	0.099098	0.027741	0.016818	0.008832	0.006963575

Table A-5: List of the anisotropic values calculated to generate the Anisotropic Invariant Map for single phase fluid flow through a pipe using the Reynolds Stress Turbulence Model at Re No. = 9500.

Pipe Flow Anisotropy Calculations		Radius = 0.80 (Center of Pipe)	Radius = 0.83	Radius = 0.86	Radius = 0.89	Radius = 0.92	Radius = 0.95 (Pipe Wall)
Near Wall of Cylinder	UU	0.002	0.003	0.004	0.005	0.004	0.002
	VV	0.0004	0.0006	0.0009	0.001	0.002	0.004
	WW	0.0005	0.0006	0.0009	0.001	0.0016	0.002
	UV	0.000056	0.0003	0.0006	0.001	0.001	0.001
	b11	0.3809524	0.380952	0.333333	0.291667	0.166667	0
	b22	-0.1904762	-0.19048	-0.18333	-0.20833	-0.08333	0.333333333
	b33	-0.1547619	-0.19048	-0.18333	-0.20833	-0.13333	0
	b12	0.02	0.071429	0.1	0.125	0.125	0.166666667
	-II	0.0969136	0.113946	0.104722	0.119792	0.047292	0.027777778
	III	0.0112918	0.014793	0.013037	0.015914	0.003935	0

Table A-6: List of the anisotropic values calculated to generate the Anisotropic Invariant Map for single phase fluid flow through a pipe using the K-Epsilon Turbulence Model at Re No. 95,000.

Pipe Flow Anisotropy Calculations		Radius = 0.80 (Center of Pipe)	Radius = 0.83	Radius = 0.86	Radius = 0.89	Radius = 0.92	Radius = 0.95 (Pipe Wall)
Near Wall of Cylinder	UU	0.02008	0.018238	0.02232	23.33813	0.043284	0.084392272
	VV	0.0182438	0.018279	0.016217	23.33135	0.034686	0.083326476
	WW	0.0176952	0.017147	0.01704	23.33227	0.0356	0.084070313
	UV	0.0054743	0.006256	0.007038	0.00782	0.012441	0.041935184
	b11	0.0385185	0.004402	0.08	6.86E-05	0.060161	0.001556635
	b22	0.004515	0.00516	-0.033016	-2.83E-05	-0.018009	-0.00267271
	b33	-0.0056437	-0.015802	-0.017778	-1.52E-05	-0.009697	0.00027902
	b12	0.1013757	0.115858	0.13034	0.000112	0.113098	0.166409459
	-II	0.010135	0.01365	0.019946	1.47E-08	0.013969	0.027696346
	III	5.702E-05	0.000212	0.000349	2.2E-13	0.000135	-7.7278E-06

Table A-7: List of the dimensionless values of radius and velocity used to create the plot of the Velocity Profile of Fully Developed Flow for single phase fluid flow through a pipe using the K-Epsilon and Reynolds Stress Turbulence Model at different Reynolds numbers.

Dimen-sionless Parameter	Turbulence Model	Reynolds Number	R = 0.80 (Center of Pipe)	R = 0.83	R = 0.86	R = 0.89	R = 0.92	R = 0.95 (Pipe Wall)
U/Uo	K-Epsilon	95,000	1	1.000	0.986	0.973	0.973	0.017
U/Uo	K-Epsilon	9500	1	1.188	1.417	1.542	1.500	0.016
U/Uo	K-Epsilon	1000	1	1.068	1.096	1.112	1.082	0.014
U/Uo	RSM	95,000	1	1.000	1.000	0.986	0.969	0.016
U/Uo	RSM	9500	1	1.000	1.000	0.971	0.369	0.078
U/Uo	RSM	1000	1	1.083	1.150	1.150	1.033	0.012
U/Uo	Analytical Value	95,000	1	0.970	0.932	0.881	0.801	0.000
U/Uo	Analytical Value	9500	1	0.941	0.871	0.781	0.647	0.000
U/Uo	Analytical Value	1000	1	0.960	0.911	0.846	0.745	0.000
r/R	N/A	N/A	0	0.2	0.4	0.6	0.8	1

APPENDICES B

NATURAL CONVECTION IN A 2D SQUARE ENCLOSURE

Table B-1: List of the dimensionless parameters used to create the plot of dimensionless height (in the y-direction) versus dimensionless temperature generated inside the 2D Enclosure for the Realizable K-Epsilon turbulence model without radiation.

Dimensionless Temeprature	Dimensionless Height (Y/H)
0.17	0
0.181818182	0.1
0.222222222	0.2
0.313131313	0.3
0.404040404	0.4
0.494949495	0.5
0.595959596	0.6
0.686868687	0.7
0.777777778	0.8
0.818181818	0.9
0.82	1

APPENDICES C

TWO-DIMENSIONAL MODEL OF CYLINDER ABOVE A HEATED PLATE

Table C-1: List of the temperature profile specified for the inner surface of the heated plate.

Time (seconds)	Temperature (K)
0	911.15
10	883.15
20	856.15
30	835.15
40	815.15
50	791.15
60	769.15
70	750.15
80	730.15
90	713.15
100	697.15
110	682.15
120	668.15
130	654.15
140	642.15
150	631.15
160	620.15
170	610.15
180	601.15
190	593.15
200	586.15
210	579.15

Table C-2: List of the anisotropic values calculated to generate the Anisotropic Invariant Map of the steady state calculation of the Reynolds Stress Model for Grid Types 1 through 4.

Model Descriptions	Invariant Diagram Calculations	Grid #1 scaled - 1st order	Grid 2 scaled us with new temp profile, ground symm - 1st order	Grid 2 scaled ss - 1st order	Grid 3 scaled ss - 1st order	Grid 4 with Adaption - 1st & 2nd order	Grid 4 with Adaption - 2nd order
Near Wall	UU	0.51	0.0014	0.46	0.0015	0	0.68
of Cylinder	VV	0.135	0.0005	0.13	0.0015	0	0.0017
	WW	0.174	0.0021	0.26	0.063	0.000003	0.58
	UV	-0.079	0.0007	0.197	0.026	-0.307	0.042
	b11	0.525	-0.31	-0.07	-0.33	-0.33	0.049
	b22	-0.106	-0.32	-0.26	-0.33	-0.33	-0.33
	b33	-0.04	-0.3	-0.18	-0.004	-0.33	-0.007
	b12	-0.466	0.125	0.11	0.14	-0.295	0.024
	-II	**0.274**	**0.01**	**0.03**	**-0.09**	**0.087**	**0.017**
	III	**0.0109**	**-0.03**	**-0.0011**	**-0.000357**	**-0.0072**	**0.000117**
Maximum	UU	4.24	0.068	5.71	9.058	22.69	13.63
Value for	VV	6.7	0.049	6.32	6.18	15.47	10.54
Model	WW	4.32	0.068	5.14	6.15	16.82	11.59
	UV	2.16	0.0123	3.56	3.95	10.46	6.9
	b11	-0.048	-0.05	0.03	0.14	0.1	0.051
	b22	0.117	-0.13	0.07	-0.01	-0.037	-0.036
	b33	-0.043	-0.05	-0.005	-0.01	-0.011	-0.007
	b12	0.144	0.05	0.23	0.21	0.2	0.19
	-II	**0.028**	**-0.002**	**0.05**	**0.05**	**0.044**	**0.038**
	III	**0.0011**	**-0.0002**	**0.00025**	**0.000455**	**0.000481**	**0.000266**

Table C-3: List of the anisotropic values calculated to generate the Anisotropic Invariant Map of the transient calculation of the K-Epsilon Model for Grid Type 4 (Maximum Anisotropy Value of Mode and value measured near bottom cylinder wall).

Model Descriptions	Invariant Diagram Calculations	Grid 4 scaled us Kepsilon Turbulence Model @60 sec	Grid 4 scaled us Kepsilon Turbulence Model @120 sec	Grid 4 scaled us Kepsilon Turbulence Model @180 sec	Grid 4 scaled us Kepsilon Turbulence Model @240 sec	Grid 4 scaled us Kepsilon Turbulence Model @360 sec	Grid 4 scaled us Kepsilon Turbulence Model @540 sec
Near Wall of Cylinder	UU	0.00304625	1.3344E-06	1.19999E-08	1E-09	1.98E-10	2.53333E-11
	VV	0.002959785	1.33231E-06	1.20001E-08	9.99999E-10	1.98E-10	2.53333E-11
	WW	0	0	0	0	0	0
	UV	-3.4789E-05	-7.8954E-10	8.93388E-14	8.81633E-17	9.69796E-17	5.21633E-18
	b11	0.00513886	0.000266849	-2.9605E-06	3.33061E-07	-1.3853E-07	-8.1346E-08
	b22	-0.00446835	-0.00025584	3.25079E-06	-1.9592E-07	1.68213E-07	8.13462E-08
	b33	-0.33	-0.33	-0.33	-0.33	-0.33	-0.33
	b12	-0.0038654	-0.00019739	2.48163E-06	2.93878E-08	1.63265E-07	6.86359E-08
	-II	0.108937904	0.108900107	0.1089	0.1089	0.1089	0.1089
	III	1.25082E-05	3.53869E-08	5.20826E-12	2.18184E-14	1.64861E-14	3.73827E-15
Maximum Value for Model	UU	-96.8763265	-3.76114286	-0.02499864	-0.00326694	-0.00031753	-2.5321E-05
	VV	-1171.1185	-3.24914286	-0.0590449	-0.00833252	-0.00064406	-3.7838E-05
	WW	0	0	0	0	0	0
	UV	-1615.33388	-24.5314286	-0.20026122	-0.03458531	-0.00308571	-0.00020841
	b11	-4.2939354	-4.81088435	-3.30936184	-1.96680272	-7.14723658	-2.12152658
	b22	-48.2122582	-4.20136054	-7.36248785	-4.49959184	-14.1543313	-3.00549598
	b33	-0.33333333	-0.33333333	-0.33333333	-0.33333333	-0.33333333	-0.33333333
	b12	-66.0398151	-29.2040816	-23.840622	-17.2926531	-66.2170448	-14.7180906
	-II	4154.347968	832.7772354	544.1212304	290.2971515	4283.643773	210.3570632
	III	1384.745619	277.5553748	181.3367064	96.72868014	1427.844221	70.08198402

Table C-3 (cont'd): List of the anisotropic values calculated to generate the Anisotropic Invariant Map of the transient calculation of the K-Epsilon Model for Grid Type 4 (Maximum Anisotropy Value of Mode and value measured near bottom cylinder wall).

Model Descriptions	Invariant Diagram Calculations	Grid 4 scaled us Kepsilon Turbulence Model @660 sec	Grid 4 scaled us Kepsilon Turbulence Model @840 sec	Grid 4 scaled us Kepsilon Turbulence Model @990.5 sec	Grid 4 scaled us Kepsilon Turbulence Model @1155.5 sec	Grid 4 scaled us Kepsilon Turbulence Model @1173 sec
Near Wall of Cylinder	UU	1E-11	3.46667E-12	2.04E-12	1.43333E-12	1.39333E-12
	VV	1E-11	3.46667E-12	2.04E-12	1.43333E-12	1.39333E-12
	WW	0	0	0	0	0
	UV	1.00286E-18	5.91673E-20	-8E-22	-5.551E-21	-6.7347E-21
	b11	-3.5657E-08	-5.6892E-09	5.22876E-10	2.58187E-09	2.14823E-09
	b22	3.56571E-08	6.63736E-09	-4.3573E-10	-1.7212E-09	-2.0623E-09
	b33	-0.33	-0.33	-0.33	-0.33	-0.33
	b12	3.34286E-08	5.68917E-09	-1.3072E-10	-1.2909E-09	-1.6112E-09
	-II	0.1089	0.1089	0.1089	0.1089	0.1089
	III	7.88337E-16	2.31421E-17	8.08236E-20	2.01648E-18	2.31863E-18
Maximum Value for Model	UU	-2.3823E-06	1.94612E-07	-5.3457E-06	1.85986E-07	1.9351E-07
	VV	-3.3619E-06	-7.8389E-07	-3.9986E-07	-3.1469E-07	-6.3197E-08
	WW	0	0	0	0	0
	UV	-3.2327E-05	-7.8525E-06	-2.2988E-06	-1.1265E-06	-1.0462E-06
	b11	-0.6238593	-0.28910328	-2.12719719	-0.24304868	-0.23609202
	b22	-0.74332172	-0.51149041	-0.46751587	-0.48609735	-0.36509076
	b33	-0.33333333	-0.33333333	-0.33333333	-0.33333333	-0.33333333
	b12	-3.94225983	-1.78465677	-0.77140118	-0.54685952	-0.52573069
	-II	15.18879552	3.148237349	-0.28832755	0.292021129	0.301308857
	III	5.025894802	1.012375413	-0.13314622	0.060303339	0.063399249

Table C-4: List of the Y+ values measured to create the plot of the Grid Refinement versus the Turbulence Y+ values generated at the bottom cylinder wall.

Grid Refinement Model	Y+ Value
Grid 1 ss rsm 1st order	222.5
Grid 2 ss rsm 1st order	106.31
Grid 3 ss rsm 1st order	54.77
Grid 3 ss rsm 1st order plus 2nd order	21.8
Grid 3 ss rsm 2nd order	33.34
Grid 3 ss rsm 1st order	51.96
Grid 4 ss rsm 1st order plus 2nd order	0
Grid 4 ss rsm 2nd order	0

Table C-5: List of the temperature values measured to create the Hot Soaking temperature profile of the bottom wall from the cylinder for the transient calculation of the K-Epsilon Model for Grid Type 4.

Time (seconds)	Cylinder Bottom Temperature (K)
0	362.73
60	368.13
120	372.3
180	374.14
240	374.73
300	374.74
330.5	374.62
360	374.44
420	373.95
480	373.37
540	372.75
660	371.48
840	369.93
990.5	369.15
1155.5	368.69
1173	368.66

Table C-6: List of the temperature values calculated to create the temperature profiles of the bottom wall of the cylinder from the transient calculation of the K-Omega Turbulence Model for Grid Type 4.

Time (seconds)	Cylinder Bottom Temperature (K)
0	362.98
30	370.61
60	377.37
90	381.9
120	384.6
150	386.63
180	388.11
240	389.69
300	390.6
330	390.8
570	391.12
630	387.96
750	385.6
870	383.6
990	382.03
1050	381.36

Table C-7: List of the temperature values calculated to create the temperature profiles of the bottom wall of the cylinder from the transient calculation of the RSM Turbulence Model for Grid Type 4.

Time (seconds)	Cylinder Bottom Temperature (K)
0	362.89
18	368.26
47.5	372.32
77.5	378.95
107.5	383.54
137.5	386.5
167.5	387.7
197.5	388.17
227.5	387.94
257.5	388.83
287.5	389.78
317.5	390.5
335.5	390.67
356.5	390.86
457	391.37
577	391.45
697	391.27
725	391.22

Table C-8: List of the heat flux values calculated to generate the plot of the dominant mode of heat transfer generated as a result of the hot soaking phenomenon on the top wall of the plate for K-Epsilon Model.

Time (seconds)	Qradiation flux	Qconduction flux	Qconvection flux
0	24565.8	55.176	118468.524
60	15920	-410.4925	64881.4925
120	8053	-362.0925	12405.0925
180	4257	-241.0925	786.0925
240	2651	-156.3925	10153.3925
300	1853	-126.1425	-156.8575
360	1331	-95.8925	-312.1075
540	196	-53.5425	427.5425
840	250	-114.0425	19.0425
1155.5	275	-313.6925	342.6925

Table C-9: List of the heat flux values calculated to generate the plot of the modes of heat transfer generated as a result of the hot soaking phenomenon on the bottom wall of the cylinder for K-Epsilon Model.

Time (seconds)	Qradiation flux	Qconduction flux	Qconvection flux
0	-8206	-48.2185	1366.2185
60	-5905	-50.82	-2513.18
120	-4694	0	782
180	-3356	-39.325	-167.675
240	2492	-0.0605	-5151.9395
300	-1938	0	-142
360	-1556	0	-155
540	570	0	-374
840	-477	0	-123
1155.5	-451	0	-90

Table C-10: List of the anisotropic values calculated to generate the Anisotropic Invariant Map from the use of different turbulence models for Grid Type 4, steady state (Anisotropy Value Near Wall of Cylinder).

Model Descriptions	Invariant Diagram Calculations	Grid 4 scaled ss Kepsilon Turbulence Model (density const, ground symm, bouss approach)	Grid 4 scaled ss KOmega Turbulence Model (density const, ground symm, bouss approach)	Grid 4 scaled ss RSM Turbulence Model (density const, ground symm, bouss approach)
Near Wall of Cylinder	UU	0.260358733	3.94113E-05	0
	VV	0.25966841	3.67465E-05	0
	WW	0	0	0.000003
	UV	-0.00029227	-8.22519E-07	-0.307
	b11	0.000459914	0.012379539	-0.33
	b22	-0.00042511	-0.010996033	-0.33
	b33	-0.33	-0.33	-0.33
	b12	-0.0003747	-0.007215081	-0.295
	-II	0.108900336	0.109088183	0.087
	III	1.10853E-07	6.21005E-05	-0.0072
Maximum Value for Model	UU	-171.977415	-15.89251701	22.69
	VV	-998.295782	-324.7795918	15.47
	WW	0	0	16.82
	UV	-1588.8	-438.3387755	10.46
	b11	-6.97851938	-0.921945074	0.1
	b22	-38.9073589	-12.36220711	-0.037
	b33	-0.33333333	-0.333333333	-0.011
	b12	-61.3910355	-16.23476946	0.2
	-II	3497.454598	252.2815747	0.044
	III	1165.781162	84.05682119	0.000481

Table C-11: List of the anisotropic values calculated to generate the Anisotropic Invariant Map from the K-Omega turbulence models for Grid Type 4, unsteady (Anisotropy Value Near Wall of Cylinder).

Model Descriptions	Invariant Diagram Calculations	Grid 4 scaled us KOmega Turbulence Model @ 60 sec	Grid 4 scaled us KOmega Turbulence Model @ 90 sec	Grid 4 scaled us KOmega Turbulence Model @ 120 sec	Grid 4 scaled us KOmega Turbulence Model @ 150 sec
Near Wall of Cylinder	UU	0.015989714	0.026936381	0.022788136	0.021591837
	VV	0.0195536	0.00264381	-9.6E-05	-0.00239728
	WW	0	0	0	0
	UV	0.005685257	-0.00386743	-0.00174041	-0.00305633
	b11	-0.00432687	0.353819242	0.397055643	0.523485585
	b22	0.069004115	-0.26588921	-0.33641026	-0.42846345
	b33	-0.33	-0.33	-0.33	-0.33
	b12	0.1169806	-0.09865889	-0.05578231	-0.1212828
	-II	0.122883032	0.212710297	0.245585257	0.347903956
	III	0.004614401	0.034257398	0.045106135	0.078871306

Table C-11 (cont'd): List of the anisotropic values calculated to generate the Anisotropic Invariant Map from the K-Omega turbulence models for Grid Type 4, unsteady (Anisotropy Value Near Wall of Cylinder).

Model Descriptions	Invariant Diagram Calculations	Grid 4 scaled us KOmega Turbulence Model (@ 180 sec	Grid 4 scaled us KOmega Turbulence Model @ 240 sec	Grid 4 scaled us KOmega Turbulence Model @ 300 sec	Grid 4 scaled us KOmega Turbulence Model @ 330 sec
Near Wall of Cylinder	UU	0.01715778	0.011190226	0.010619592	0.010036898
	VV	-0.00100446	0.00171483	-0.00030307	-0.00064599
	WW	0	0	0	0
	UV	-0.00244379	-0.00210064	-0.00276898	-0.00291306
	b11	0.439539621	0.293921479	0.414525247	0.427037724
	b22	-0.3785794	-0.23721058	-0.35467663	-0.3822717
	b33	-0.33	-0.33	-0.33	-0.33
	b12	-0.11008053	-0.1177487	-0.19499856	-0.22068646
	-II	0.287418367	0.19248604	0.293946858	0.320846947
	III	0.058911061	0.027583393	0.061065463	0.069942493

Table C-12: List of the anisotropic values calculated to generate the Anisotropic Invariant Map from the Reynolds Stress turbulence models for Grid Type 4, unsteady (Anisotropy Value Near Wall of Cylinder).

Model Descriptions	Invariant Diagram Calculations	Grid 4 scaled us RSM (density bouss, ground symm, bouss approach) @T=18 sec	Grid 4 scaled us RSM (density bouss, ground symm, bouss approach) @T=77.5 sec	Grid 4 scaled us RSM (density bouss, ground symm, bouss approach) @T=137.5 sec	Grid 4 scaled us RSM (density bouss, ground symm, bouss approach) @T=197.5 sec	Grid 4 scaled us RSM (density bouss, ground symm, bouss approach) @T=257.5 sec	Grid 4 scaled us RSM (density bouss, ground symm, bouss approach) @T=317.5 sec	Grid 4 scaled us RSM (density bouss, ground symm, bouss approach) @T=335.5 sec
Near Wall of Cylinder	UU	0.000027	0.000011	0.000002	0.000003	0.000001	0.000001	0.000001
	VV	0.000013	0.000093	0.000007	0.000001	0.000006	0.000008	0.00000999
	WW	0.00099	0.000095	0.000022	0.000011	0.000004	0.000006	0.000007
	UV	-0.058	-0.033	-0.0121	0.0021	-0.0075	0.0025	-0.01
	b11	-0.33324521	-0.3332847	-0.33332281	-0.33331468	-0.33332609	-0.3333252	-0.33332493
	b22	-0.33329091	-0.33292219	-0.3329649	-0.33332711	-0.33328986	-0.33326829	-0.33324938
	b33	-0.33	-0.33	-0.33	-0.33	-0.33	-0.33	-0.33
	b12	-0.18929504	-0.14588859	-0.06368421	0.013059701	-0.05434783	0.020325203	-0.08403361
	-II	0.033665013	0.019225608	0.001860357	-0.00203226	0.000759483	-0.00177361	0.004881321
	III	-0.02482755	-0.02959255	-0.03532308	-0.03660765	-0.03568637	-0.03652229	-0.03432616

Table C-13: List of the pressure coefficient values calculated to generate the plot of the surface pressure distribution generated on the bottom wall of the cylinder.

Theta (degrees)	Coefficient of Pressure (Cp)
0	1.52
15	1.05
30	0.15
45	-0.99
60	-2.08
75	-2.84
90	-3.07
105	-2.6
120	-1.74
135	-0.75
150	-0.09
165	-0.033
180	0.053

Table C-14: List of the anisotropic values calculated to generate the Anisotropic Invariant Map generated from the combination of the Reynolds stresses and the mean temperature evaluated using the steady state K-Epsilon turbulence model for Grid Type 4 (Measured between Cylinder & Heated Plate).

Y-coordinate between cylinder and heated plate	Invariant -II	Invariant III
0.040953297	0.083408296	-0.009234272
0.039832428	0.083343858	-0.009255751
0.038711558	0.083332769	-0.009259447
0.037590688	0.083332714	-0.009259466
0.036469819	0.083332411	-0.009259567
0.035348949	0.083331858	-0.009259751
0.03422808	0.083330874	-0.009260079
0.03310721	0.083329646	-0.009260488
0.031986341	0.083325964	-0.009261716
0.030865471	0.083325964	-0.009261716
0.029744601	0.083325964	-0.009261716
0.028623732	0.083343714	-0.009255799
0.027502862	0.083343714	-0.009255799
0.026381993	0.083343714	-0.009255799
0.025261123	0.083343714	-0.009255799
0.024140254	0.083343714	-0.009255799
0.023019384	0.083338521	-0.00925753
0.021898514	0.083336791	-0.009258107
0.020777645	0.083335926	-0.009258395
0.019656775	0.083335408	-0.009258568
0.018535906	0.083335062	-0.009258683
0.017415036	0.083334831	-0.00925876
0.016294167	0.083334378	-0.009258911
0.01522	0.083311581	-0.00926651
0.01517	0.083303968	-0.009269048
0.01511	0.083285986	-0.009275042
0.01506	0.083238997	-0.009290705
0.01501	0.083125906	-0.009328402

Table C-15: List of the anisotropic values calculated to generate the Anisotropic Invariant Map generated from the combination of the Reynolds stresses and the mean temperature evaluated using the unsteady K-Epsilon turbulence model for Grid Type 4 at t = 60 seconds (Measured between Cylinder & Heated Plate).

Y-coordinate between cylinder and heated plate	Invariant -II	Invariant III
0.040953297	0.083329624	-0.009260496
0.039832428	0.083335496	-0.009258538
0.038711558	0.130022925	0.006303938
0.037590688	0.118422638	0.002437176
0.036469819	0.169985922	0.019624937
0.035348949	0.243971555	0.044286815
0.03422808	0.084635572	-0.00882518
0.03310721	0.178266659	0.022385183
0.031986341	0.173678426	0.020855772
0.030865471	0.181625066	0.023504652
0.029744601	0.194301167	0.027730019
0.028623732	0.201411937	0.030100275
0.027502862	0.201411937	0.030100275
0.026381993	0.198632944	0.029173944
0.025261123	0.195123541	0.028004143
0.024140254	0.19087553	0.02658814
0.023019384	0.185631227	0.024840039
0.021898514	0.188539279	0.025809389
0.020777645	0.212987373	0.033958754
0.019656775	0.220294374	0.036394421
0.018535906	0.18858835	0.025825746
0.017415036	0.079797773	-0.010437779
0.016294167	0.083332445	-0.009259555
0.01522	0.083317044	-0.009264689
0.01517	0.083322108	-0.009263001
0.01511	0.083293672	-0.00927248
0.01506	0.082032324	-0.009692929
0.01501	0.083730001	-0.009127037

BIBLIOGRAPHY

BIBLIOGRAPHY

Catton, I. (1978). Natural Convection in Enclosures. Proc. 6th Int. heat Transfer Conf., Toronto, Canada. Vol. 6, pp. 13-31

Choi, K.S and Lumley, J.L. (2001). The return to isotropy of homogeneous turbulence. Journal of Fluid Mechanics. vol. 436, Issue 01, p.59-84

Chung, Kathy, Geer, Larry, Rajadural, Sivanandi. (2000) Numerical Simulation and Experimentation Validation of the Catalytic Converter Cool Down Process. SAE #2000-01-0204; Society of Automotive Engineers.

Damodaran, Vijay; Kaushik, Shailendra. (2000). Simulation to Identify and Resolve Underhood/Underbody Vehicle Thermal Issues. Journal Article by Fluent Software Users JA118, Fluent Inc..

Elsherbiny, S. M., Raithby, G. D., and Hollands, K. G. T. (1982). Heat Transfer by Natural Convection Across Vertical and Inclined Air Layers. ASME J. Heat Transfer, **104**, pp. 96–102.

Fluent Incorporated. (2005). Fluent 6.2 User Guide.

Fluent Incorporated. (2005). Fluent 6.1 Tutorial Guide. http://simba.ara.bme.hu/~cfd/fluent6.1doc/help/html/tg/main_pre.htm.

Fox, R. and McDonald, A. (1998) Introduction to Fluid Mechanics: Fifth Edition. pp. 354.

Fu, S., Launder, B. E., and Leschziner, M. A. (1987). Modeling Strongly Swirling Recirculating Jet Flow with Reynolds-Stress Transport Closures. In Sixth Symposium on Turbulent Shear Flows, Toulouse, France.

Gibson, M. M. and Launder, B. E.(1978). Ground Effects on Pressure Fluctuations in the Atmospheric Boundary Layer. J. Fluid Mech., 86:491{511}.

Hsu et al. (2003). Methodology for Speciation of Organic Gas Hot Soak Emissions California Light-Duty Vehicles.

Jovicic, N., Breuer, M., and Jovanovic, J. (2006) Anisotropy-Invariant Mapping of Turbulence in a Flow Past an Unswept Airfoil at High Angle of Attack. J. Fluids Engineering, 128, pp. 560.

Karlsson, Rolfe. (2003). GM Thermal Vehicle Integration Engineer, Personal Communication.

Krogstad, P.A. and Simonsen, A.J (2005). Turbulent Stress Invariant Analysis: Clarification of Existing Terminology. Physics of Fluids 17, pp. 088103-3.

Launder, B. E. (1989). Second-Moment Closure and Its Use in Modeling Turbulent Industrial Flows. International Journal for Numerical Methods in Fluids, 9:963{985}.

Launder, B. E. and Shima, N. (1989). Second-Moment Closure for the Near-Wall Sublayer: Development and Application. AIAA Journal, 27(10):1319{1325}.

Lee, Kwangjin. (1999). Numerical Prediction of Brake Fluid Temperature Rise During Braking and Heat Soaking. SAE 1999-01-0483; Society of Automotive Engineers.

Lien, F. S. and Leschziner, M. A. (1994). Assessment of Turbulent Transport Models Including Non-Linear RNG Eddy-Viscosity Formulation and Second-Moment Closure. Computers and Fluids, 23(8):983-1004.

Lumley, J. L., and Newman, G. (1977). The Return to Isotropy of Homogeneous Turbulence. J. Fluid Mech., **82**, pp. 161–178.

Lumley, J. L. (1978). Computational Modeling of Turbulent Flows. *Adv. Appl. Mech., 18* , pp. 123-176.

Markatos, N. C., and Pericleous, K. A. (1984). Laminar and Turbulent Natural Convection in an Enclosed Cavity. Int. J. Heat Mass Transf., **27**, pp. 755–772.

Munson, B. R., Young, D. F., and Okiishi, T.H. (2002). Fundamentals of Fluid Mechanics: Fourth Edition. pp. 570.

Sabersky, R.H., Acosta, A.J., Hauptmann, E.G., and Gates, E.M. (1999). Fluid Flow, A First Course In Fluid Mechanics: Fourth Edition, pp. 269.

Turner, David. (2003). GM Thermal Technical Integration Engineer, Personal Communication.

Velusamy, K., Sundararajan, T., and Seetharamu, K.N. (2001). Interaction Effects Between Surface Radiation and Natural Turbulent Convection in Square and Rectangular Enclosures. ASME J. Heat Transfer, 123, pp. 1065.